Theme: Phytoplankton and Macroalgae

Case Study 5

Observation of Ocean Colour Beyond Chlorophyll-*a*: From Particulate Organic Carbon Content and Size Distribution to Phytoplankton Functional Groups

Séverine Alvain[*1], **Lucile Duforêt-Gaurier**[1] **and Hubert Loisel**[1]

5.1 Background Information

The term phytoplankton encompasses all microscopic plant-like organisms living in the illuminated surface layers of the ocean. The existence of phytoplankton is of fundamental interest as they form the base of the aquatic food web, providing an essential ecological function for all aquatic life.

Phytoplankton also play an important role in the biological pump of carbon and CO_2 sequestration. During the process of photosynthesis, phytoplankton take up dissolved CO_2 and convert it into organic compounds, using energy from the sun. This transformation is of biogeochemical importance for two reasons: firstly the resulting organic carbon no longer participates in the equilibrium of the carbonate system, thus increasing the ocean's ability to dissolve carbon dioxide. Secondly, the particulate organic carbon sinks from surface waters to deeper layers, removing carbon from the surface layer. The biological pump thus plays a very important role in the Earth's carbon cycle, and the evolution of the biological pump will play a key role in understanding climate change scenarios.

Like terrestrial plants, phytoplankton use pigment antennae to capture the energy of photons. Among these phytoplankton pigments is chlorophyll-*a*, which is used as an index of the phytoplankton biomass. Chlorophyll-*a* selectively modifies the flux of photons that penetrate the ocean's surface layer. It absorbs the red and blue wavelengths and scatters the green ones. For this reason, the colour of the ocean will range from blue-green to green depending on the type and density of phytoplankton populations. Thus, by studying the colour of light reflected from the oceans, in other words ocean colour, optical sensors can quantify the amount of chlorophyll and other constituents.

[1]Université Lille Nord de France, LOG CNRS, ULCO, USTL, UMR8187, F-62930 Wimereux, France.
[*]*Email address:* severine.alvain@univ-littoral.fr

Visible and near-infrared passive radiometers onboard spacecraft provide useful data at spatial and temporal scales unattainable by shipboard sampling. This was fully demonstrated by the first satellite, CZCS, dedicated to the observation of ocean colour. Since then, a number of advanced ocean-colour satellites have been launched. In the past few years, inversion of ocean-colour satellite data has moved beyond the estimation of chlorophyll-*a* concentration to include new parameters which make it possible, for example, to determine the dominant phytoplankton species in the surface waters, to get information about particle size distribution (Loisel et al., 2006) and to retrieve information about other biogeochemical components such as particulate organic carbon (POC), and coloured detrital matter (Stramski et al., 1999; Loisel et al., 2002; Siegel et al., 2002). Consequently, information on dominant phytoplankton groups can be superimposed on POC and size distribution maps, allowing for a large range of new applications. Information obtained from satellite observation is restricted to the near-surface layer. Indeed, the surface oceanic layer that is remotely sensed in the visible part of the spectrum is the first attenuation layer, generating 90% of the photons that form the upward flux just beneath the surface (Gordon and McCluney, 1975). The thickness of this layer typically varies from a few meters to about 60 meters, depending on the presence of optically-significant constituents in the water and the wavelength considered (Smith and Baker, 1978). Products derived from satellite data such as chlorophyll or POC concentration are integrated over the first penetration depth.

5.2 Materials and Methods

5.2.1 POC Estimates from Space

In this section, we will present the Loisel et al. (2002) method used to estimate the near-surface concentration of POC from satellite data (POC_{surf}). This method consists of deriving POC_{surf} from the inherent optical properties, as presented in Loisel et al. (2002). The natural variations of optically-significant substances in seawater can be observed through the measurements of inherent optical properties (IOPs). Among these IOPs, the total backscattering coefficient of seawater, b_b, is not sensitive to the dissolved material. The $b_b$coefficient can therefore be partitioned into two components $b_b = b_{bp} + b_{bw}$ where b_{bw} is the backscattering coefficient of seawater (Morel and Prieur, 1977) and b_{bp} is the backscattering coefficient of particles. The b_{bp} variability is governed (to the first order) by changes in the abundance and (to the second order) composition of the particle assemblage.

Previous studies at regional (Stramski et al., 1999; Loisel et al., 2001) and global scales (Loisel et al., 2002) have demonstrated the feasibility of estimating POC from b_{bp}. The robust relationship found between POC and b_{bp} can be explained by the fact that under non-bloom conditions, b_{bp} is governed mainly by small-sized, non-living particles (Stramski and Kiefer, 1991; Morel and Ahn, 1991), which represent the

dominant contribution of POC in the open ocean (Koike et al., 1990). Note that previous studies have shown a good correlation between *in situ* b_{bp} and POC values in different oceanic areas (Reynolds et al., 2001; Stramski et al., 2008).

In a remote-sensing context, the backscattering coefficient of seawater is not measured directly, but is derived by the inversion of the natural light field reflected back out of the ocean and detected by the satellite ocean-colour sensor. In this study, $b_b(490)$ is retrieved from the remote-sensing reflectance at 443nm, 490nm and 555nm, using the method developed by Loisel and Stramski (2000), and slightly modified by Loisel and Poteau (2006).

Because coincident measurements of the particle backscattering coefficient and POC are still very scarce, the parameterization of POC_{surf} is established as a function of the particle scattering coefficient, b_p, which is derived from b_{bp} using the following empirical relationship (Twardowski et al., 2001):

$$b_{bp}(490)/b_b(490) = 0.0096 \times [\text{chl-}a]^{-0.253} \tag{5.1}$$

A simple linear relationship is used between POC_{surf} and b_p (Claustre et al., 1999; Loisel et al., 2001). Based on results of previous studies carried out in different regions of the global ocean, a mean slope value of 400 mg m^{-2} is adopted (Claustre et al., 1999; Loisel et al., 2002) with a null intercept as a first approximation.

Figure 5.1 displays the global maps of the POC_{surf} near-surface concentration for the SeaWiFS period 1997-2008 during June and January. The global distribution of POC_{surf} follows the major gyre systems and other large scale circulation features of the ocean. Low surface POC concentrations are encountered in subtropical gyres, where large scale downwelling is expected. For example in the South Pacific gyre, POC_{surf} is less than 50 mg m^{-3}. Elevated near-surface POC concentrations in the range 100-200 mg m^{-3} are encountered at high and temperate latitudes (e.g. Antarctic Circumpolar Current, sub-arctic gyres, temperate North Atlantic). Compared to subtropical gyres, these areas are characterized by a high chlorophyll concentration (by a factor of about ten, Figure 5.2) supported by inputs of nutrients injected from below the euphotic layer by advection or vertical mixing, or from terrestrial sources.

5.2.2 Spectral Dependency of Optical Backscattering by Marine Particles: A Proxy of the Particle Size Distribution

Knowledge of the relative proportions of small- and large-sized particles in the surface ocean is essential for understanding the ocean ecology and biogeochemistry, including particle dynamics and carbon cycling. This information may be assessed qualitatively from satellite observations of ocean colour (see Figure 5.3). Such capability is based on the estimation of spectral dependence of the particulate backscattering coefficient, b_{bp}, denoted γ, which is sensitive to particle size distribu-

tion. The greater the value of (the steeper the slope), the more small particles are present in the water column, relative to large particles (and vice versa).

The retrieval of γ from ocean-colour remote sensing observations is performed in two steps. First, $b_{bp}(\lambda)$ is assessed at different visible wavelengths, λ, by an inverse algorithm which uses the light field estimated from the total signal measured at the top of the atmosphere and corrected for atmospheric effects (Loisel and Stramski, 2000). Then, γ is calculated by linear regression between Log (b_{bp}) and Log (λ). In general, the γ values are much greater in summer than in winter, which holds true for both the northern and southern hemisphere (Figure 5.3). Seasonal variations of indicate that the proportion of small-sized particles compared to larger particles increases from winter to summer in the surface waters of the global oceans. These spatio-temporal patterns are interpreted in terms of processes that modify the composition of particulate assemblages and physiology of phytoplankton in response to environmental forcing.

5.2.3 Detection of Dominant Phytoplankton Groups: The PHYSAT Method

Phytoplankton play an important role in many global biogeochemical cycles. However, the efficiency and impact of phytoplankton depends strongly on the nature of phytoplankton itself. Thus monitoring the spatial and temporal distribution of dominant phytoplankton groups is of critical importance. From a pigment point of view, the main phytoplankton groups have specific pigments, called biomarkers. The PHYSAT algorithm (Alvain et al., 2005; Alvain et al., 2008) has been developed based on an empirical relationship between coincident *in situ* biomarker pigment measurements and remote sensing reflectance anomalies. The PHYSAT method has been applied to the SeaWiFS satellite archive, from September 1997 to December 2008. Monthly PHYSAT data have been used to retrieve the monthly climatology maps for January and June, shown in Figure 5.4.

The main difficulty in ocean-colour measurements (in the visible spectrum) is caused by the atmosphere and aerosols which act to diffuse and absorb light. The atmosphere is responsible for about 95% of the signal detected by a satellite sensor. However, the portion of the signal that carries information from the ocean and the atmosphere respectively can be deconvoluted. This is currently done using atmospheric correction algorithms. The measurements we used here are obtained after atmospheric correction. However, since we used second order variability for the PHYSAT method, some additional criteria have to be applied. Thus, we will consider, for the PHYSAT part, only pixels associated with an aerosol optical thickness less than 0.15. Another validity criteria concerns the concentration of chlorophyll-*a*, [chl-*a*], which has to be lower than 3 mg m^{-3} to exclude waters possibly contaminated by coastal material, and higher than 0.04 mg m^{-3} to discard ultra-oligotrophic waters where it is unlikely that a dominant group can be found using ocean-colour data.

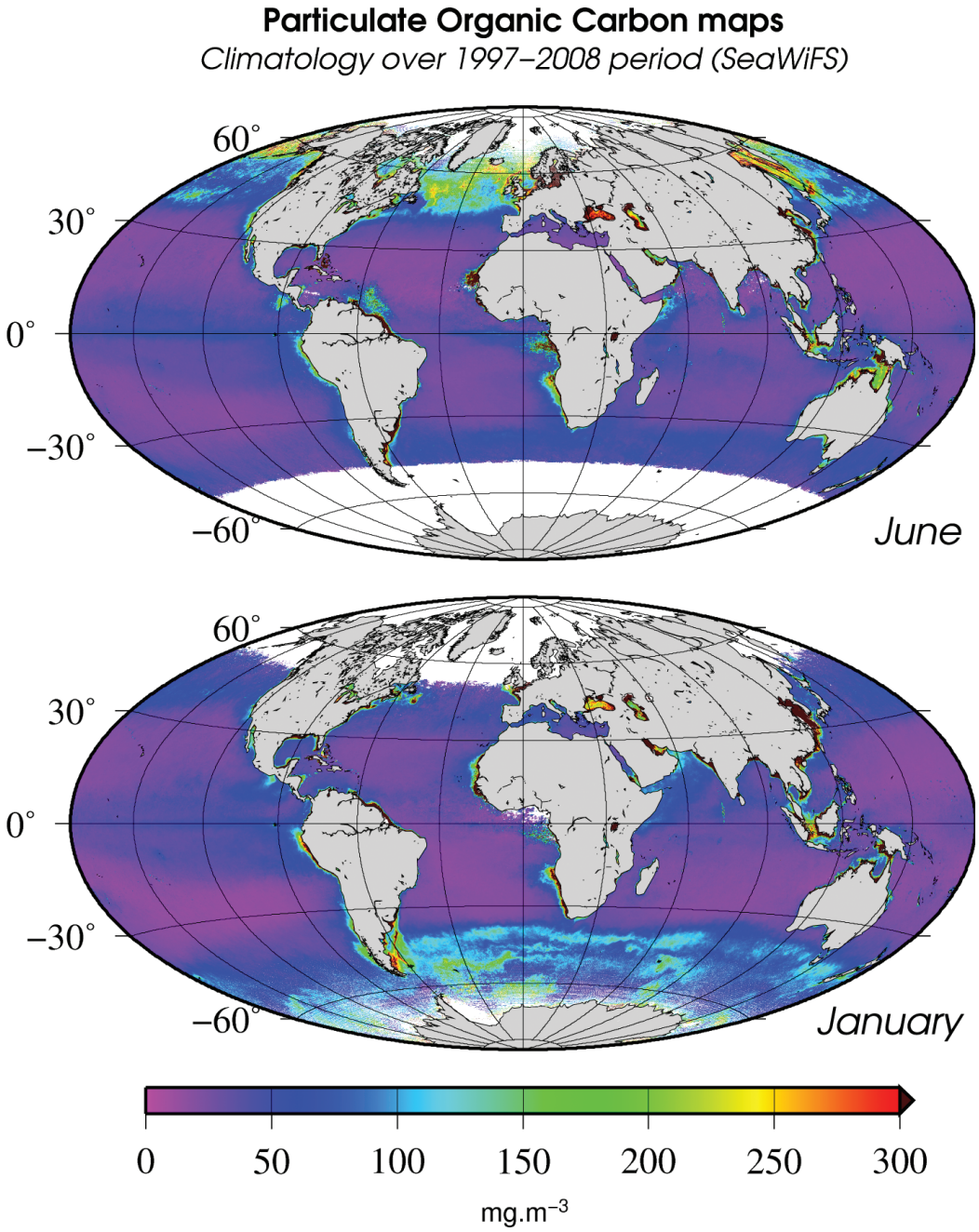

Figure 5.1 Particulate organic carbon (POC) climatology maps (1997 – 2008, SeaWiFS) for the months of June and January.

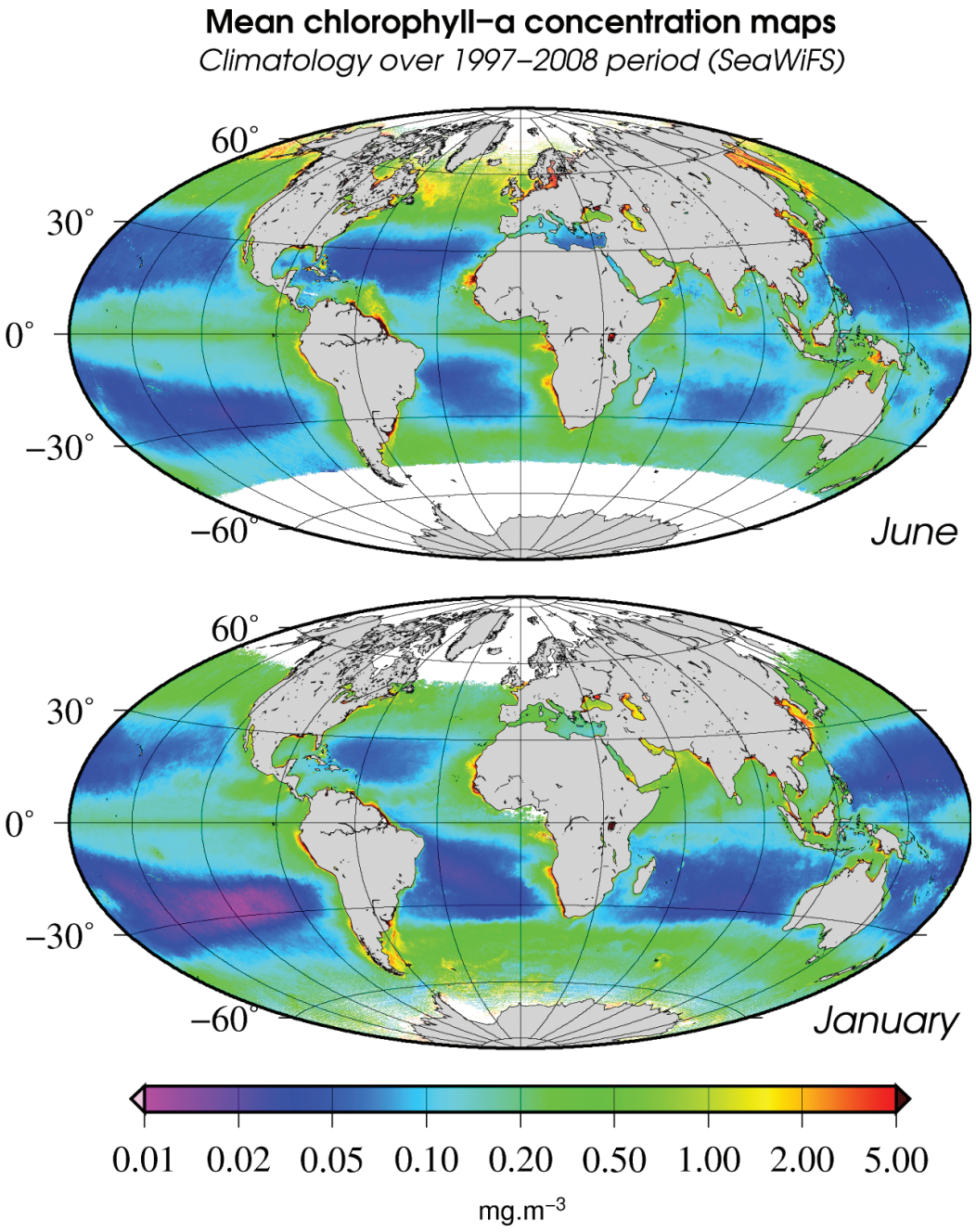

Figure 5.2 Mean chlorophyll-*a* concentration climatology maps (1997 – 2008, SeaWiFS) for the months of June and January.

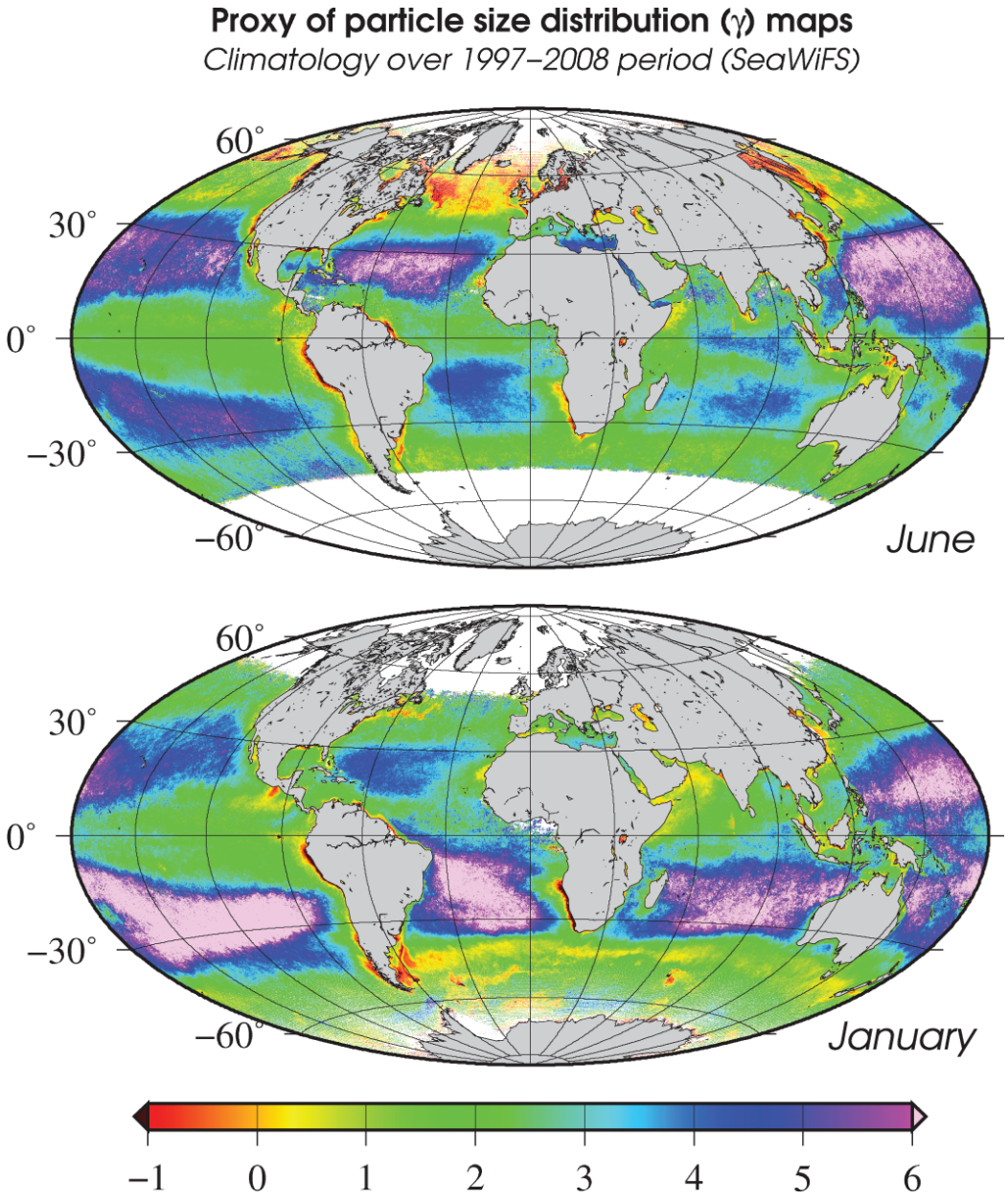

Figure 5.3 Particle size distribution proxy (γ) climatology maps (1997-2008, SeaWiFS) for the months of June and January.

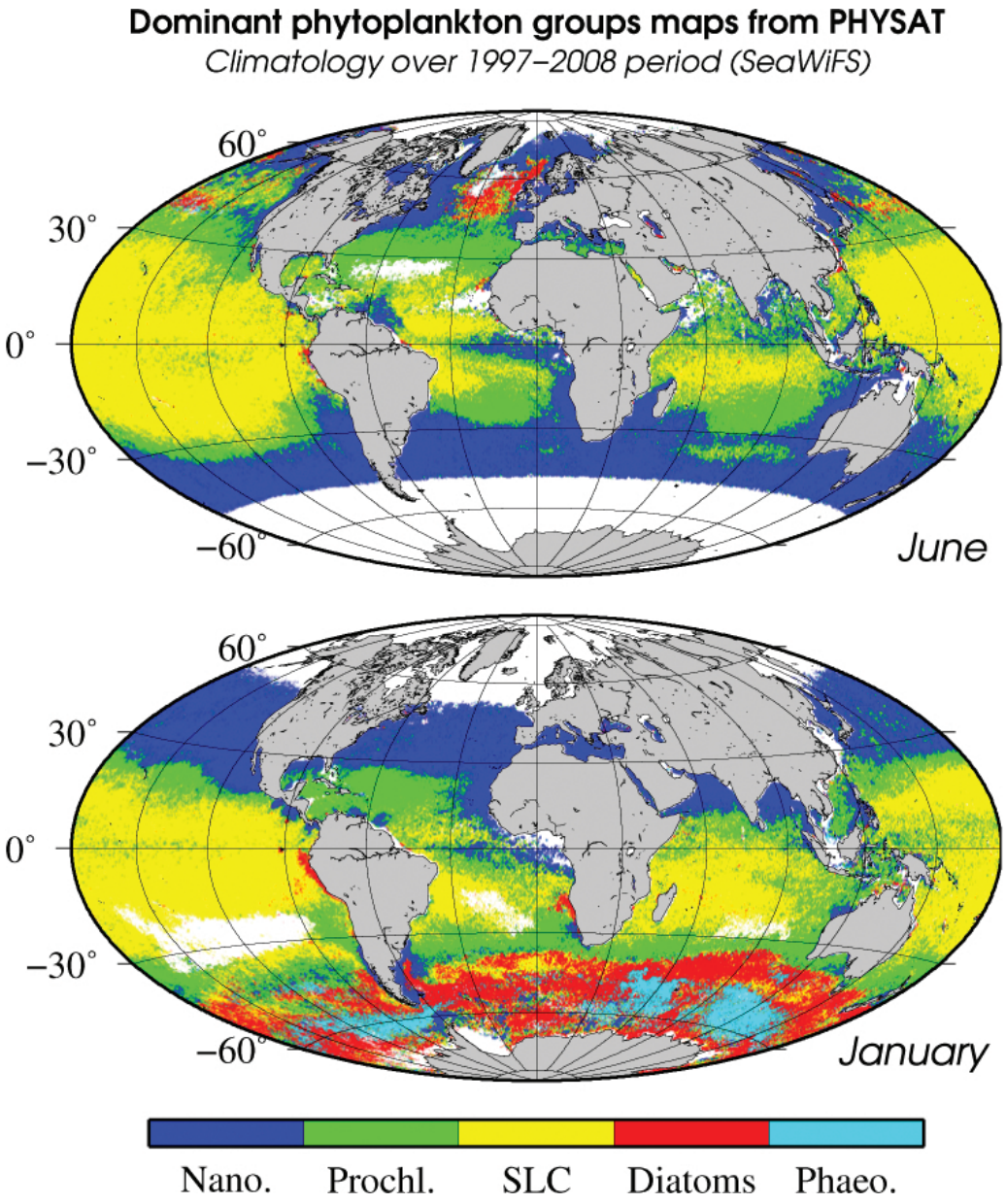

Figure 5.4 Climatology maps (1997 – 2008, SeaWiFS) of dominant phytoplankton groups for the months of June and January, estimated using PHYSAT. Nano. = nanophytoplankton, Prochl. = *Prochlorococcus*, SLC = *Synechococcus*-like cyanobacteria (SLC), and Phaeo. = *Phaeocystis*.

The PHYSAT approach is based on the identification of specific signatures in the nLw spectra classically measured by ocean-colour sensors, after the previous criteria concerning atmospheric correction and [chl-*a*] has been applied. PHYSAT is an empirical method, established by comparing two kinds of simultaneous and coincident measurements: SeaWiFS nLw measurements and *in situ* measurements of biomarker phytoplankton pigments performed in the framework of the Gep&Co program (Dandonneau et al., 2004). In a first study, four dominant phytoplankton groups were identified within the GeP&CO dataset: diatoms, nanoeukaryotes, *Synechococcus* and *Prochlorococcus*. Recently, the PHYSAT method has been improved to detect an additional group, namely the *Phaeocystis*-like group, by analyzing specific signal anomalies in the Southern Ocean during winter months (Alvain et al., 2008). Note that the PHYSAT method allows detection of these groups only when they are dominant, that is, in situations where a given phytoplankton group is a major contributor (>60%) of the total pigment concentration. It is important to point out that, even if there is a general agreement on the taxonomic message of each biomarker pigment, for example, divinyl chlorophyll-*a* (d-chl-*a*), is associated with *Prochlorococcus*, a large range of relative concentrations (pigments ratios) can be found in the literature. Pigment ratios are defined as:

$$P_{rel} = P/([\text{chl-}a] + [\text{d-chl-}a]), \tag{5.2}$$

where P is the measured biomarker pigment concentration. A thorough analysis of pigment ratios from the literature has allowed us to define a mean, relative concentration for each group, thus allowing thresholds to be fixed. A group is considered dominant when P_{rel} is at least equal to 60% of the total. Detailed information of the method including the use of thresholds is available in Alvain et al. (2005).

The key step in the success of methods such as PHYSAT is to associate *in situ* measurements with remote sensing measurements after having removed the first order variations due to the chlorophyll-*a* concentration (and classically used in previous ocean-colour products). Thus, a second step to establish PHYSAT has been to transform the nLw SeaWiFS spectra into specific normalized water leaving radiance, noted nLw*, to determine the second order variability of the satellite signal. This was done by dividing the actual nLw by a mean nLw model (nLw_{ref}), established from a large remote sensing dataset of nLw(λ) and [chl-*a*], cf. equation 5.3.

$$nLw^*(\lambda) = nLw(\lambda)/nLw_{ref}(\lambda, [\text{chl-}a]) \tag{5.3}$$

The nLw_{ref} depends only on the standard SeaWiFS chlorophyll-*a*. By dividing nLw by this reference, we obtain a new product, denoted nLw*, which is used in PHYSAT. Indeed, it has been shown that every dominant phytoplankton group sampled during the GeP&Co dataset is associated with a specific nLw* spectrum. It is thus possible

to define a set of criteria to characterize each group as a function of its nLw* spectrum. These criteria can thus be applied to the global daily SeaWiFS archive to obtain global monthly maps of the most frequently detected dominant groups, as shown in Figure 5.4. Note that when no group prevails over the period of one month, the pixels are associated with an 'unidentified' group. Alvain et al. (2008) studied the geographical distribution and seasonal succession of major dominant phytoplankton groups which are in good agreement with previous studies (Zubkov et al., 2000; DuRand et al., 2001; Marty and Chivérini, 2002; Dandonneau et al., 2004; Longhurst 2007). However, as for all empirical ocean-colour methodology, validation based on *in situ* measurements has to be pursued each time a suitable dataset is available.

5.3 Questions

Q 1: What can you say about the spatial distribution of POC, chl-*a* and dominant phytoplankton groups (from Figures 5.1, 5.2, and 5.4)? Look specifically at the following areas: (i) 45 – 52°N, 30 – 15°W and (ii) 47 – 40°S, 65 – 80°E for the month of January.

Q 2: In the future, what sort of potential applications could be considered from synergy of data of POC, [chl-*a*] and dominant phytoplankton groups?

Q 3: How would you explain the high POC concentration (~250 – 300 mg m^{-3}) encountered around Alaska, British Isles and the Yellow East China Sea seen in Figure 5.1?

Q 4: What can you say about diatom distribution in Figure 5.4?

Q 5: What will PHYSAT detect (ideally) if the relative contribution to the total pigment concentration is: 20% for group 1, 40% for group 2 and 40% for group 3?

Q 6: Is it possible to apply PHYSAT, as described above, to coastal waters, and why?

Q 7: What should I do if I want to apply the PHYSAT method to a different satellite?

Q 8: What is essential to establish a method like PHYSAT ?

Q 9: What is essential to apply a method like PHYSAT, in addition to water leaving radiances?

Q 10: How could we validate PHYSAT or improve PHYSAT?

5.4 Answers

A 1: These two areas are almost identical in terms of chlorophyll-*a* concentration but are distinct in term of POC concentration. Furthermore, these two areas are also distinct in terms of phytoplankton groups. The region in the Southern ocean is dominated by diatoms whereas the region in the northern Atlantic is dominated by nanoeukaryotes. The actual results for these two areas for the period 1998 – 2006 are summarised below in Table. 1.

Table 5.1 Mean near-surface POC and chlorophyll-*a* concentration over the areas in question for the SeaWiFS monthly climatology of January (1998 – 2006), as well as the percentage of pixels dominated by various phytoplankton groups (nano= nanophytoplankton; Prochl = *Prochlorococcus*; SLC = *Synechococcus*-like cyanobacteria; and Phaeo = *Phaeocystis*-like).

	(45–52°N, 30–15°W)	**(47–40°S, 65–80°E)**
Chl-*a* (mg m^{-3})	0.20 ± 0.07	0.33 ± 0.10
POC (mg m^{-3})	40.07 ± 10.8	172.8 ± 23.5
% Nano	98	8
% Prochl	2	4
% SLC	0	15
% Diatoms	0	69
% Phaeo	0	4

A 2: Coincident information of [chl-*a*], POC and dominant phytoplankton groups could be interpreted from an ecological point of view. We could carry out studies to investigate:

- links between dominant phytoplankton groups and the food web
- links between phytoplankton species and POC and chlorophyll-*a* concentration
- relationship between phytoplankton and POC and nutrients, irradiance and stratification.

In the future, new ocean colour parameters will help to assess the relationship between the total biomass and/or phytoplankton composition and productivity (for resource management).

A 3: In these areas, some of the high POC_{surf} values may result from the presence of coastal waters, which carry particles of terrigenous origin which affect the remote sensing reflectance, resulting in an overestimate of the near-surface POC concentration. The algorithm described above is not appropriate for estimating POC content in these coastal waters. Consequently, these high POC concentrations should not be considered.

A 4: Diatom blooms are observed mainly in the North Atlantic and North Pacific Ocean during spring. During the austral summer, large blooms of diatoms are also observed at latitudes less than 30°S as well as in upwelling areas off the west coast

of southern Africa and South America.

A 5: In this case, PHYSAT will not detect a dominant group, since a dominant group should contribute at least 60% of the total pigment concentration.

A 6: No, because coastal waters are influenced by other organic and inorganic material (e.g. sediments, mineral particles, coloured dissolved organic matter) that can change the nLw but are not related to phytoplankton, and are not taken into account in PHYSAT.

A 7: In this case, it is necessary to calculate a new look up table containing the nLw_{ref} spectra for the new satellite. It is also necessary to check and adapt thresholds used to classify nLw* spectra.

A 8: As PHYSAT is an empirical method, it is essential to have *in situ* information about dominant phytoplankton groups (e.g. using pigments or others methods) and coincident and simultaneous water leaving radiance measurements, during very clear sky atmosphere conditions.

A 9: It is essential to have information about atmospheric conditions (such as aerosol optical thickness) and the concentration of chlorophyll-*a*.

A 10: Since PHYSAT is an empirical method, it is rather difficult to evaluate errors precisely. However, each time an *in situ* dataset with enough information about dominant phytoplankton groups is available, it is essential to use it to validate the method. Some optical studies are currently in progress to better understand the relationship between specific nLw* spectra and specific dominant groups.

5.5 References

Alvain S, Moulin C, Dandonneau Y, Bréon FM (2005) Remote sensing of phytoplankton groups in case 1 waters from global SeaWiFS imagery. Deep-Sea Res I 52: 1989-2004

Alvain S, Moulin C, Dandonneau Y, Loisel H (2008) Seasonal distribution and succession of dominant phytoplankton groups in the global ocean: A satellite view. Global Biogeochem Cycles 22: GB3001, doi:10.1029/2007GB003154

Claustre H, Morel A, Babin M, Cailliau C, Marie D, Marty JC, Talliez D, Vaulot D, (1999) Variability in particle attenuation and chlorophyll fluorescence in the tropical Pacific: Scales, patterns and biogeochemical implications. J Geophys Res 104(C2): 3401-3422

Dandonneau Y, PY Deschamps, JM Nicolas, H Loisel, J Blanchot, Y Montel, F Thieuleux and G Bécu (2004) Seasonal and interannual variability of ocean color and composition of phytoplankton communities in the North Atlantic, Equatorial Pacific and South Pacific. Deep Sea Res II 51: 303-318

DuRand MD, Olson RJ, Chisholm SW (2001) Phytoplankton population dynamics at the Bermuda Atlantic time-series station in the Sargasso Sea. Deep Sea Res II 48: 1983-2003

Gordon HR, McCluney MR (1975) Estimation of the depth of the sunlight penetration in the sea for remote sensing. Appl Opt 14(2): 413-416

Koike I, Hara S, Terauchi K, Kogure K (1990) Role of submicrometer particles in the ocean. Nature 345: 242-244

Loisel H, Stramski D (2000) Estimation of the inherent optical properties of natural waters from the irradiance attenuation coefficient and reflectance in the presence of Raman scattering. Appl Opt 39(18): 3001-3011

Loisel H, Bosc E, Stramski D, Oubelkheir K, Deschamps PY (2001) Seasonal variability of the backscattering coefficient in the Mediterranean Sea based on Satellite SeaWiFS imagery. J Geophys Res Lett 28(22): 4203-4206

Loisel H, Nicolas J M, Deschamps P Y, Frouin R (2002) Seasonal and inter-annual variability of particulate organic matter in the global ocean. Geophys Res Lett 29(49): 2196, doi:10.1029/2002GL015948

Loisel H, Poteau A (2006) Inversion of IOP based on Rrs and remotely retrieved Kd. In: IOCCG (2006). Remote Sensing of Inherent Optical Properties: fundamental tests of algorithms and applications. Reports of the International Ocean-Colour Coordinating Groups, No 5, Lee, ZP (ed), IOCCG, Dartmouth, Canada, p 35-42

Longhurst A (2007) Ecological Geography of the Sea, 2nd Edition, Academic Press, San Diego, USA

Marty JC, Chiavérini J, Pizay MD, Avril B (2002) Seasonal and interannual dynamics of nutrients and phytoplankton pigments in the western Mediterranean Sea at the DYFAMED time series station (1991-1999) Deep Sea Res II, 49: 2017-2030

Morel A, Ahn YH (1991) Optics of heterotrophic nanoflagellates and ciliates: A tentative assessment of their scattering role in oceanic waters compared to those of bacterial and algal cells. J Marine Res 48: 1-26

Morel A, Prieur L (1977) Analysis of variations in ocean color. Limnol Oceanogr 22(4): 709-722

Reynolds RA, Stramski D, Mitchell BG (2001) A chlorophyll-dependent semi-analytical model derived from field measurements of absorption and backscattering coefficients within the Southern Ocean. J Geophys Res 106: 7125-7138

Siegel DA, Maritorena S, Nelson NB (2002). Global distribution and dynamics of colored dissolved and detrital organic materials. J Geophys Res 107(C2): 3228, doi:10:1029/2001JC000965

Smith RC, and Baker KS (1978) The bio-optical state of ocean waters and remote sensing. Limnol Oceanogr 23: 247-259.

Stramski D, Kiefer DA (1991) Light scattering by microorganisms in the open ocean, Prog Oceanogr 28: 343-383

Stramski D, Reynolds RA, Kahru M, Mitchell, BG (1999) Estimation of particulate organic carbon in the ocean from satellite remote sensing. Science 285: 239-241

Stramski, D Reynolds RA, Babin M, Kaczmarek S, Lewis MR, Rottgers R, Sciandra A, Stramska M, Twardowski MS, Franz BA, Claustre H (2008) Relationships between the surface concentration of particulate organic carbon and optical properties in the eastern South Pacific and eastern Atlantic Oceans Biogeosciences 5: 171-201

Twardowski MS, Boss E, Macdonald JB, Pegau WS, Barnard AH, Zaneveld JR (2001) A model for bulk refractive index from the optical backscattering ratio and the implications for understanding particle composition in case I and case II waters. J Geophys Res 106(C7): 14,129-14,142

Zubkov MV, Sleigh MA, Burkill PH, Leakey RJG (2000) Picoplankton community structure on the Atlantic Meridional transect : A comparison between seasons. Prog Oceanogr 45: 369-386

Case Study 6

Monitoring Phytoplankton Productivity from Satellite: An Aid to Marine Resources Management

Frédéric Mélin[*1] **and Nicolas Hoepffner**[*1]

6.1 Introduction

An important biogeochemical quantity monitored by satellites is the concentration of chlorophyll-*a*, an omnipresent pigment in all phytoplankton species and, for this reason, commonly used as an index of phytoplankton biomass. In marine waters, phytoplankton biomass is a key component of the ecosystem. Phytoplankton are responsible for the conversion of carbon dioxide to organic carbon through the process of photosynthesis, i.e. primary production. Marine photosynthesis represents approximately half of the total carbon fixation in the global biosphere, making it a critical element of the Earth's carbon budget and biogeochemical cycles. In addition, phytoplankton biomass and primary production are descriptors of the first trophic level in the marine food chain. Quantitative estimates of these variables from satellite could therefore provide important information on the structure and functioning of the rest of the food web, up to commercially exploited fish populations.

6.2 Materials and Methods

6.2.1 Modelling phytoplankton photosynthesis

The process of photosynthesis requires the energy from sunlight, and takes place essentially in the euphotic layer of the oceans. For ecosystem analysis, the meaningful quantity to retrieve is the daily water column primary production, in mg of carbon fixed per m^2 per day. Several numerical methods have been described to estimate primary production in marine waters (see Behrenfeld and Falkowski 1997), all differing to some extent according to their resolution in depth and irradiance. Friedrichs et al. (2008) distinguished four categories of models: depth-integrated,

[1]European Commission - Joint Research Centre, Institute for Environment and Sustainability, Via E. Fermi 2749, I-21027 Ispra, Italy. *Email addresses:* frederic.melin@jrc.ec.europa.eu and nicolas.hoepffner@jrc.ec.europa.eu

wavelength-integrated models; depth-resolved but wavelength integrated models; depth-integrated but wavelength-resolved models; and models resolving both the depth and the irradiance wavelength. For the purpose of this exercise, the model used fits within the fully resolved category, following the developments by Platt and Sathyendranath (1988) as implemented at global scale by Longhurst et al. (1995). A commonality in many of these models is the requirement for a suitable knowledge of the light field and phytoplankton biomass at any given location, depth and time. The instantaneous rate of photosynthesis or primary production is commonly formulated as:

$$PP(z,\lambda,t) = f[B(z),\phi(\lambda,z),E_{PAR}(\lambda,t)] \tag{6.1}$$

where B is the phytoplankton biomass commonly indexed by the concentration of chlorophyll-a, ϕ measures the physiological capacity of phytoplankton organisms to perform photosynthesis considering the surrounding conditions, and E_{PAR} is the total irradiance available for photosynthesis between 400 and 750 nm.

6.2.2 Estimation of surface irradiance

The estimation of surface irradiance and the modelling of its propagation through the water column are key aspects of oceanography. This is particularly true in the spectral range 350–700 nm that defines the photosynthetically available radiation, PAR. Assuming that this spectral interval represents roughly half of the total solar flux at the ocean surface, total PAR could be derived simply from a global database of solar fluxes, such as the International Satellite Cloud Climatology Project (ISCCP, Schiffer and Rossow 1983). Another method is to obtain PAR directly from ocean-colour satellites (Frouin et al. 2003). However, the selected model of primary production for this exercise requires a complete description of the spectral and angular characteristics of the incident light. Ignoring these properties could result in a significant bias in the light absorption by phytoplankton and subsequent errors in the final results (Kyewalyanga et al. 1992).

The formalism used here to calculate the incident light at the sea surface was originally described by Bird and Riordan (1986) and adapted by Platt and Sathyendranath (1988) for its implementation in marine primary production modelling. Gregg and Carder (1990) have completed this model for purely oceanographic applications with a spectral resolution for direct and diffuse irradiance of 1 nm over the interval 350–700 nm. In the case of clear sky, the direct [$E_{dd}(\lambda)$] and diffuse [$E_{ds}(\lambda)$] components of the irradiance are formulated separately as:

$$E_{dd}(\lambda) = \mu_0 E_0(\lambda) T_r(\lambda) T_a(\lambda) T_{03}(\lambda) T_{02}(\lambda) T_w(\lambda) \tag{6.2}$$

$$E_{ds}(\lambda) = E_{dsr}(\lambda) + E_{dsa}(\lambda) \tag{6.3}$$

where μ_0 is the cosine of the sun zenith angle, and E_0 the extra-terrestrial solar irradiance. The direct light path through the atmosphere is modified according to the transmittance properties of various compounds, including Rayleigh scattering (T_r), aerosol extinction (T_a), as well as ozone (T_{03}), water vapor (T_w), and oxygen (T_{02}) absorption. The diffuse component is the sum of the contributions from the molecules (Rayleigh scattering) E_{dsr} and the aerosols E_{dsa}.

All transmittance functions are calculated using meteorological variables either directly available from satellite data or from climatological databases. Under clear sky conditions, an accurate description of the aerosol optical properties and their distribution in time and space is a necessary requirement to estimate the irradiance at the surface. Satellite-based ocean colour radiometry has the capacity to provide aerosol characteristics (optical thickness and Ångström exponent), with an appropriate resolution in time and space to monitor their variability over the oceans.

The effect of clouds on the surface light field is three fold. They i) lower the irradiance intensity at the sea surface; ii) change the shape of the irradiance spectrum; and iii) reinforce the diffuse part of the irradiance with respect to the direct component. These effects can be modelled if appropriate information on clouds is available, such as the cloud optical thickness and structure derived by remote sensing, or the value of the albedo of the ocean-cloud system, for instance known with the distribution of reflectivity in the UV as provided by TOMS (McPeters 1998).

6.2.3 Underwater light field

Estimating primary production in the entire illuminated layer of the ocean requires some knowledge of the light field at any depth within the water column up to a level of minimum sunlight (i.e. euphotic depth). This is done through a bio-optical model which accounts for both the optical properties inherent to the water itself and material in suspension (absorption and scattering), and the distribution /geometry of the light field.

6.2.3.1 Water optical properties

As the sunlight penetrates in the water column, its magnitude and spectral quality is altered by water molecules (w) and optically significant constituents like phytoplankton (ph), non-algal particles (np) (detritus, minerals) and a coloured fraction of the total dissolved organic matter ($cdom$). The total absorption [$a(\lambda)$] and scattering [$b(\lambda)$] coefficients of the water are then:

$$a(\lambda) = a_w(\lambda) + a_{ph}(\lambda) + a_{np}(\lambda) + a_{cdom}(\lambda) \tag{6.4}$$

represented by the sum of the optical properties inherent to each of these constituents.

$$b(\lambda) = b_w(\lambda) + b_{ph}(\lambda) + b_{np}(\lambda) \tag{6.5}$$

In practice, the bio-optical model assumes Case 1 waters where the inherent optical properties of the constituents co-vary with phytoplankton concentration.

The absorption spectrum of phytoplankton, $a_{ph}(\lambda)$, between 400 and 750 nm is characterized by a continuous envelope reflecting a strong coupling in the energy transfer between photosynthetic pigments to the photosystems. The spectral shape and magnitude of the absorption coefficient is parameterized as a function of the chlorophyll concentration according to Bricaud et al. (1995), statistically representative of various marine conditions. The formulation accounts for differences in the composition of pigments within the phytoplankton cells, as well as in cell size (package effect) which translates to a flattening effect of $a_{ph}(\lambda)$ for large-cell phytoplankton communities.

For non-algal particles and dissolved organic substances, the spectral absorption obeys a similar exponential curve defined by the absorption coefficient at a reference wavelength and its slope in the lower part of the spectrum (400–440 nm). The curve parameters for $a_{np}(\lambda)$ are parameterized as a function of the chlorophyll-*a* concentration according to Bricaud et al. (1998). In the case of $a_{cdom}(\lambda)$, the bio-optical model assumes a constant slope and an amplitude of the absorption coefficient at 440 nm equivalent to a fixed ratio of the total absorption by particles and pure sea water.

The absorption due to pure sea water, $a_w(\lambda)$, plays a large role in the photon budget calculation, particularly in the red part of the visible spectrum where it reaches maximal values. In the blue part of the spectrum, the absorption coefficient of water molecules is used to determine the level of the euphotic depth, hence the productive layer.

With respect to scattering properties, a clear identification of the particles responsible for the optical signal remains difficult. In the estimation of primary production, scattering properties are calculated for total particulate matter, i.e. phytoplankton and non-algal particles, based on a statistical regression between chlorophyll-*a* concentration and the scattering coefficient at 550 nm (Loisel and Morel 1998). Scattering by dissolved substances is assumed to be negligible.

6.2.3.2 Propagation of the light in the water column

The vertical propagation of the light field is modelled according to Sathyendranath and Platt (1988; 1989), taking into account the attenuation coefficients for direct and diffuse light. The geometry of the light field is expressed through the mean cosine of light propagation weighted by the direct and diffuse component of the

downwelling irradiance. The objective of this exercise is to estimate the light flux received by a unit volume of water from all directions, the so-called scalar irradiance, which is the quantity useful for photosynthesis.

6.2.4 Model implementation

Measuring the water column primary production from space also requires some knowledge of parameters that are not accessible from satellite, such as the vertical profile of phytoplankton biomass, as well as other optically-significant constituents, and the photosynthetic parameters reflecting the capacity of phytoplankton communities to assimilate dissolved inorganic carbon through photosynthesis. These parameters have to be retrieved from field observations and their interpolation to meet the spatial and temporal resolution of satellite data are a key step of the work.

6.2.4.1 Biomass depth profile

The absorption and scattering coefficients, as well as the attenuation of light through the water column, are functions of the chlorophyll concentration. Two options can be considered for the vertical distribution of phytoplankton biomass: i) the vertical distribution of the phytoplankton biomass is uniform in a well-mixed surface layer, therefore the chlorophyll concentration at any depth is equivalent to that at the surface (possibly retrieved by satellite), and ii) in stratified conditions, a subsurface maximum usually occurs at depths ranging from close to the surface down to the bottom of the euphotic layer (i.e., 1% or 0.1% light level). The vertical distribution of the phytoplankton biomass in this case is represented by assuming a Gaussian distribution superimposed on a background chlorophyll concentration (Sathyendranath and Platt 1989). Its application in our primary production model requires *a priori* knowledge of three additional parameters defining the Gaussian curve.

6.2.4.2 Photosynthetic parameters

The relationship between the rate of carbon assimilation by phytoplankton and the submarine irradiance is described by a well-known photosynthesis-light model. More specifically, the primary production normalized to chlorophyll concentration is a function of scalar irradiance, described through a curve (P-E curve) defined by two parameters: the photosynthetic rate at light saturation (or assimilation number, $P_m{}^B$) and the initial slope of the curve (light-limited photosynthetic rate, α^B). A number of mathematical formalisms have been proposed to describe the P-E curve, starting with a 2-step linear function (Blackman 1906), to hyperbolic tangent (Jassby and Platt 1976), and exponential formulations with or without photoinhibition (Platt et al. 1980). The photosynthetic parameters issued from statistical

regression on field measurements using one or another of these formalisms reflects the physiological characteristics of the phytoplankton community under specific environmental factors.

6.2.4.3 Biogeographical provinces

Applying satellite data to retrieve the water column daily primary production requires specification of the five parameters described above (three describing the vertical structure of the biomass profile and two for the photosynthetic efficiency) on a pixel-by-pixel basis. Different options can be considered when assigning the parameters: i) constant values of the parameters at all locations and time; ii) the parameters are continuously variable, responding in the same way to changes in the forcing factors or; iii) some regional differences in the relationship between the parameters and the forcing factors constrict the assignment of the parameters to some ecological provinces, well defined in time and space. Substantial variability has been observed in the parameters of the biomass profile (Morel and Berthon 1989; Uitz et al. 2006), as well as the photosynthetic parameters (Kyewalyenga et al. 1998; Forget et al. 2007). In light of these *in situ* measurements, assigning a constant value to the parameters is therefore not appropriate. The application of a global smooth function relating each, or a combination of these parameters, to physical variables would be ideal, especially if the physical variables can be retrieved from satellite. Morel and Berthon (1989) provided solutions to retrieve the Gaussian parameters of the biomass profile from surface chlorophyll, which was used as an indicator of the trophic state. These relationships were then confirmed by Uitz et al. (2006) using a different data set.

On the other hand, the relationships between phytoplankton physiology and physical variables are more complex. Spatial discontinuities in the photosynthetic parameters are perceptible, reflecting regional diversity in the phytoplankton community response to physical forcing (Bouman et al. 2005). One technique suggested by Platt and Sathyendranath (1988), consists of partitioning the studied area into several provinces, each having its own set of the required parameters. Within each province, the parameters are either assumed constant for a given time period, e.g. seasons (Longhurst et al. 1995; Sathyendranath et al. 1995) or vary continuously with the physical conditions (Platt et al. 2008).

6.3 Demonstration: Application to global primary production

The primary production budget is calculated for three different months in 2006 and given for the global ocean, as well as selected basins. The processing starts with the global estimation of the sun irradiance at the surface and satellite-derived

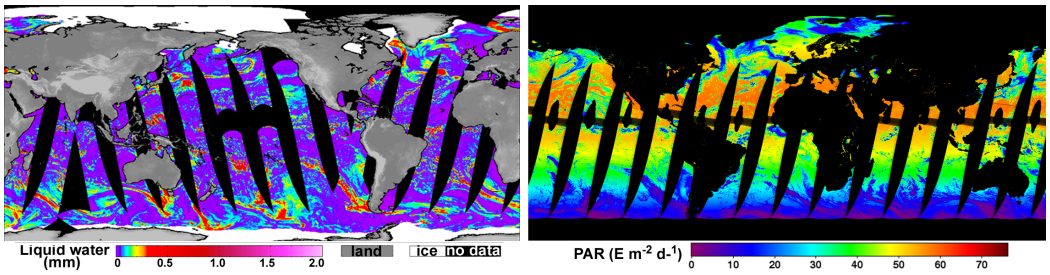

Figure 6.1 Daily maps of cloud liquid water path, LWP (left panel) and photosynthetically available radiation, PAR (right panel) for May 8, 2006.

chlorophyll concentration. These are inputs to the local model of primary production which, after selection of the parameters, will then be integrated over time (first over a day), depth and wavelength to yield a monthly map of daily water-column primary production.

The geophysical products necessary for the calculation of irradiance in the case of a clear sky can be identified as: i) atmospheric pressure, relative humidity, precipitable water vapor, and wind at the water surface; ii) ozone concentration; iii) aerosol characteristics. The values for the first group are provided as meteorological products by NCEP (National Center for Environmental Prediction, http://www.ncep.noaa.gov/), with a spatial resolution of 1°×1° (only the NCEP map given at noon is used). The ozone concentration is available through TOMS (Total Ozone Mapping Spectrometer, http://toms.gsfc.nasa.gov/) with a spatial resolution of 1.25° in longitude and 1° in latitude, which is extrapolated onto a grid of 1°×1°. The aerosol characteristics are provided on a monthly basis by the SeaWiFS products (~9 km resolution, as provided by the GSFC- DAAC, Goddard Space Flight Center, Distributed Active Archive Center, http://oceancolor.gsfc.nasa.gov). Since this temporal frequency does not guarantee a complete coverage, the SeaWiFS aerosol maps are re-gridded onto maps of reduced spatial resolution (1°).

For cloudy sky, it is assumed that the value of the albedo of the ocean-cloud system is known with the distribution of reflectivity (at 360 nm) provided by TOMS (McPeters 1998). The value of reflectivity provided by TOMS is then compared to the content of a look-up table of solutions of the radiative transfer problem for the cloud layer, pre-computed for various values of cloud liquid water path (LWP, Figure 6.1). The associated value of LWP immediately provides the value of transmittance for direct light from the same look-up table of pre-computed solutions of the radiative transfer problem with the cloud layer. Total direct irradiance is finally calculated as the direct irradiance for clear sky weighted by the direct transmittance under cloud conditions (Figure 6.2).

The surface chlorophyll concentration or phytoplankton biomass can be obtained directly from various ocean colour sensors and data archives, at the appropriate space agencies (e.g., http://oceancolor.gsfc.nasa.gov/). In the case of SeaWiFS

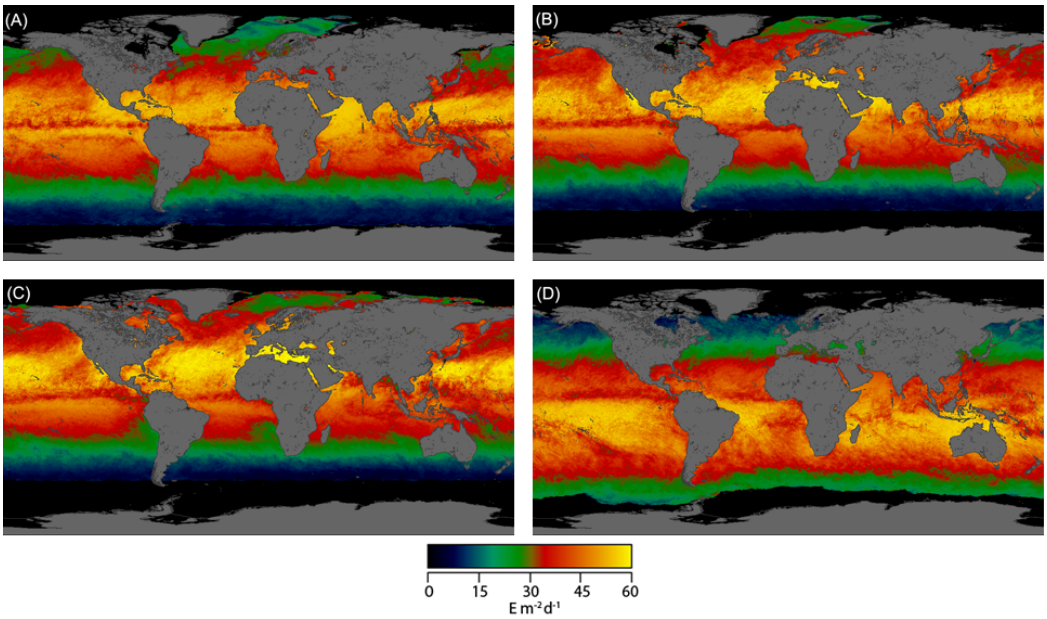

Figure 6.2 Monthly composites of daily photosynthetic active radiation (PAR) as computed directly from SeaWiFS data for April (A), May (B), July (C) and October (D), using top-of-atmosphere radiance to infer the attenuation of solar irradiance through the atmosphere (Frouin et al. 2003). Units are Einstein m^{-2} day^{-1} with a scale typically ranging from 0 to 60. One "Einstein" is equivalent to one mole of photons.

and MODIS chlorophyll products, daily standard mapped image (SMI) Level 3 (Figure 6.3) are distributed in a global equidistant cylindrical projection (or sinusoidal equal area grid for MERIS data) with a spatial resolution of 4320 pixels in longitude and 2160 pixels in latitude. The resolution is ca. 0.0833, equivalent to 9.28 km at the equator. For global and regional analysis, higher resolution data can be obtained by processing Level 1-A data with dedicated software packages freely available from space agencies (e.g., SeaDAS, `http://oceancolor.gsfc.nasa.gov/seadas/`; and BEAM, `http://www.brockmann-consult.de/cms/web/beam/software`).

Having defined the surface photosynthetically active radiation and phytoplankton biomass, we now need to specify the five parameters required to obtain the water-column integrated daily primary production i.e. three parameters to describe the vertical structure of the phytoplankton biomass, and two parameters to describe the photosynthetic efficiency of the organisms.

In this exercise, the primary production model uses a partition of the global ocean into biomes and provinces (Longhurst 1998; Figure 6.4), based on factors such as light conditions, circulation patterns, nutrient inputs, the bathymetry and other elements linking our current knowledge on regional oceanography to the response of phytoplankton to physical forcing. Statistical analyses are performed on the available *in situ* databases to retrieve the most representative set of parameters for

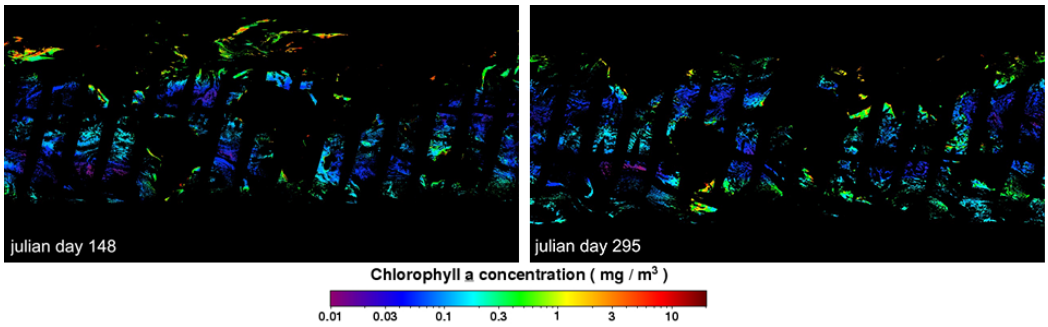

Figure 6.3 Daily scenes of Level 3 chlorophyll product as processed from SeaWiFS for day 148 (May 28, 2006) and day 295 (Oct. 22, 2006).

each of the provinces and/or biomes that will be assumed to remain constant for an appropriate time period (e.g. seasons).

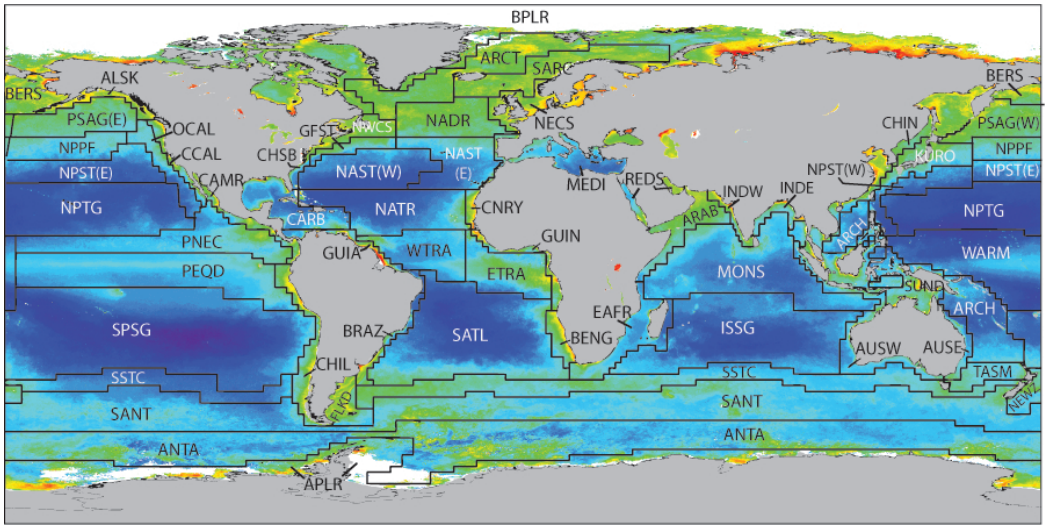

Figure 6.4 Distribution of the Longhurst oceanographic provinces adopted for the global ocean. Definition and acronyms of the provinces are detailed in Longhurst (1998; 2006).

Equation 15.1 can now be used to calculated primary production from daily scenes of surface chlorophyll concentrations, applying a spectral model to estimate the underwater light field at a given time and depth interval within the euphotic zone. The final output is the water-column integrated daily rate of primary production given in g C m^{-2} d^{-1}.

6.4 Questions

Q1: Based on Figure 6.2 and the section on estimation of surface irradiance (Section 6.2.2), what would be the primary and secondary drivers of PAR (photosynthetically active radiation) on a global scale?

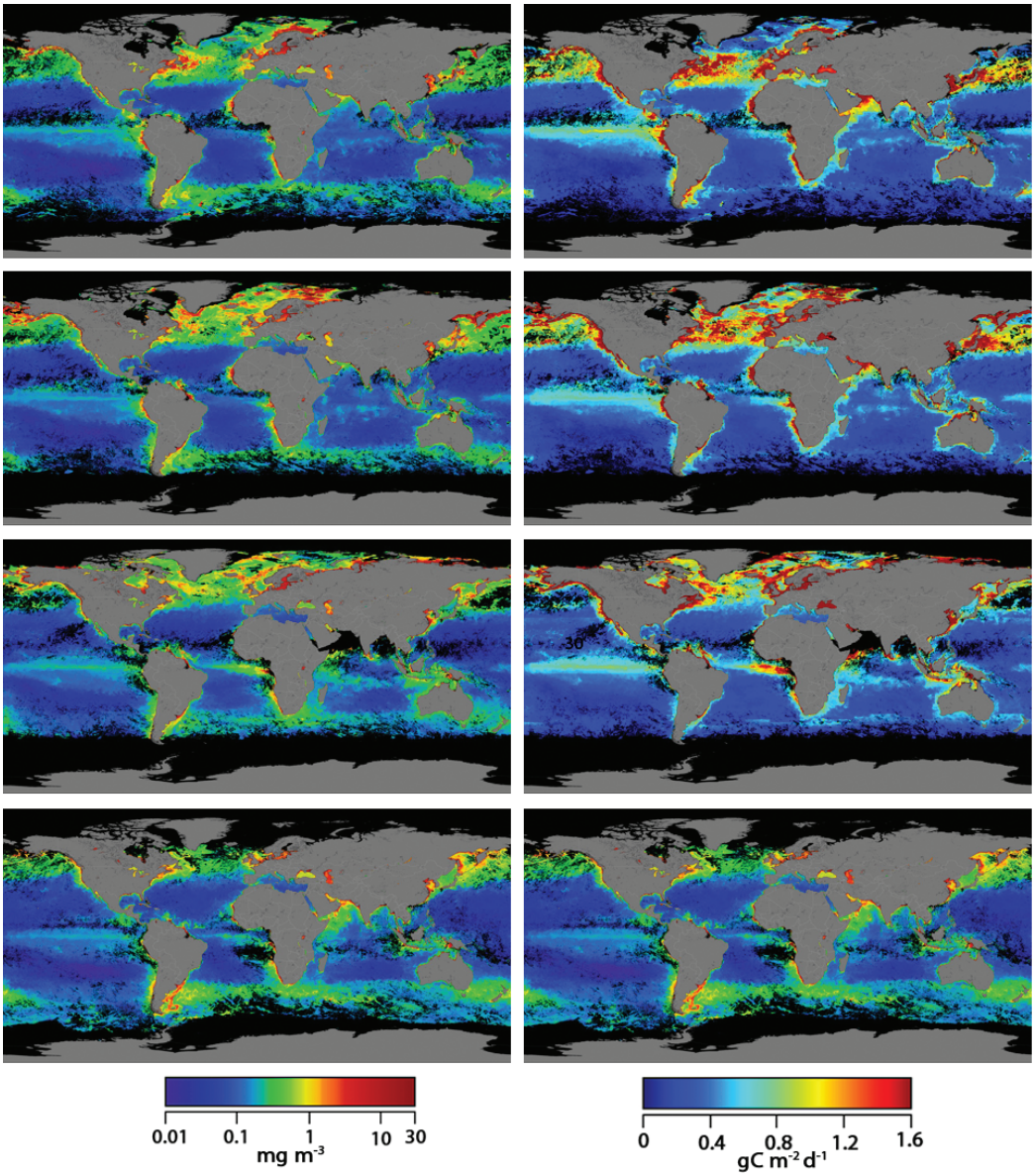

Figure 6.5 Global monthly composites of surface chlorophyll concentration (left panel) and primary production (right panel) as derived from SeaWiFS data for April, May, July and October 2006. Areas in black have no data.

Q2: What are the main drivers of primary production on a global scale? Discuss this by comparing the maps for primary production (Figure 6.5 right panel) with those of PAR (Figure 6.2) and chlorophyll concentrations (Figure 6.5 left panel).

Q3: What are the reasons for lack of data for Chla and primary production on Figure 6.5?

Q4: Looking at the maps in Figure 6.5, what are the main features you can observe in terms of temporal and spatial variability?

Q5: High primary production can be seen in coastal zones and marginal seas. Why is it consistent with expectations? Given the models presented above, why is the uncertainty on the derived primary production likely to be higher?

Q6: Looking at the global maps of primary production and zooming in on some regions, e.g. southeastern Africa and the Agulhas Current (Figure 6.6), what can you say about some of the surface features?

Q7: At what level of accuracy can primary production be retrieved using satellite data?

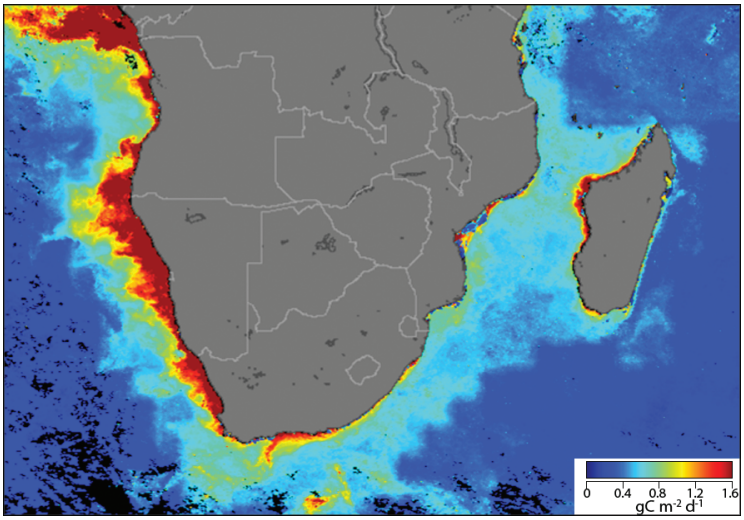

Figure 6.6 Primary production along South Africa-Madagascar region (extracted from the global map in Figure 6.5)

6.5 Answers

A1: On a theoretical basis, the solar irradiance at the top-of-atmosphere is proportional to the cosine of the solar zenith angle. The irradiance value at the sea surface is therefore directly affected by the solar angle. In turn, the solar zenith angle is a

function of latitude and day of the year (or season). PAR intensity and day length thus vary with location and season, which can be seen when comparing Figures 6.2c and d: the zone of maximum PAR shifts in latitude with season.

The other main driver of PAR is cloud cover. It changes the PAR amplitude, spectral shape at the surface, and geometry (diffuse-to-direct ratio). Aerosols have a similar effect, even though it is less pronounced, except in cases of strong aerosol events linked with desert dust or biomass burning. In general, these secondary effects are seen in the figures by zonal variations of PAR at a given latitude (Figure 6.2). A persistent feature is the relative minimum in PAR found slightly north of the Equator. This should be a region of maximum PAR, but it is characterized by a recurrent cloud cover associated with the Inter-Tropical Convergence Zone, where convection generates clouds.

A2: Phytoplankton biomass or chlorophyll concentration is the main driver of primary production. This is further modulated by PAR. If PAR was the dominant controlling factor, areas at subtropical latitudes with high PAR would show high productivity, which is generally not the case. At these latitudes, heat energy from the more intense sunlight is absorbed in the upper layers of the ocean, leading to a quasi-persistent stratification of the water column. This structure would prevent any supply of new nutrients from the deep oceans to the productive illuminated surface layer, thus keeping the productivity at low levels based on locally regenerated nutrients.

At higher latitudes, stratification of the water column occurs in spring as temperature increases, subsequently trapping large amount of nutrients from winter mixing in the euphotic layer. Favourable conditions of nutrients and light trigger phytoplankton blooms and productivity as seen in Figure 6.5 in the April and May composites.

A3: Lack of data in monthly composites of phytoplankton biomass and primary production could result from:

1. Very low sun zenith angle in local winter: for example, the northern seas between Scandinavia and Greenland have significantly more coverage in April and May than in October (Figure 6.5). Processing of chlorophyll images, and hence the estimation of primary prodcution, is restricted to sun zenith angles lower than 70°. The sun zenith angle is a function of time, day number and latitude.
2. Persistent cloud cover: ocean colour sensors only perform in clear sky conditions. Time-composite mapping enables a better coverage of the area of interest, to some extent, increasing the probability of obtaining cloud free scenes over each pixel. Nevertheless, areas with no data are still visible in monthly maps (Figure 6.5), especially along the equator. This area corresponds to a zone of persistent cloud cover previously described (see Answer 1) as the

Inter-Tropical Convergence Zone.

3. Persistent thick aerosol plumes: as for clouds, important aerosol emission events such as desert dust plumes or biomass burning can prevent any signal from the water surface from reaching the satellite sensor. These events are recurrent along the west coast of Africa as wind blows over the Sahara and Sahel regions.

A4: On a global scale, the variability in primary production is driven by the seasonal cycle. Comparing productivity values in the North Atlantic in April-May with that in October clearly shows an intensification of phytoplankton production in spring. On the contrary, in the southern hemisphere, productivity at higher latitudes tends to be higher in the October map than in April-May. The mechanism associated with that seasonal cycle is partly explain in Answer 2. Another noticeable feature in Figure 6.5 is a narrow band of higher productivity along the equator. The prevailing currents, combined with the Earth's rotation generates an upwelling process, and nutrient-rich deep waters are lifted to the surface layers.

A5: Relative to open ocean waters, coastal and shelf areas receive large fluxes of nutrients from rivers, and from upwelling processes at the coast. Higher productivity in these waters is thus expected. The four major eastern boundary upwelling systems along the coast of north- and southwest Africa, California, and Peru are well identified in the primary production maps (Figure 6.5) as permanent features, although the strength of the upwelling process varies seasonally. Note that these upwelling systems account for only 5% of the global ocean, but support major world fisheries.

Caution should be taken in the interpretation of primary production values in coastal areas: the bio-optical model presented above follows the Case-1 water assumption, where optical properties co-vary with Chlorophyll-*a*. At the coast, the water can be optically more complex than the open ocean waters because of the large influence by the land system and catchment basins delivering significant amounts of dissolved and particulate material to the coast. These additional substances, evolving independently from phytoplankton, impact on the derivation of chlorophyll concentration from satellite using standard "case 1 water" algorithms, but also on the propagation of light through the water column, as they compete with phytoplankton for light absorption.

A6: Caution should be taken in the interpretation of some surface features observed in the primary production maps (e.g. staircase-like features, straight and squared angle fronts). These are methodological artifacts associated with the partition of the global ocean into specific biogeographical provinces, each of them having their own set of model parameters reflecting their ecological characteristics (Longhurst, 1998). To tackle regional issues, it may be necessary to re-examine in more detail, the interactions between physics and biology in the region and the annual variability

of the forcing fields, such that more realistic provinces can be established for the studied area. The number of provinces will depend on the knowledge of the regional oceanography and the availability of the data required for primary production calculation.

In Longhurst's original work, the provinces have geometrical shapes (Figure 6.4) with fixed boundaries in space and time, although some adjustment could be applied from year to year according to the variability of inter-annual forcings. As a result, sharp squared-like discontinuities occur between provinces. This artifact does not alter in any way the estimated value of the primary production for each province, which relies on careful selection of parameters. Various protocols have been developed for a more dynamic partitioning of the oceans, using remotely-sensed data to locate the province boundaries and enable their adjustment in real-time. Readers are referred to Report # 9 of the International Ocean Colour Coordinating Group (IOCCG, 2009) for the various approaches in addressing oceanic ecosystem classification.

A7: As mentioned in the introduction, several models to retrieve primary production from remotely-sensed data have been developed during the last two decades. The performance of these models, including the one described in this exercise, were analysed in a series of round-robin experiments aiming at an extensive comparative assessment of the models (Carr et al., 2006), and their validation against *in situ* measurements (Friedrichs et al., 2009; Saba et al., in press). The mean RMSD (root mean square deviation) of 21 ocean colour models was 0.29 relative to *in situ* primary production values collected in the tropical Pacific, with the model described here being amongst the best performing (Friedrichs et al., 2009). However, the model's success varies substantially from region to region (Saba et al., in press), and in general the performance is still limited by the accuracy of the input variables, particularly uncertainties in satellite-derived chlorophyll values.

6.6 References and further reading

Behrenfeld M, Falkowski P (1997) A consumer's guide to phytoplankton primary production models. Limnol Oceanogr 42: 1479-1491

Bird R, Riordan C (1986) Simple solar spectral model for direct-normal and diffuse horizontal irradiance. Sol Energy 32: 461-471

Bouman H, Platt T, Sathyendranath S, Stuart V (2005) Dependence of light-saturated photosynthesis on temperature and community structure. Deep-Sea Res I 52: 1284-1299

Bricaud A, Morel A, Babin M, Allali K, Claustre H (1998) Variations of light absorption by suspended particles with chlorophyll a concentration in oceanic (case 1) waters: analysis and implications for bio-optical models. J Geophys Res 103: 31033-31044

Bricaud A, Babin M, Morel A, Claustre H (1995) Variability in the chlorophyll-specific absorption coefficients of natural phytoplankton: analysis and parameterization. J Geophys Res 100: 13321-13332

Carr M-E, et al. (2006) A comparison of global estimates of marine primary production from ocean color. Deep-Sea Res II 53: 741-770

Dowell M, Platt T (eds) Partition of the Ocean into Ecological Provinces: Role of Ocean-Colour Radiometry. Reports of the International Ocean Colour Coordinating Group, No 9, IOCCG, Dartmouth, Canada

Forget M-H, Sathyendranath S, Platt T, Pommier J, Vis C, Kyewalyanga MS, Hudon C (2007) Extraction of photosynthesis-irradiance parameters from phytoplankton production data: demonstration in various aquatic systems. J Plank Res 29: 249-262

Friedrichs MAM et al. (2009) Assessing the uncertainties of model estimates of primary productivity in the tropical Pacific Ocean. J Mar Syst 76: 113-133

Frouin R, Franz B, Werdell P (2003) The SeaWiFS PAR product. In SB Hooker and ER Firestone (eds), NASA TM, 2003-206892, Vol 22, chap 8, pp 46-50 NASA-GSFC

Gregg W, Carder K (1990) A simple spectral irradiance model for cloudless maritime atmospheres. Limnol Oceanogr 35: 1657-1675

Jassby A, Platt T (1976) The relationship between photosynthesis and light for natural assemblages of marine phytoplankton. J Mar Res 12: 421-430

Kyewalyanga M, Platt T, Sathyendranath S (1992) Ocean primary production calculated by spectral and broad-band models. Mar Ecol Prog Ser 85: 171-185

Kyewalyanga M, Platt T, Sathyendranath S, Lutz VA, Stuart V (1998) Seasonal variations in physiological parameters of phytoplankton across the North Atlantic. J Plank Res 20: 17-42

Loisel H, Morel A (1998) Light scattering and chlorophyll concentration in case 1 waters: a reexamination Limnol Oceanogr 43: 847-858

Longhurst A, Sathyendranath S, Platt T, Caverhill C (1995) An estimate of global primary production in the ocean from satellite radiometer data. J Plank Res 17: 1245-1271

Longhurst A (1998) Ecological geography of the sea, pp 398. San Diego: Academic Press.

IOCCG (2009) Partition of the Ocean into ecological provinces: role of ocean colour radiometry. Dowell M, Platt T (eds) Reports of the International Ocean Colour Coordinating Group, No 9, IOCCG, Dartmouth, Canada

McPeters R, et al. (1998) Earth Probe Total Ozone Mapping Spectrometer (TOMS) data user's guide. In NASA TM, 1998-206895, pp 1-64 NASA-GSFC

Morel A, and J-F Berthon (1989) Surface pigments, algal biomass profiles and potential production of the euphotic layer: relationships reinvestigated in view of remote sensing applications. Limnol Oceanogr 34: 1545-1562

Platt T, Sathyendranath S (1988) Oceanic primary production: estimation by remote sensing at local and regional scales. Science, 241: 1613-1620

Platt T, Gallegos C, Harrison W (1980) Photoinhibition of photosynthesis in natural assemblages of marine phytoplankton. J Mar Res 38: 687-701

Platt T, Sathyendranath S, Forget M-H, White III GN, Caverhill C, Bouman H, Devred E, and Son S (2008) Operational estimation of primary production at large geographical scales. Rem Sens Environ 112: 3437-3448

Saba VS et al. (in press) Estimating marine primary productivity in coastal and pelagic regions across the globe: an evaluation of satellite-based ocean color models. Biogeosciences

Sathyendranath S, Platt T (1988) The spectral irradiance field at the surface and in the interior of the ocean: a model for applications in oceanography and remote sensing. J Geophys Res 93: 9270-9280

Sathyendranath S, Platt T (1989) Computation of aquatic primary production: extended formalism to include effect of angular and spectral distribution of light. Limnol Oceanogr 34: 188-198

Sathyendranath S, Longhurst A, Caverhill C, Platt T (1995) Regionally and seasonally differentiated primary production in the North Atlantic. Deep-Sea Res 42: 1773-1802

Schiffer R, Rossow W (1983) The international cloud climatology project (ISCCP): The first project of the Worlds Climate Research Program. Bull Amer Meteor Soc 64: 779-784

Uitz J, Claustre H, Morel A, Hooker SB (2006) Vertical distribution of phytoplankton communities in open ocean: an assessment based on surface chlorophyll. J Geophys Res 111: C08005, doi:10.1029/2005JC003207

Case Study 7

Red Tide Detection in the Eastern Gulf of Mexico Using MODIS Imagery

Chuanmin Hu*[1], Jennifer Cannizzaro[1], Kendall L. Carder[1], Zhongping Lee[2], Frank E. Muller-Karger[1] and Inia Soto[1]

7.1 Background

Many of the red tides (i.e., harmful algal blooms or HABs) in the eastern Gulf of Mexico (GOM) (24°–31°N, 90°–80°W) are caused by the toxic dinoflagellate, *Karenia brevis* (previously known as *Gymnodinium breve* or *G. breve*). Brevetoxins produced during *K. brevis* blooms can kill fish, mammals, and other marine organisms and cause respiratory irritation in humans (Hemmert, 1975; Asai et al., 1982; Landsberg and Steidinger, 1998; Kirkpatrick et al., 2004; Flewelling et al., 2005). *K. brevis* blooms can also adversely impact local tourism and commercial shellfish industries, leading to economic losses that have exceeded millions of US dollars during a single bloom event (Habas and Gilbert, 1974; Larkin and Adams, 2007).

Although *K. brevis* blooms can change the water to many different colours (e.g., brown, red, or even black) depending on the bloom's cell concentration and the concentration of other important optical constituents (Dierssen et al., 2006), they are commonly referred to as red tides. In the eastern GOM, red tides occur every year, mainly from late summer to early spring, yet their occurrence frequency, intensity, spatial extent, and duration all vary from year to year. Despite many years of community efforts, the mechanisms of initiation, maintenance and demise of red tides are still poorly understood and require further investigation. Data collected between the 1950's and the 1980's suggest that red tides are initiated offshore in nutrient-poor waters (Tester and Steidinger, 1997), and that they move toward shore by winds and currents, where they concentrate near fronts and utilize new nutrients from coastal runoff (Walsh et al., 2006). Several hypotheses that attempt to explain new nutrient supplies for these HABs have been proposed, including nitrogen fixation stimulated by atmospheric deposition of iron-rich Saharan dust particles

[1]College of Marine Science, University of South Florida, 140 7th Ave., S., St. Petersburg, FL 33701, USA. **Email address:* hu@marine.usf.edu

[2]Geosystems Research Institute, Mississippi State University, Stennis Space Center, MS 39529, USA

(Lenes et al., 2001; Walsh and Steidinger, 2001; Walsh et al., 2006), submarine groundwater discharge (Hu et al., 2006), and dead fish (Walsh et al., 2009). These hypotheses remain to be tested, and these possible sources need to be evaluated relative to sources such as upwelling of deeper GOM waters, riverine inputs, and benthic nutrient regeneration.

Timely information of *K. brevis* blooms is essential for all aspects of red tide studies, including testing hypotheses, assessing and managing the coastal environment, and forecasting and mitigation of red tides. In the past few decades, several long-term monitoring programs have invested significant resources in collecting red tide information. These include the Monitoring and Event Response for Harmful Algal Blooms (MERHAB) program supported by the U.S. NOAA (National Oceanic and Atmospheric Administration) and the Florida Fish and Wildlife Research Institute, several other programs supported by the state of Florida, local environmental groups, and volunteers. Most of these efforts rely on water sample analysis from field surveys because this is currently the only accurate means to differentiate *K. brevis* from other phytoplankton species. However, field surveys are often limited in spatial coverage and temporal frequency, especially during severe weather events. This lack of synoptic and frequent field observations makes it difficult to 1) provide near real-time information for rapid response, and 2) understand the long-term red tide occurrence statistics. For example, there has been substantial discussion and debate within the scientific community as to whether there is any historical trend in red tide occurrence along the west-central Florida coast. While Brand and Compton (2007) found that the frequency and duration of red tides appear to have increased in recent years, there was also argument (Christman and Young, 2006; Alcock, 2007) that this observation may simply be due to the unevenly distributed sampling scheme, the so-called observer effect (i.e. increased sampling during recent years because of increased public and scientific awareness - http://research.myfwc.com/features/view_article.asp?id=27095).

In addition to the intensive field sampling efforts, satellite remote sensing can offer synoptic and more frequent measurements, with imagery available in near real-time (Babin et al., 2008). Therefore, detection of red tides via remote sensing is highly desirable, and thus has been an active research topic. Satellite imagery already has been used for operational monitoring of HABs in the GOM region. Some of the disadvantages are that satellite remote sensing using visible radiance is limited by cloud cover, spatial resolution, lack of information with depth below the surface, and algorithm uncertainty. While the first three are inherent with a given satellite-based instrument and cannot be fully "corrected", there has been continuous progress in algorithm development to improve the accuracy in red tide detection. Here, using several examples, we demonstrate how to use Moderate Resolution Imaging Spectroradiometer (MODIS) satellite imagery to differentiate the various waters, including *K. brevis* red tides in the eastern GOM. We will begin by reviewing briefly the underlying principles of red tide detection from space, and

follow with descriptions of the data and methods. We show several examples to illustrate the potential of this technology.

7.1.1 Principles

The use of ocean-colour satellites for rapid detection of red tides in the eastern GOM has been described previously (e.g., Stumpf et al., 2003a; Tomlinson et al., 2004; 2008; Hu et al., 2005; Cannizzaro et al., 2008; Amin et al., 2009). *K. brevis* cells contain chlorophyll-*a* and accessory pigments. These pigments have reflectance spectra that allow them to be differentiated from other water constituents, such as suspended non-living particles. The chlorophyll-*a* content of *K. brevis* cells ranges from ~8.5 pg/cell for natural populations to ~25 pg/cell for cultured populations (Evens et al., 2001). Assuming 10 pg/cell, a concentration of $2x10^4$ cells l^{-1} implies 0.2 mg m^{-3} of chlorophyll-*a*, close to the clear-water background chlorophyll-*a* concentration (Chl-*a*) in the eastern GOM. Satellite ocean-colour instruments typically have a measurement precision (not accuracy) of 0.01 – 0.02 mg m^{-3} for blue waters. In order for a *K. brevis* bloom to be detected and identified as such, however, Chl-*a* needs to exceed 0.5 – 1 mg m^{-3}, corresponding to *K. brevis* cell concentrations of $5x10^4$ to 10^5 cells l^{-1}. These concentrations are high enough to cause fish kills (Steidinger et al., 1998).

Satellite-derived Chl-*a* data products can be used to identify areas of possible red tides. For example, a Chl-anomaly technique was proposed by Stumpf et al. (2003a) to flag "new" blooms in an area relative to conditions two weeks earlier — under certain conditions these new blooms can be flagged as potential *K. brevis* blooms.

There are practical difficulties when applying the Chl-based approach to identify red tides in the eastern GOM using remote sensing data. The first is the difficulty with obtaining an accurate chlorophyll estimate in many coastal waters because of errors in the atmospheric correction algorithms (to remove atmospheric effects from the spectral satellite signal) and bio-optical inversion algorithms (to convert the surface spectral signal to Chl-*a* and other bio-optical parameters). In these waters, the optical signal may not be dominated by phytoplankton, but instead by coloured dissolved organic matter (CDOM) from *in situ* phytoplankton degradation or terrestrial runoff, resuspended sediments, and/or the bottom effects in clear, shallow water. The empirical band-ratio OC4 algorithm (O'Reilly et al., 2000; version 4) that is used to convert the surface spectral signal to Chl-*a* does not differentiate between optically important constituents, but rather regards all influences as originating from Chl-*a*. This causes large errors in the Chl-*a* estimates for the eastern GOM coastal waters (Hu et al., 2003; 2005). Although a semi-analytical algorithm designed for MODIS (Carder et al., 1999) can separate CDOM from Chl-*a* and thus improve Chl-*a* estimates in clear and moderately turbid waters (Hu et al., 2003), in highly turbid coastal waters the algorithm switches to an empirical blue/green band-ratio form.

The second difficulty is differentiating *K. brevis* blooms from other phytoplankton blooms. Chl-*a* cannot be used for this task because both types of blooms contain high Chl-*a*. Discrimination between *K. brevis* and other phytoplankton groups using *in situ* optical observations has been done with some success (Cullen et al., 1997; Millie et al., 1997; Lohrenz et al., 1999; Schofield et al., 1999; Kirkpatrick et al., 2000). However, these techniques require hyperspectral data (e.g., Craig et al., 2006), which are not available from satellites. Several HAB detection techniques have been proposed that can use multi-spectral satellite data. These include methods involving particulate backscattering (Cannizzaro et al., 2008), spectral curvature (Tomlinson et al., 2008), a combination of red-wavelength bands (Amin et al., 2009), and image segmentation (Zhang et al., 2002).

In this demonstration, we will combine the techniques proposed by Hu et al. (2005) and Cannizzaro et al. (2008). We used MODIS satellite data to show how to differentiate bloom waters from coastal waters in which other constituents dominate the optical signal, and to differentiate *K. brevis* blooms from other blooms. Specifically, we distinguished phytoplankton blooms from CDOM-rich waters by examining spectral water-leaving radiance and solar stimulated fluorescence (Hu et al., 2005), and *K. brevis* blooms were distinguished from non-*K. brevis* blooms by examining bloom backscattering efficiency (Cannizzaro et al., 2008).

7.2 Data and Methods

MODIS Level-1a data were obtained from the U.S. NASA Goddard Space Flight Center (GSFC) (http://oceancolor.gsfc.nasa.gov). These data are open to the public within a few hours (typically 3 – 6) of collection by the spacecraft. The following steps were used to generate georeferenced MODIS images at 1-km resolution:

1. MODIS/Aqua Level-1a data were processed to generate Level-1b (calibrated total radiance) data for the "ocean colour" spectral wavebands in the visible and near-infrared, and geolocation data using SeaWiFS Data Analysis System (SeaDAS) software. The 1-km bands were designed for the ocean with sufficient sensitivity to detect subtle changes in ocean colour. The Level-1b and geolocation data were stored in computer files in HDF (Hierarchical Data Format);
2. MODIS Level-1b data were atmospherically corrected to generate the spectral remote sensing reflectance ($R_{rs}(\lambda)$, sr^{-1}) and normalized water-leaving radiance (nLw(λ), mW cm^{-2} μm^{-1} sr^{-1}) using SeaDAS. These two parameters can be derived from each other using the extraterrestrial solar irradiance (time-independent constants). During this step, ancillary data (surface wind, pressure, total ozone thickness, and atmospheric water vapor content) were downloaded from NASA/GSFC and used to estimate the atmospheric contribution to the satellite-received radiance. The atmospheric correction was based on the two near-infrared (NIR) bands at 748 nm and 869 nm, from which atmo-

spheric properties were derived and used to estimate the properties at other wavelengths on a per-pixel basis (Gordon and Wang, 1994). Over turbid coastal waters, a modification to the atmospheric correction scheme was used that involves using an iterative approach to account for the non-zero water-leaving radiance in the NIR (Stumpf et al., 2003b);

3. The spectral $R_{rs}(\lambda)$ was used to derive two data products: Chl-*a* from an empirical band-ratio algorithm (OC4v4; O'Reilly et al., 2000); particulate backscattering coefficient at 551 nm (b_{bp},551) using a Quasi-Analytical Algorithm (QAA, Lee et al., 2002). Using nLw(λ) data from three MODIS wavebands at 667, 678, and 748 nm we derived the Fluorescence Line Height (FLH, mW cm^{-2} μm^{-1} sr^{-1}) product using a linear baseline algorithm (Letelier et al., 1996). Further, the empirically-derived Chl-*a* was used to estimate the particulate backscattering coefficient at 551 nm using the Morel (1988) algorithm, designed for phytoplankton dominated (i.e., Case 1) waters:

$$b_{bp,Morel} = 0.3 \times \text{Chl}^{0.62} \times (0.002 + 0.02 \times (0.5 - 0.25 \times \log_{10}\text{Chl})) \qquad (7.1)$$

4. These products $R_{rs}(\lambda)$, nLw(λ), Chl-*a*, $b_{bp,QAA}$, $b_{bp,Morel}$ and FLH) were georeferenced to a cylindrical equidistant (rectangular, also called geographic lat/lon) projection for the area of interest. The final images had a spatial resolution equivalent to 1-km per image pixel. The map-projected products were stored in HDF files. Individual products were also converted to raster image formats with an embedded palette using pre-defined colour look-up tables;
5. nLw(λ) data at 551, 488, and 443 nm were used as the red, green and blue channels to compose an Enhanced RGB (ERGB) image. The red waveband (667 nm) was not used because water-leaving radiance at this wavelength (nLw(667)) is very low except in sediment-rich waters, thus providing little information on red tides.

The Florida Fish and Wildlife Research Institute (FWRI) has compiled an *in situ* database for *K. brevis* cell concentration data. Water samples have been collected by various research and volunteer groups in the eastern GOM and analyzed using microscopic enumeration techniques. These data, although not continuous in either space or time, were used as ground-truth to help interpret the MODIS imagery. Below we demonstrate, step by step, how the various colour features are identified and interpreted from the MODIS imagery.

7.3 Demonstration

In 2005, a long-lasting, extensive red tide event occurred on the west Florida shelf (WFS, 24.5°–30.1°N and 85.1°–81.5°W), which may have been related to excessive rainfall in both 2004 and 2005 (Hu et al., 2006). The event started in January 2005

near Tampa Bay, Florida (Tampa Bay is marked as "A" in Figure 7.1a). Figure 7.1 shows several MODIS products from a scene collected on 21 January 2005, where the red tide patch can be seen.

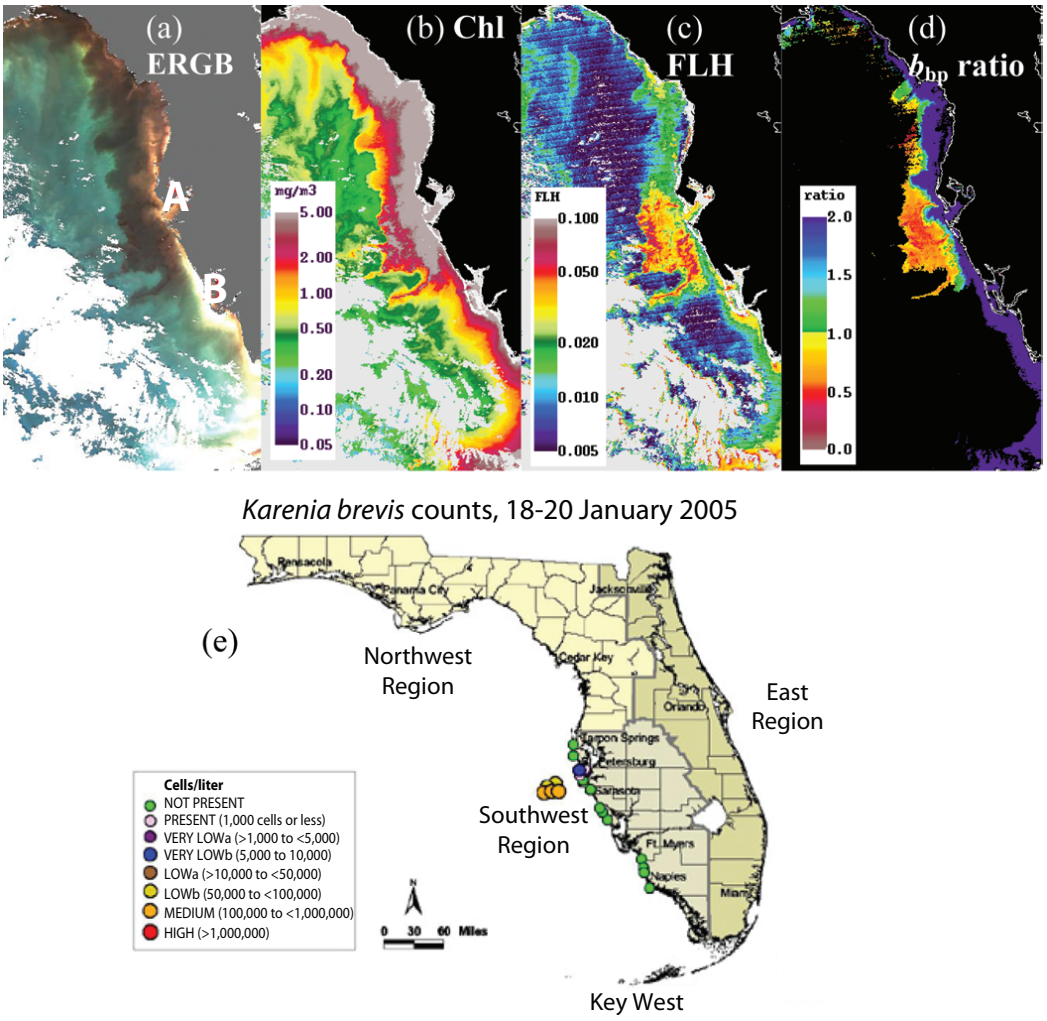

Figure 7.1 (a – d) MODIS images on 21 January 2005 showing a *K. brevis* bloom in coastal waters between Tampa Bay (A, 27.75°N, 82.56°W) and Charlotte Harbor (B, 26.75°N, 82.1°W). The images cover the area between approximately 24.5°–30.1°N and 85.1°–81.5°W. The various image types were generated using Steps 1 – 5 described in the Data and Methods section. In (d), the b_{bp} ratio is defined as $b_{bp,QAA}/b_{bp,Morel}$ (e) *K. brevis* concentration (in cells l^{-1}) obtained from FWRI (http://research.myfwc.com/gallery/image_details.asp?id=24764).

Figure 7.1a shows an ERGB image, where the dark colours result from increased light absorption in the blue wavelength (443 nm) due to high concentrations of CDOM and/or chlorophyll-*a*, and bright colours (light blue, yellow and white) result from suspended sediments and/or shallow bottom. The corresponding Chl-*a* image

in Figure 7.1b, derived from the blue-green band ratio algorithm, shows erroneously elevated Chl-*a* along the entire coast. In contrast, the FLH image in Figure 7.1c helps distinguish dark CDOM-rich waters (erroneously interpreted as high Chl-*a* in band ratio algorithms) from phytoplankton-rich waters. FLH is insensitive to CDOM (McKee et al., 2007). However, FLH is not a reliable parameter in sediment-rich waters (Gilerson et al., 2007). The high FLH values near Charlotte Harbor (Charlotte Harbor is marked as "B" in Figure 7.1a) for example, may in part be false interpretation of suspended sediments.

Figure 7.1 reveals: 1) Chl-rich waters (dark colour in ERGB with high FLH values); 2) CDOM-rich waters (dark colour in ERGB with low FLH values); 3) sediment-rich waters (bright colour in ERGB with high FLH values); and 4) shallow, clear waters (bright colour in ERGB with low FLH values). Of these, observations 3 and 4 are sometimes difficult to distinguish from each other, especially for very shallow waters (< 5 m water depth) because nLw in the fluorescence bands may also be influenced by benthic algae or sediments. This should not affect our interpretation because both cases are excluded as potential *K. brevis* blooms. Of the four, observation 1 represents waters with high biomass (Chl-*a*) and therefore can be *K. brevis* or other blooms. However, there are two drawbacks from this interpretation. The first is its qualitative nature. Indeed, the terms "high" and "low" only provide a relative sense. The second drawback is that it is impossible to tell if the high-FLH dark waters contain high concentrations of the toxic *K. brevis* or other phytoplankton species (such as diatoms).

To overcome these two difficulties, we first assume that FLH > 0.015 – 0.02 mW cm^{-2} μm^{-1} sr^{-1} can indicate bloom conditions and FLH < 0.01 – 0.015 represent non-bloom conditions (note that the values between 0.01 and 0.02 represent transition conditions). Observations from South Florida coastal waters suggest that a FLH value of 0.01 mW cm^{-2} μm^{-1} sr^{-1} is equivalent to about 1 mg m^{-3} Chl-*a* for the range of 0.4 – 4 mg m^{-3} ($Chl = 1.255 \times (FLH \times 100)^{0.86}$, r=0.92, n=77, Hu et al., 2005), although the relationship between FLH and Chl-*a* (a function of fluorescence efficiency) varies.

The technique proposed by Cannizzaro et al. (2008) was then used to examine the backscattering coefficient at 551 nm ($b_{bp,551}$) estimated with the QAA algorithm (Lee et al., 2002) in reference against $b_{bp,Morel}$ from a Case-1 empirical algorithm (Morel, 1988; Equation 7.1). Results are shown in Figure 7.1d. To exclude non-productive waters, pixels with Chl-*a* < 1.5 mg m^{-3} are masked as black. Because *K. brevis* blooms exhibit a lower backscattering efficiency compared to diatom blooms, the warm colours (yellow-red, with $b_{bp,551}/b_{bp,Morel} < 1.0$) in Figure 7.1d represent potential *K. brevis* blooms. Indeed, near concurrent *in situ* water sample analysis from FWRI confirms this finding (Figure 7.1e), where waters offshore of Tampa Bay showed medium concentrations of *K. brevis* cells (100,000 to <1,000,000 cells l^{-1}). Further, in nearshore waters there were no *K. brevis* found in these samples, consistent with the high b_{bp} ratios shown in Figure 7.1d. In other words, the high-

FLH values near Charlotte Harbor (sediment-rich water as identified by the bright colour in Figure 7.1a) is successfully discarded as potential *K. brevis* blooms in Figure 7.1d.

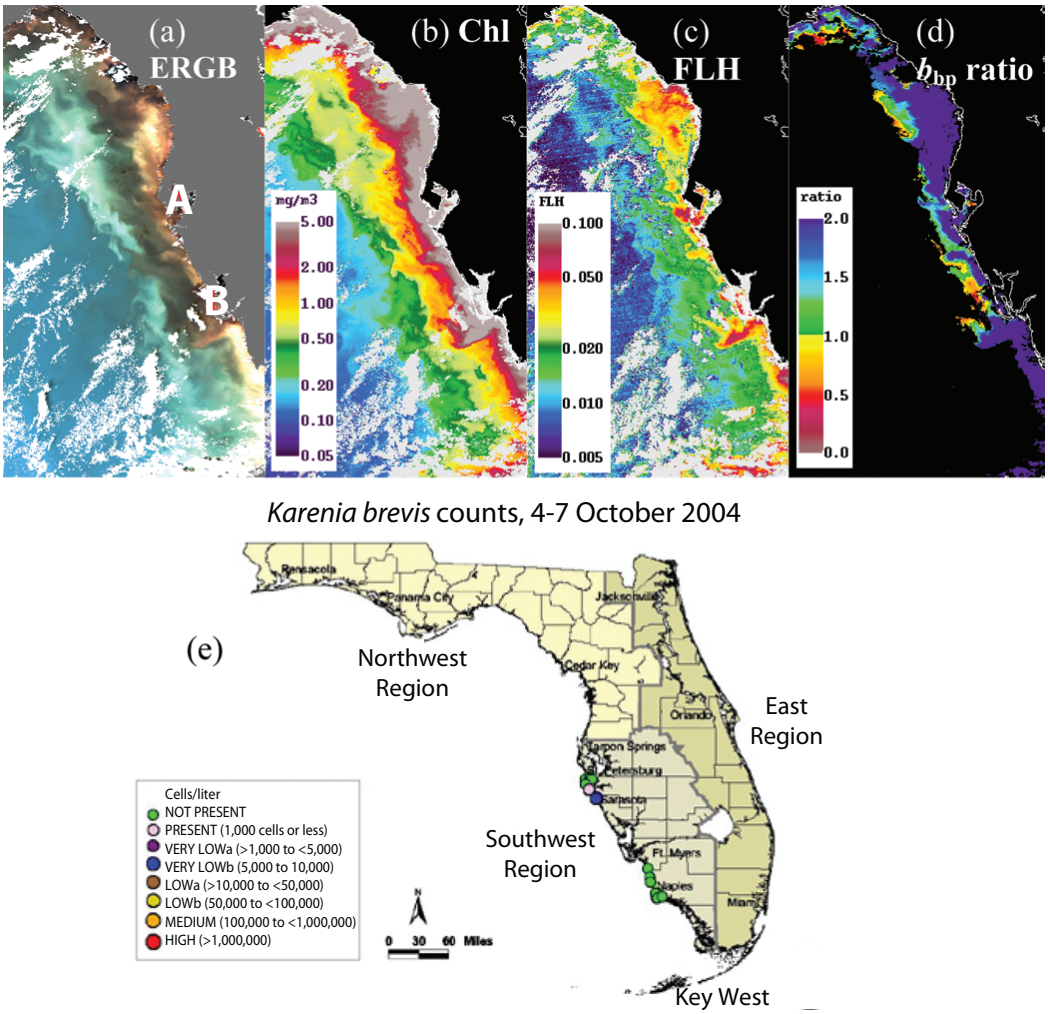

Figure 7.2 (a – d) MODIS images on 1 October 2004 showing diatom blooms off Tampa Bay (A, 27.75°N, 82.56°W) and Charlotte Harbor (B, 26.75°N, 82.1°W). The images cover the area between approximately 24.5°–30.1°N and 85.1°–81.5°W. The various image types were generated using Steps 1 – 5 described above in the Data and Methods section. In (d), the b_{bp} ratio is defined as $b_{bp,QAA}/b_{bp,Morel}$ (e) *K. brevis* concentration (in cells l^{-1}) obtained from FWRI (http://research.myfwc.com/gallery/image_details.asp?id=20058).

While Figure 7.1 demonstrates the multiple steps used to delineate *K. brevis* blooms in optically complex waters on the WFS, Figure 7.2 shows another case where the same technique is used to identify non-*K. brevis* (in this case, diatom) blooms. Figure 7.2a shows that, in less than one week after Hurricane Jeanne's passage on 26 September 2004, most of the WFS waters became enriched in CDOM/Chl-*a* and

suspended sediments, all interpreted as high Chl-*a* (Figure 7.2b). While the FLH image in Figure 7.2c shows potential blooms in nearshore waters, especially near the Tampa Bay and Charlotte Harbor mouths, the b_{bp} ratio image in Figure 7.2d indicates the possibility that these nearshore blooms are *K. brevis* blooms, is low. Although concurrent water sample data lack coverage of most shelf waters, the limited data in Figure 7.2e confirms that the high FLH patches near Tampa Bay and Charlotte Harbor mouths are non-*K. brevis* blooms. Indeed, the FWRI database showed 0 cells l^{-1} of *K. brevis* but very high levels (up to 230,000 cells l^{-1}) of *Pseudonitzschia* (a toxic diatom) in water samples collected from piers/beaches off Tampa Bay (e.g. Mullet Key, Anna Maria Island, Skyway fishing pier, offshore Egmont Key) between 2–7 October 2004. In this case, the image set used here not only identifies blooms, but also recognizes non-*K. brevis* blooms. Combined with the results shown in Figure 7.1, we can conclude that this technique is efficient, at least for the two cases presented here, in delineating the following waters: Chl-rich, sediment-poor waters; CDOM-rich, Chl-poor waters; sediment-rich and/or shallow, clear waters; *K. brevis* and other bloom waters.

7.4 Training

To help prepare and interpret MODIS imagery, we now go through each step to generate the various types of MODIS images from a map-projected MODIS Level-3 HDF data file. The MODIS data (Figure 7.3) were collected on 7 October 2006, where ERGB, Chl-*a*, FLH, and b_{bp} ratio images are presented in Figures 7.3a-d, respectively. The following steps were used in SeaDAS for image generation, visualization, and interpretation, but any other software package that has basic image processing capabilities and HDF compatibility can also be used.

Step 1: Download the MODIS Level-3 HDF data file from the IOCCG website (`http://www.ioccg.org/handbook/Hu_red/`) and open in a SeaDAS Display window. Load the three bands nLw_443, nLw_488, and nLw_551 in the "Band List Selection Window." Then, under Utilities => Data Visualization => Load True Color Image, choose "Band List" instead of "Input File." Choose band numbers 3, 2, 1, for the R, G, B channels, respectively. Enter 10 for slopes and 0 for intercepts. Load the RGB channels in the "Band List Selection" window, and display the true colour image. An image similar to Figure 7.3a should appear in a separate window. A high-resolution coastline can be overlaid on the image by selecting Setups => Coastline. The final image can be saved as an 8-bit png image (colour coded 2-dimensional image) or a 24-bit png image (3-dimensional image) under Functions => Output => Display.

Step 2: Use the same method in Step 1 above to load the "chlor_a" data product from the HDF file into the "Band List Selection Window," and display the image in a separate window. The colour shades in this window appear strange because of the

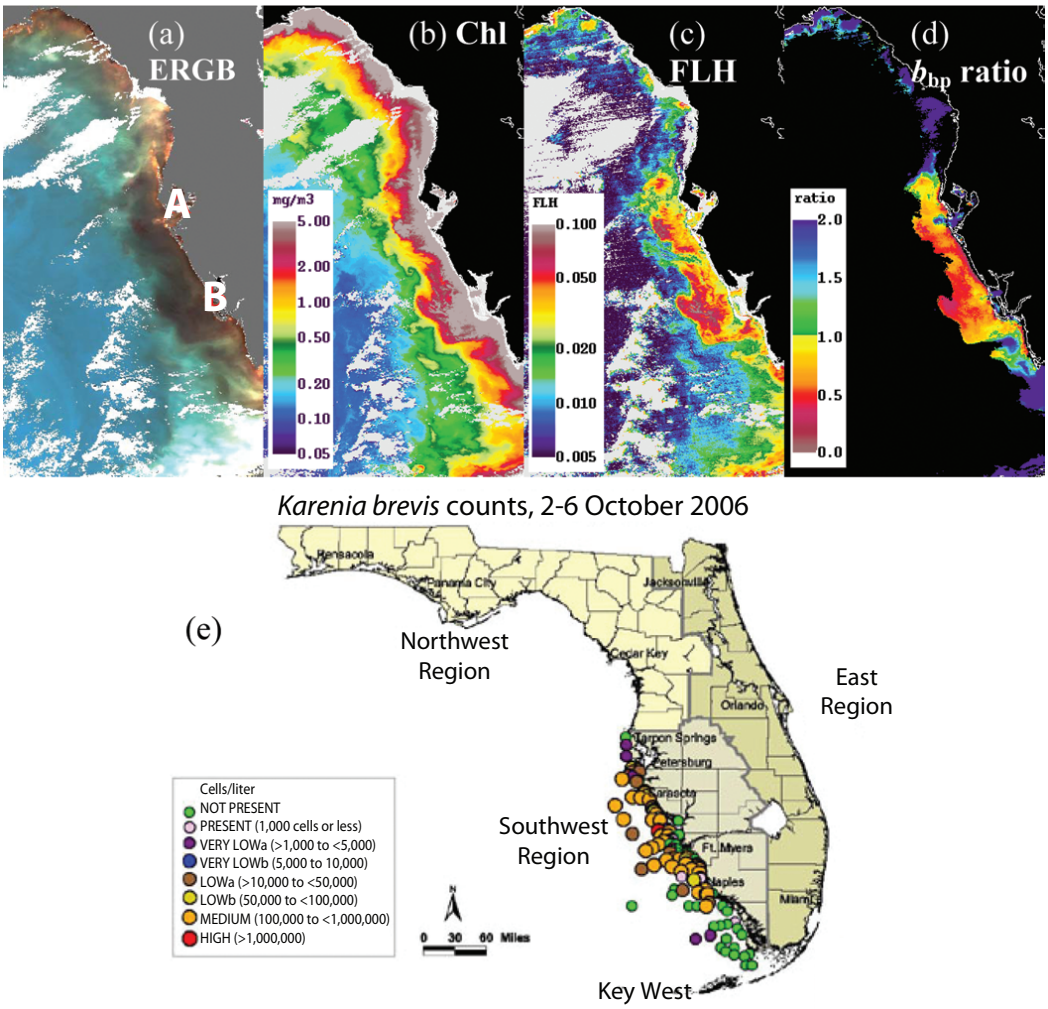

Figure 7.3 (a – d) MODIS images on 7 October 2006 showing *K. brevis* blooms off the central west Florida between Tampa Bay (A, 27.75°N, 82.56°W) and Charlotte Harbor (B, 26.75°N, 82.1°W). The images cover the area between approximately 24.5°–30.1°N and 85.1°–81.5°W. The various image types were generated using Steps 1 – 5 described in the Data and Methods section. In (d), the b_{bp} ratio is defined as $b_{bp,QAA}/b_{bp,Morel}$ (e) *K. brevis* concentration (in cells l^{-1}) obtained from FWRI (http://research.myfwc.com/gallery/image_details.asp?id=24504.

colour encoding in Step 1. The colour scheme can be changed to a "rainbow" colour by selecting "Chlorophyll a" in the list of colours from Functions => Color Lut => Load Lut. The Chl-*a* image with this colour scheme may appear different to that in Figure 7.3b, but the colour stretch can be adjusted by selecting Functions => Rescale with a log stretch. A colour legend can be added by selecting Functions => Color Bar => On, and a high-resolution coastline can also be added using methods in Step 1. The final image can be saved as a colour-coded png image, similar to Step 1.

Step 3: The same steps as in Step 2 are used to load the "flh" data product from the HDF file, display it in a separate window, adjust the colour stretch, and save it as a colour-coded png image. Note that to show details at low values, a logarithmic colour stretch is required under Functions => Rescale.

Step 4: The SeaDAS software allows a user to define a new parameter using existing parameters. Based on the "chlor_a" data available in the "Band List Selection" window, Equation 7.1 is used to estimate $b_{bp,Morel}$. Assuming "chlor_a" is the 5^{th} band in the band list, type in the following commands under Utilities => Data Manipulation => User Defined Operations:

```
bad_idx=where(B5 lt 0.001)
B5[bad_idx]=0.001
result=0.3*B5^0.62*(0.002 + 0.02 * (0.5 - 0.25 * alog10(B5)))
```

Then, type in "bbp_morel" in the "New band name" field, and click "Run." This will create a new parameter "bbp_morel" in the "Band List Selection" window (assuming it is the 6^{th} band in the window). Load bbp_551_qaa from the HDF file to this window (assuming it is the 7^{th} band in the window). In the "User Defined Operations" window type in the following commands:

```
result=B7/B6
low_chl_idx = where(B5 lt 1.5)
result[low_chl_idx]=0.0
```

Then, type in "bbp_ratio" in the "New band name" field, and click "Run." This will create a new parameter "bbp_ratio" in the "Band List Selection" window. This band can be displayed, colour stretched, and saved as a colour-coded png image (together with a colour legend) using the same steps as above. The saved image should appear as the opposite of Figure 7.3d with the cold colours representing low values and the warm colours representing high values.

7.5 Questions

Q1: What do the various colour shades in Figure 7.3a mean? Do the dark shades between Tampa Bay and Charlotte Harbor indicate high Chl-*a*?

Q2: Do the high Chl-*a* values (yellowish and reddish colours indicated on the colour legend) in Figure 7.3b represent high chlorophyll-*a* concentrations or something else?

Q3: What do the high FLH values in Figure 7.3c mean?

Q4: Do the low "bbp_ratio" values in Figure 7.3d indicate *K. brevis* blooms?

7.6 Answers

A1: Similar to Figure7.1a, the various colour shades in the RGB image can be used to qualitatively distinguish various waters. Dark colours result from high concentrations of CDOM and/or chlorophyll-*a*, but it is impossible to tell which of the two is dominant because they both strongly absorb blue light. So the dark shades between Tampa Bay and Charlotte Harbor do not necessarily indicate high Chl-*a*. The bright colours in the ERGB image result from suspended sediments and/or shallow bottom because they both strongly scatter light.

A2: The warm colours in coastal waters do not necessarily indicate high Chl-*a* because the band-ratio empirical algorithm used to derive Chl-*a* could falsely interpret other water constituents (CDOM, suspended sediments, and shallow bottom) as chlorophyll-*a*.

A3: While FLH is a reliable measure of biomass (Chl-*a*) in sediment-poor waters, in sediment-rich waters high FLH values may be simply due to high turbidity and not due to high Chl-*a*. Thus, combining Figure 7.3c with Figure 7.3a where sediment-rich waters can be easily identified, we can infer that high FLH values associated with dark waters in Figure 7.3a (between Tampa Bay and Charlotte Harbor) are likely associated with high biomass, while high FLH values associated with bright waters in Figure 7.3a (in the northern and southern parts of the coastal waters) are likely associated with high concentrations of suspended sediments.

A4: The low "bbp_ratio" values in Figure 7.3d very likely indicate *K. brevis* blooms. These blooms have a lower backscattering efficiency compared with non-*K. brevis* blooms. The waters with bbp_ratio < 1 can be classified as dominated by *K. brevis* cells. Indeed, analysis of near-concurrent FWRI water sample data (Figure 7.3e) confirms this inference for coastal waters between Tampa Bay and Charlotte Harbor. However, it is unknown if waters in the northern part of Florida (associated also with low bbp_ratio but high FLH) contain high concentrations of *K. brevis*, because CDOM interference to MODIS Chl may lead to erroneously overestimated Chl and lower-than-real bbp ratio. A related case can be found in Figure 7.1d, where offshore waters north of Tampa Bay show high CDOM (Figure 7.1a) and erroneously high MODIS Chl (Figure 7.1b and c), leading to low bbp_ratio with high Chl. Cross-examination of all four types of imagery is necessary to rule out potential false positive detection.

7.7 Discussion and Summary

We demonstrated the principles of *K. brevis* bloom detection using a combination of MODIS imagery and techniques proposed by Hu et al. (2005) and Cannizzaro et al. (2008). Several other methods have been published (Stumpf et al., 2003a; Tomlinson et al., 2004; 2008; Amin et al., 2009), but our purpose here is to show the principles as opposed to providing a comprehensive review on the various techniques.

The three cases shown here are successful examples. However, we must recognize that nature is more complex than shown here, and none of the published techniques is perfect. Indeed, our methods can result in both false-positives (i.e., identifies *K. brevis* blooms in non-bloom waters) and false negatives (i.e., identifies non-bloom in *K. brevis* bloom waters). Although the evaluation results of Tomlinson et al. (2008) show low possibilities (about 20 – 30%) for both error types if different image types are combined, such possibilities cannot be neglected.

The 70–80% success rate of the *K. brevis* bloom detection methods provides useful information in at least two aspects: 1) to document the *K. brevis* occurrence patterns in both space and time to help understand their initiation, maintenance, and control mechanisms and 2) to guide rapid response in field surveys. This capability, combined with the free availability of both MODIS data and processing software (SeaDAS), makes it particularly useful in implementing any regional satellite-based HABs monitoring system. The reader is cautioned, however, that not every HAB species contains high chlorophyll-*a* pigment or displays low backscattering efficiency. For a particular region, a regional algorithm based on the unique optical characteristics of HABs is often required.

At the time of writing, MODIS data from the Aqua satellite (afternoon pass, 2002 – present) are considered to be of science quality, but MODIS data from the Terra satellite (morning pass, 1999 – present) are provisional. The ocean colour community, especially the NASA Ocean Biology Processing Group (OBPG), is making progress by removing noise and improving calibration/retrieval algorithms for MODIS-Terra. The combined MODIS instruments will significantly increase the spatial/temporal coverage in many coastal regions, thus providing additional values in HABs monitoring. Likewise, when MERIS data (Medium Resolution Imaging Spectrometer, 2002 – present) at 300-m resolution are used, the capability to detect small-patch blooms should be enhanced. In the absence of fluorescence data (e.g., SeaWiFS is not equipped with the fluorescence bands), other techniques (e.g., Chl-anomaly or spectral curvature, see Tomlinson et al., 2008) can also be used.

In summary, ocean-colour satellite imagery is particularly useful in detecting and monitoring HAB events because of their synoptic and frequent coverage as well as the information carried in their spectral reflectance. Correct interpretation of the various image types requires sufficient knowledge in bio-optics and phytoplankton dynamics. In any case, the full potential of satellite remote sensing of HABs can only be realized through coordinated efforts between remote sensing specialists,

environmental scientists, coastal managers, and other groups.

7.7.1 Acknowledgements

This work was supported by the U.S. NASA (NNX09AE17G and NNX09AV56G), EPA (MX964754070), and NOAA (NA06NES4400004). We thank the U.S. NASA/GSFC for providing MODIS data and thank FWRI for providing *in situ K. brevis* concentration data.

7.8 References

Amin R, Zhou J, Gilerson A, Gross B, Moshary F, Ahmed S (2009) Novel optical techniques for detecting and classifying toxic dinoflagellate *Karenia brevis* blooms using satellite imagery. Opt Express 17:9126-9144

Asai S Krzanowski JJ, Anderson WH, Martin DF, Polson JB, Lockey RF, Bukantz SC, Szentivanyi A (1982) Effects of the toxin of red tide, *Ptychodiscus brevis*, on canine tracheal smooth muscle: a possible new asthma-triggering mechanism. J Allergy Clin Immunol 69: 418- 428

Babin M, Roesler CS, Cullen J J (eds) (2008) Real-time coastal observing systems for marine ecosystem dynamics and harmful algal blooms: Theory, instrumentation and modeling. UNESCO, Paris

Brand L, Compton A (2007) Long-term increase in *Karenia brevis* abundance along the Southwest Florida Coast. Harmful Algae 6:232-252

Cannizzaro JP, Carder KL, Chen FR, Heil CA, Vargo GA (2008) A novel technique for detection of the toxic dinoflagellate, *Karenia brevis*, in the Gulf of Mexico from remotely sensed ocean color data. Cont Shelf Res 28:137-158

Carder KL, Chen FR, Lee ZP, Hawes SK, Kamykowski D (1999) Semianalytic Moderate-Resolution Imaging Spectrometer algorithms for chlorophyll *a* and absorption with bio-optical domains based on nitrate- depletion temperatures. J Geophys Res 104:5403-5421

Christman, M , Young L (2006) Analysis of *Karenia brevis* Gulf Data. Final project report to Florida Wildlife Research Institute, from University of Florida, Gainsville, FL, June 2006

Craig SE, Lohrenz SE, Lee ZP, Mahoney KL, Kirkpatrick GJ, Schofield OM, Steward RG (2006) Use of hyperspectral remote sensing reflectance for detection and assessment of the harmful alga, *Karenia brevis*. Appl Optics 45:5414-5425

Cullen JJ, Ciotti AM, Davis RF, Lewis MR (1997) Optical detection and assessment of algal blooms. Limnol Oceanogr 42:1223-1239

Dierssen HM, Kudela RM, Ryan JP, Zimmerman RC (2006) Red and black tides: Quantitative analysis of water-leaving radiance and perceived color for phytoplankton, colored dissolved organic matter, and suspended sediments. Limnol Oceanogr 51:2646-2659

Evens TJ, Kirkpatrick GJ, Millie DF, Chapman DJ, Schofield OME (2001) Photophysiological responses of the toxic red-tide dinoflagellate *Gymnodinium breve* (Dinophyceae) under natural sunlight. J Plank Res 23:1177-1193

Flewelling, LJ, Naar JP, Abbott JP, Baden DG, Barros NB, Bossart GD, et al. (2005) Brevetoxicosis: red tides and marine mammal mortalities. Nature 435: 755-756

Gilerson A, Zhou J, Hlaing S, Ioannou I, Schalles J, Gross B, Moshary F, Ahmed S (2007) Fluorescence component in the reflectance spectra from coastal waters. Dependence on water composition. Optics Express 15:15702-15721

Gordon HR, Wang M (1994) Retrieval of water-leaving radiance and aerosol optical thickness over the oceans with SeaWiFS: A preliminary algorithm. Appl Optics 33:443-452

Habas EJ , Gilbert CK (1974) The economic effects of the 1971 Florida red tide and the damage it presages for future occurrences. Environ Lett 6: 139-147

Hemmert WH (1975) The public health implications of *Gymnodinium breve* red tides, a review of the literature and recent events. In: LoCicero, VR (ed), Proceedings of the First International Conference on Toxic Dinoflagellate Blooms: 489-497

Hu CM, Muller-Karger FE, Biggs DC, Carder KL, Nababan B, Nadeau D, Vanderbloemen J (2003) Comparison of ship and satellite bio-optical measurements on the continental margin of the NE Gulf of Mexico. Int J Rem Sens 24:2597-2612

Hu CM, Muller-Karger FE, Taylor CJ, Carder KL, Kelble C, Johns E, Heil CA (2005) Red tide detection and tracing using MODIS fluorescence data: A regional example in SW Florida coastal waters. Rem Sens Environ 97:311-321

Hu C, Swarzenski PW, Muller-Karger FE (2006) Hurricanes, submarine groundwater discharge, and Florida's red tides. Geophys Res Lett 33: L11601, doi:10.1029/2005GL025449

Kirkpatrick B, Fleming LE, Squicciarini D, Backer LC, Clark R, Abraham W, Benson J, Cheng YS, Johnson D, Pierce R, Zaias J, Bossart GD, Baden DG (2004) Literature review of Florida red tide: implications for human health effects. Harmful Algae 3:99-115

Kirkpatrick GJ, Millie DF, Moline MA, Schofield O (2000) Optical discrimination of a phytoplankton species in natural mixed populations. Limnol Oceanogr 45:467-471

Landsberg JH, Steidinger KA (1998) A historical review of *Gymnodium breve* red tides implicated in mass mortalities of the manatee (*Trichechus manatus* latiriostris) in Florida, USA. In: Reguera, B, Blanco J, Fernandez ML , Wyatt T (eds), Proceedings of the 8th International Conference on Harmful Algal Blooms, Vigo, Spain: 97-100

Larkin, SL , Adams CM (2007) Harmful algal blooms and coastal business: economic consequences in Florida. Soc Nat Resour 20: 849-859

Lee Z, Carder KL, Arnone RA (2002) Deriving inherent optical properties from water color: a multiband quasi-analytical algorithm for optically deep waters. Appl Opt 41: 5755-5772

Lenes JM, Darrow BP, Cattrall C, Heil CA, Callahan M, Vargo GA, Byrne RH, Prospero JM, Bates DE, Fanning KA, Walsh JJ (2001) Iron fertilization and the *Trichodesmium* response on the West Florida shelf. Limnol Oceanogr 46:1261-1277

Letelier RM, Abbott MR (1996) An analysis of chlorophyll fluorescence algorithms for the Moderate Resolution Imaging Spectrometer (MODIS). Rem Sens Environ 58:215-223

Lohrenz SE, Fahnenstiel GL, Kirkpatrick GJ, Carroll CL, Kelly KA (1999) Microphotometric assessment of spectral absorption and its potential application for characterization of harmful algal species. J Phycol 35:1438-1446

McKee D, Cunningham A , Wright D, Hay L (2007) Potential impacts of nonalgal materials on water-leaving Sun induced chlorophyll fluorescence signals in coastal waters. Appl Opt 46:7720-7729

Millie DF, Schofield O, Kirkpatrick GJ, Johnsen G, Tester PA, Vinyard BT (1997) Phytoplankton pigments and absorption spectra as potential 'Biomarkers' for harmful algal blooms: a case study of the Florida red-tide dinoflagellate, *Gymnodinium breve*. Limnol Oceanogr 42:1240-1251

Morel A (1988) Optical modeling of the upper ocean in relation to its biogenous matter content (Case I waters). J Geophys Res 93:10,749-10,768

O'Reilly JE, Maritorena S, Siegel D, O'Brien MC, Toole, D, Mitchell BG, Kahru, M, Chavez FP, Strutton P, Cota G, Hooker SB, McClain CR, Carder KL, Muller-Karger F, Harding L, Magnuson A, Phinney D, Moore GF, Aiken J, Arrigo KR, Letelier R, Culver M (2000) Ocean color chlorophyll a algorithms for SeaWiFS, OC2 and OC4: Version 4. In: Hooker SB and Firestone ER (eds) SeaWiFS Postlaunch Calibration and Validation Analyses (Part 3), NASA Technical Memorandum 2000-206892, Volume 10, NASA GSFC, 9-23

Schofield O, Grzymski J, Bisset WP, Kirkpatrick GJ, Millie DF, Moline M, Roesler CS (1999) Optical monitoring and forecasting systems for harmful algal blooms: possibility or pipe dream? J Phycol 35:1477-1496

Steidinger, KA, Vargo GA , Tester PA, Tomas CR (1998) Bloom dynamics and physiology of Gymnodinium breve, with emphasis on the Gulf of Mexico. In: Physiological Ecology of Harmful Algal Blooms (Anderson EM , Cembella AD, Hallengraff GM, eds) Springer-Verlag, New York: 135-153

Stumpf RP, Culver ME, Tester PA, Tomlinson M, Kirkpatrick GJ, Pederson BA, Truby E, Ransibrahmanakul V, Soracco M (2003) Monitoring *Karenia brevis* blooms in the Gulf of Mexico using satellite ocean color imagery and other data. Harmful Algae 2:147-160

Stumpf RP, Arnone RA, Gould RW, Martinolich PM, Ransibrahmanakul V (2003b) A partially coupled ocean-atmosphere model for retrieval of water-leaving radiance from SeaWiFS in coastal waters.

In: S B Hooker and E R Firestone (eds) SeaWiFS postlaunch technical report series, Vol 22: Algorithm updates for the fourth SeaWiFS data processing, 51-59

Tester PA, Steidinger KA (1997) *Gymnodinium breve* red tide blooms: Initiation, transport, and consequences of surface circulation. Limnol Oceanogr 42:1039-1051

Tomlinson MC, Stumpf RP, Ransibrahmanakul V, Truby EW, Kirkpatrick GJ, Pederson BA, Vargo GA, Heil CA (2004) Evaluation of the use of SeaWiFS imagery for detecting *Karenia brevis* harmful algal blooms in the eastern Gulf of Mexico. Rem Sens Environ 91:293-303

Tomlinson MC, Wynne TT, Stumpf RP (2008) An evaluation of remote sensing techniques for enhanced detection of the toxic dinoflagellate, *Karenia brevis* . Remote Sens Environ 113:598- 609

Walsh JJ, Jolliff JK, Darrow BP, Lenes JM, Milroy SP, Remsen A, Dieterle DA, Carder KL, Chen FR, Vargo GA, Weisberg RH, Fanning KA, Muller-Karger FE, Shinn E, Steidinger KA, Heil CA, Tomas CR, Prospero JS, Lee TN, Kirkpatrick GJ, Whitledge TE, Stockwell DA, Villareal TA, Jochens AE, Bontempi PS (2006) Red tides in the Gulf of Mexico: Where, when, and why? J Geophys Res 111: 111: C11003, doi:10.1029/2004JC002813

Walsh JJ, Steidinger KA (2001) Saharan dust and Florida red tides: The cyanophyte connection. J Geophys Res 106:11597-11612

Walsh JJ, Weisberg RH, Lenes JM, Chen FR, Dieterle DA, Zheng L, Carder KL, Vargo GA, Havens JA, Peebles E, Hollander DJ, He R, Heil CA, Mahmoudi B, Landsberg JH (2009) Isotopic evidence for dead fish maintenance of Florida red tides, with implications for coastal fisheries over both source regions of the West Florida shelf and within downstream waters of the South Atlantic Bight. Prog Oceanogr 80:51-73

Zhang H (2002) Detecting Red Tides on the West Florida Shelf by Classification of SeaWiFS Satellite Imagery. Master's thesis, Department of Computer Science and Engineering, University of South Florida, December 2002

Case Study 8

Monitoring Green Tides in Chinese Marginal Seas

Ming-Xia He[1], Junpeng Liu[1], Feng Yu[1], Daqiu Li[2], Chuanmin Hu[*3]

8.1 Background

Coastal phytoplankton blooms have been reported world wide. These blooms sometimes cause environmental problems in both developed and developing countries where excessive nutrients and other pollutants from rapid-growing agriculture, aquaculture, and industries are delivered to the ocean. In Chinese coastal waters of the Yellow Sea, East China Sea, and Bohai Sea, the number and size of toxic algae blooms (often called red tides) as well as toxic species have increased significantly since 1998, a result of increased nutrient inputs from multiple sources (Zhou and Zhu, 2006).

Similar to red tides, green tides have also been reported in the world's oceans (e.g., Fletcher, 1996; Blomster et al, 2002; Nelson et al. 2003; Merceron et al., 2007). These green tides contain high concentrations of green macroalgae, but they are typically small in size and restricted to coastal areas. However, between May and July 2008, an extensive bloom of the green macroalgae *Ulva prolifera* (previously known as *Enteromorpha prolifera*, see Hayden et al., 2003) occurred in coastal and offshore waters in the Yellow Sea (YS) near Qingdao, China (Hu and He, 2008). The macroalgae bloom created an enormous burden on local government and management agencies because all the algae that washed up onto the beach and in the Olympic sailing area near Qingdao had to be physically removed (Figure 8.1). By the end of July 2008, >1,000,000 tons of algae had been removed. Other methods (e.g., using a 30-km boom) were employed to maintain an algae-free area of water near Qingdao for the Olympic sailing competition, with a total cost exceeding US$100 million (Wang et al., 2009; Hu et al., 2010). The bloom was first speculated to be a result of local pollution, but analysis of MODIS (Moderate Resolution Imaging Spectroradiometer) satellite imagery revealed a remote origin (Hu and He, 2008). More recent studies suggested that the bloom was a result of rapid expansion of the coastal seaweed aquaculture

[1]Ocean Remote Sensing Institute, Ocean University of China, 5 Yushan Road, Qingdao, China 266003
[2]Institute for Environmental Protection Science at Jinan, 183, Shanda Road, Jinan, China 250014
[3]College of Marine Science, University of South Florida, 140 7th Ave., S., St. Petersburg, FL 33701, USA. *Email address: hu@marine.usf.edu

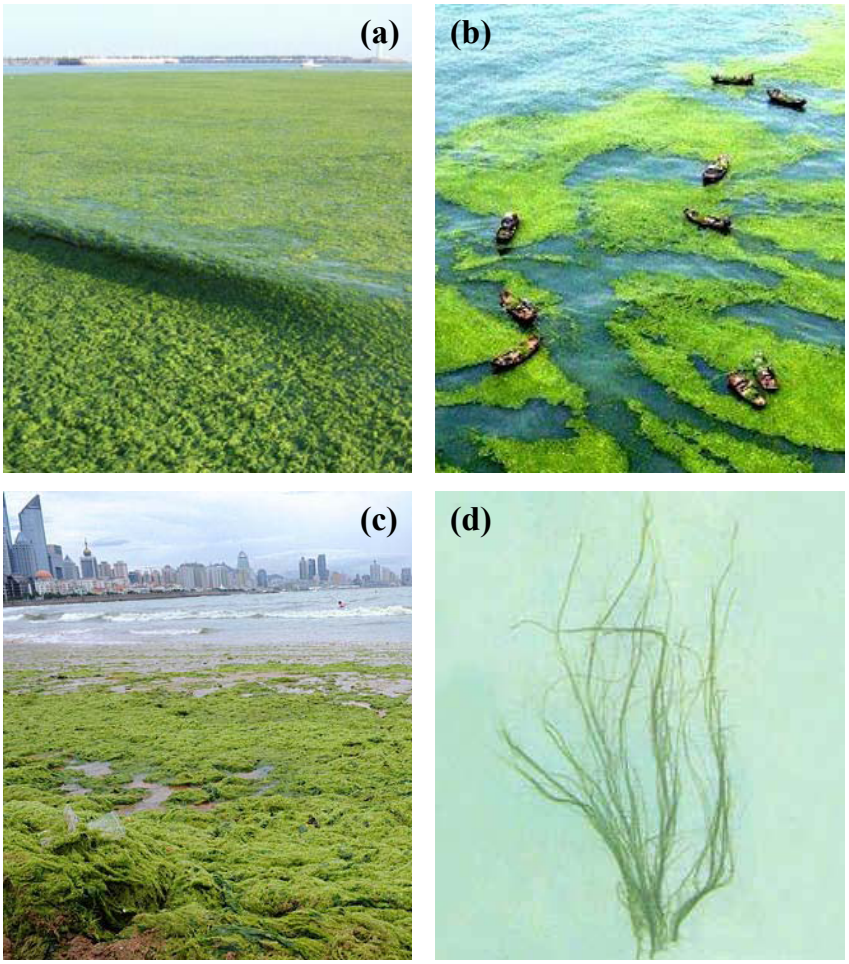

Figure 8.1 Green tide of macroalgae *Ulva prolifera* in coastal waters of the Yellow Sea near Qingdao, China. (a) and (b) Macroalgae blooms in coastal waters; (c) algae washed onto the beach; (d) morphology of the algae, which can grow to >1 m in length. (Images from public news media http://tupian.hudong.com/a2_70_76_01300000195282124057760319832_jpg.html).

of *P. yezoensis* where water circulation and favourable growth conditions brought remote *U. prolifera* to Qingdao (Li et al., 2008; Liang et al., 2008; Lu and Qiao, 2008; Qiao et al., 2008; Sun et al., 2008; Hu, 2009; Liu et al., 2009; Hu et al., 2010). Further, it was found that smaller green macroalgae blooms were recurrent in history not only in the YS but also in the East China Sea (ECS) (Hu et al., 2010). Because green tides of the same macroalgae may occur in the future in both YS and ECS, it is desirable to establish a remote-sensing based monitoring system to provide timely information on the occurrence and characteristics of green tides (location, size, and potential trajectory). Indeed, a rapid-response remote sensing system using multiple satellites has shown critical values to help implement management plans during the 2008 bloom event (Jiang et al., 2009). Here, using data from several

satellite instruments, we describe the methodology used to detect green tides, and a preliminary monitoring system that covers the entire YS and ECS (Figure 8.2). Our primary objective is to demonstrate the methods used to identify green tides from space, which may be applied in other coastal regions where similar green tides also occur.

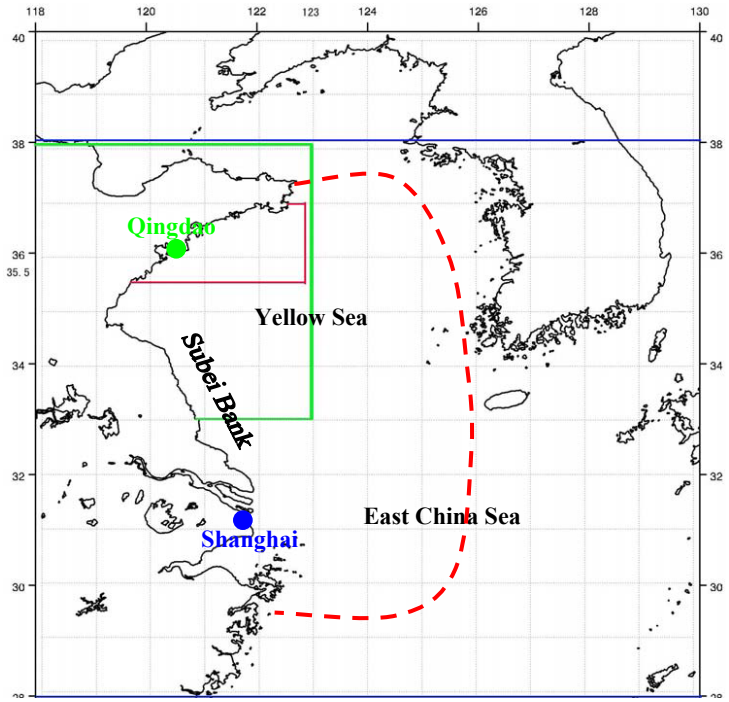

Figure 8.2 Geographic areas (dashed red line) where green tides of the macroalage *Ulva prolifera* were found between 2000 and 2009. Our monitoring efforts are focused on the Yellow Sea and East China Sea. The various colour boxes represent several pre-defined regions to facilitate image display and interpretation. An experimental online monitoring system has been established and has been in operation since early 2009: `http://www.station.orsi.ouc.edu.cn:8080/algae/`.

8.2 Data and Methods

Three types of data were used. Type 1 is near real-time data obtained from the MODIS instruments onboard the U.S. NASA satellites Terra (1999 – present) and Aqua (2002 – present), and the MERSI (Medium Resolution Spectral Imager) instrument onboard the Chinese satellite FY-3A (2008 – present). These satellite instruments have a wide swath width (>2000 km) and frequent coverage, and provide medium-resolution (250-m) data suitable for identifying large-scale macroalgae blooms. Although the individual multi-cell algae are thin and small (Figure 8.1), their aggregation makes

them appear as surface vegetation and therefore detectable in satellite imagery. Type 2 is high-resolution data from satellite instruments designed for land and coastal waters, for example Landsat, SPOT, Synthetic Aperture Radar (SAR), and HJ-1. These data have limited spatial (hundreds of kilometers) and infrequent (one week to 16 days) coverage, but can be used to detect small-scale macroalgae blooms. Type 3 is near-real time data from MODIS, MERSI, COCTS (onboard the Chinese satellite HY-1B, 2007 – present), and QuikScat (1999 – present). These data can provide environmental conditions of the study regions, including sea surface temperature (SST), sea surface wind (SSW), and ocean chlorophyll-*a* concentrations.

For brevity, in this work we demonstrate primarily how to use MODIS (Type 1 data) and Landsat (Type 2 data) to detect macroalgae blooms in open oceans and coastal waters. The use of Type 3 data to assess environmental conditions is shown in other case studies. MODIS data source and most processing methods are described in detail in another case study (*Detection of Oil Slicks using MODIS and SAR Imagery*), but for completeness they are summarized here. All data were downloaded from the U.S. NASA Goddard Space Flight Center (GSFC) at no cost (http://oceancolor.gsfc.nasa.gov). The data are open to the public in near real-time and do not require data subscription. The following steps were used to generate geo-referenced MODIS products at 250-m resolution.

Step 1: MODIS Level-0, 5-minute granules (satellite data collected every 5 minutes were stored in a computer file to facilitate data management) were downloaded from NASA/GSFC;

Step 2: MODIS Level-0 data were processed to generate Level-1b (calibrated total radiance) data for the 36 spectral bands using the SeaWiFS Data Analysis System (SeaDAS) software. The software was originally designed to process SeaWiFS data only, but was updated to process data from other satellite instruments including MODIS. The free software is distributed by the U.S. NASA GSFC. The Level-1b data were stored in computer files in Hierarchical Data Format (HDF);

Step 3: MODIS Level-1b data were used to derive the spectral reflectance:

$$R_{\mathrm{rc},\lambda}(\theta_0,\theta,\Delta\phi) = \pi L^*_{\mathrm{t},\lambda}(\theta_0,\theta,\Delta\phi)/(F_{0,\lambda}\times\cos\theta_0) - R_{\mathrm{r},\lambda}(\theta_0,\theta,\Delta\phi), \qquad (8.1)$$

where λ is the wavelength for the MODIS band, L^*_{t} is the calibrated sensor radiance after correction for gaseous absorption, F_0 is the extraterrestrial solar irradiance, $(\theta_0,\theta,\Delta\phi)$ represent the pixel-dependent solar-viewing geometry, and R_{r} is the reflectance due to Rayleigh (molecular) scattering. This step used the software CREFL from the NASA MODIS Rapid Response Team. The R_{rc} data of the 7 MODIS bands (469, 555, 645, 859, 1240, 1640, and 2130 nm) were stored in HDF computer files.

Step 4: The R_{rc} data were geo-referenced to a rectangular (also called geographic lat lon) projection for the area of interest, defined by the North-South and East-

West bounds. Because 1 degree is about 110 km at the equator, the map-projected data have 440 image pixels per degree, corresponding to 250 m per image pixel. Although only the MODIS 645- and 859-nm bands have a nadir resolution of 250 m, other bands at 500-m resolution were interpolated to 250-m resolution using a sharpening scheme similar to that for Landsat (i.e., the 250-m data at 645 nm were congregated to 500-m data, and the ratios between a congregated 500-m pixel and the 4 individual 250-m pixels were applied to "sharpen" the MODIS 500-m data from other bands). The mapping software was written in-house using C++ and PDL (Perl Data Language) with a mapping accuracy of about 0.5 image pixel;

Step 5: The map projected R_{rc} data at 645, 555, and 469 nm were converted to byte values using a logarithmic stretch, and then used as the Red, Green, and Blue channels, respectively, to compose a RGB image. The purpose was to visually identify land and clouds;

Step 6: A floating algae index (FAI) data product was derived as follows (Hu, 2009):

$$\begin{aligned} \text{FAI} &= R_{\text{rc,NIR}} - R_{\text{rc,NIR}'}, \\ R_{\text{rc,NIR}'} &= R_{\text{rc,RED}} + (R_{\text{rc,SWIR}} - R_{\text{rc,RED}}) \times (\lambda_{\text{NIR}} - \lambda_{\text{RED}})/(\lambda_{\text{SWIR}} - \lambda_{\text{RED}}), \end{aligned} \quad (8.2)$$

where $R_{\text{rc,NIR}'}$ is the baseline reflectance in the NIR band derived from a linear interpolation between the RED and shortwave IR (SWIR) bands. For MODIS, λ_{RED} = 645 nm, λ_{NIR} = 859 nm, λ_{SWIR} = 1240 nm. FAI was designed to quantify the reflectance in the near-IR due to the vegetation "red-edge" effect, because green macroalgae floating on the water surface appear as surface vegetation.

Step 7: The RGB and FAI images were loaded in the software ENVI for display and analysis. The "Link Display" function connects the two image types, so a suspicious macroalgae slick/patch in the FAI image can be cross-examined with the RGB image to determine if it might be caused by small clouds instead of macroalgae.

Landsat-5 TM and Landsat-7 ETM+ Level-1b data were obtained from the U.S. Geological Survey at no cost (`http://glovis.usgs.gov`). These are radiometrically calibrated radiance data in seven spectral channels, geo-referenced to a UTM projection and stored in Geo-TiFF computer files. The same steps used for MODIS were used to generate Landsat RGB and FAI images using computer codes developed in-house, except that Landsat wavebands of λ_{RED} = 660 nm, λ_{NIR} = 825 nm, and λ_{SWIR} = 1650 nm were used in Equation 8.2 to derive a Landsat FAI.

8.3 Demonstration

Figure 8.3 shows a MODIS 250-m resolution FAI image covering a portion of the YS, where land and clouds are masked by the RGB image, obtained on 29 June 2008. Two extensive bloom areas are outlined in the dashed circles. These are blooms of the

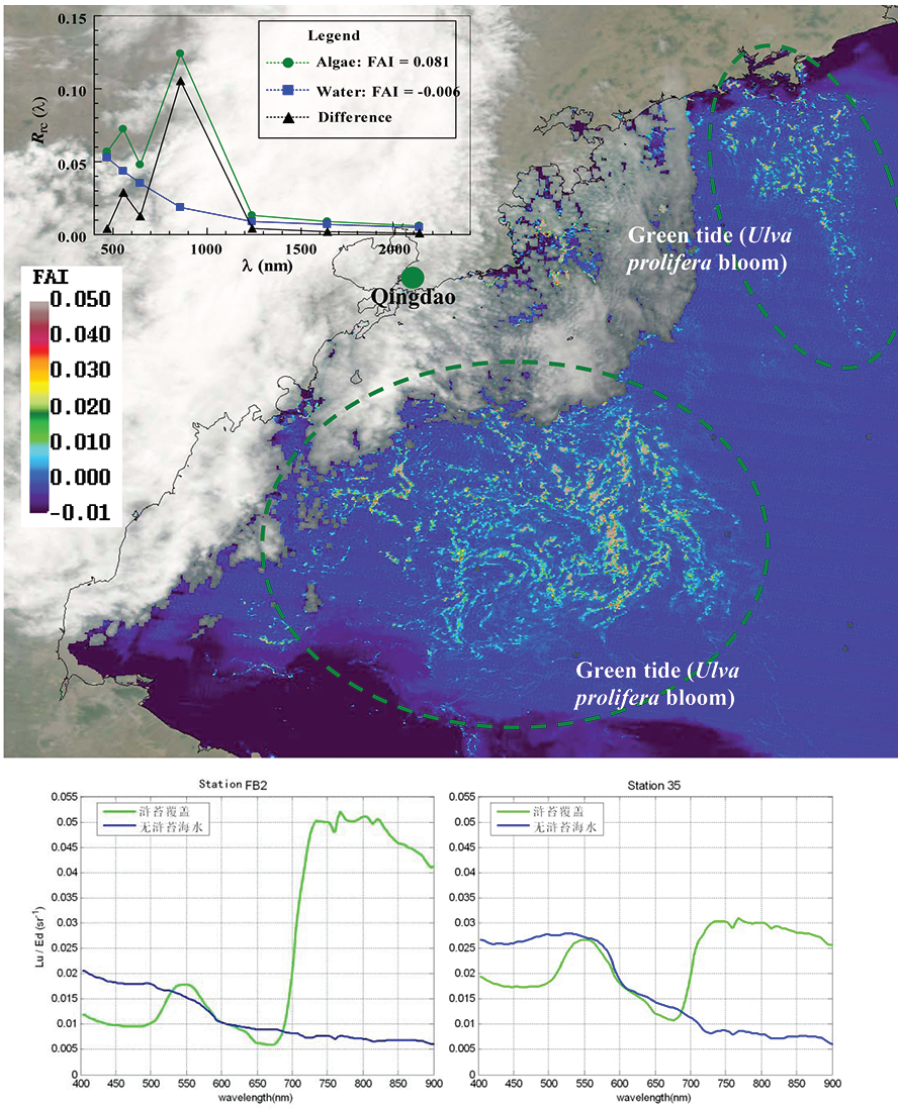

Figure 8.3 Top: MODIS floating algae index (FAI) image on 29 June 2008 showing green tides (*Ulva prolifera* blooms) in the Yellow Sea near Qingdao, China. The image covers the area of 34.5°N – 37°N and 119°E – 122°E. Cloud and land masks are overlaid on the image. The reflectance spectra of an identified algae pixel and a water pixel are shown in the inset figure. Bottom: Reflectance spectra measured from macroalgae mats (green lines) and algae-free water (blue lines) in the same region, from two different stations.

green macroalgae, *U. prolifera*, as confirmed by concurrent management activities (>1000 vessels were utilized to clean the algae in this region between late June and early August 2008, with >1,000,000 tons of algae collected). Examination of the $R_{rc,\lambda}$ spectral shapes of individual pixels from the slicks/patches show enhanced reflectance in the NIR, typical for surface vegetation. An example is shown in the

inset figure of Figure 8.3, where the spectral shape from the algae pixel is very similar to those obtained from *in situ* measurements from *U. prolifera* surface mats in the same region (Figure 8.3 bottom panels). Even though the *in situ* reflectance is defined differently (i.e., with units of sr^{-1}) and MODIS $R_{rc,\lambda}$ is not corrected for aerosol scattering effects, they both show elevated reflectance in the NIR and in the green (555 nm).

Not every MODIS 250-m pixel is covered completely by the algae. Rather, the pixels may be mixed with algae and water. The linear design of FAI (Equation 8.2) makes the unmixing straightforward. Assuming FAI ≤0.0 for 0% algae coverage in a pixel and FAI≥ 0.02 for 100% coverage in a pixel (these threshold values were determined by image gradient analysis and visual interpretation), algae coverage for FAI values between 0.0 and 0.02 can be determined using a linear interpolation. For the image shown in Figure 8.3, the total number of MODIS 250-m pixels containing the macroalgae was estimated to be 70,333, corresponding to an area of about 3600 km^2. After linear unmixing, the coverage area of algae was estimated to be 1101 km^2. The coverage area estimate, however, has some degree of uncertainty and requires field validation.

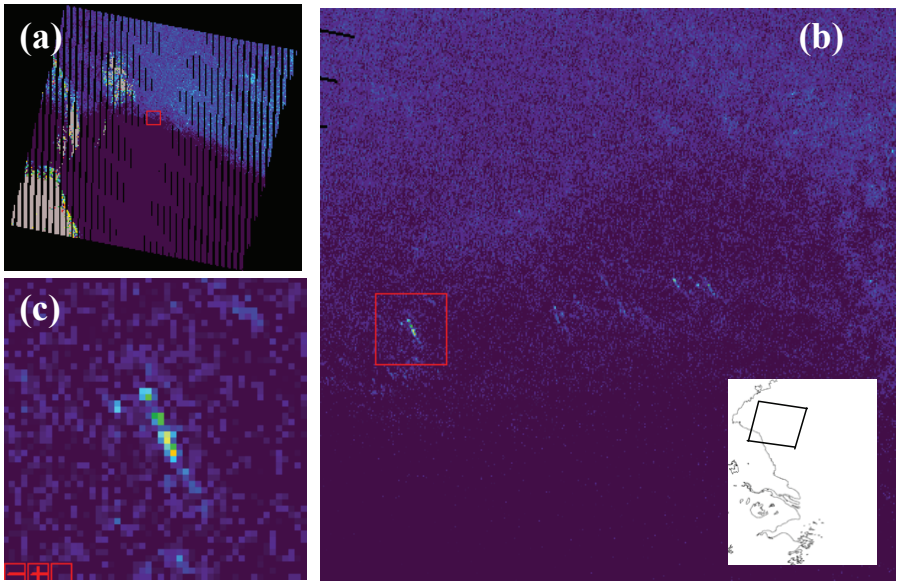

Figure 8.4 (a) Landsat-7 ETM+ FAI image on 10 May 2008 covering the northern portion of Subei Bank, where the purple colour indicates high sediment concentrations. (b) A sub-scene of 512 x 512 pixels as outlined by the red box in (a). Inset figure shows the location of the Landsat image. (c) An enlarged portion of (b) showing the algae slick.

For the MODIS instrument sensitivity, we determined that the smallest size of the algae slick that MODIS FAI imagery could reveal was about 5 m, if the slick was at least 3 – 4 pixels in length (Hu et al., 2010). Smaller algae, especially during bloom initiation, could not be detected by MODIS, but could be detected by higher-

resolution instruments such as Landsat TM and ETM+. Figure 8.4 shows a sub-scene of a Landsat ETM+ FAI image collected on 10 May 2008 in the north of the Subei Bank. The small slicks of algae are impossible to find in the corresponding MODIS FAI image, but the spectral shapes show elevated reflectance in the NIR, indicating macroalgae blooms. Indeed, Landsat and MODIS were combined to reveal the temporal evolution of the 2008 bloom event, with the conclusion that the bloom started in near-shore waters of the shallow Subei Bank (Hu et al., 2010) where aquaculture of the seaweed *P. yezoensis* was practiced every year.

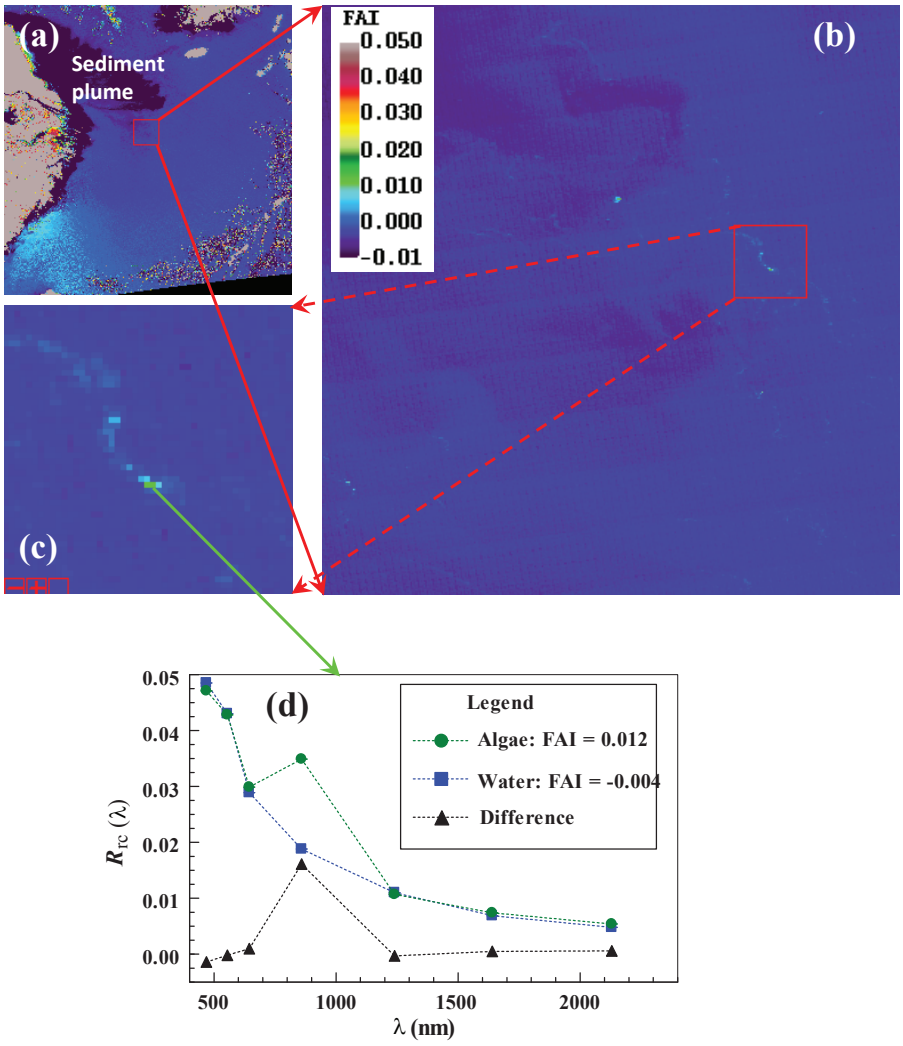

Figure 8.5 (a) MODIS-Aqua 250-m resolution FAI image on 28 April 2009 covering the ECS. (b) A sub-scene of about 100 x 100 km east of the Changjiang River mouth. (c) An enlarged portion of (b) showing the algae slick. (d) The reflectance spectra of the identified algae pixel and nearby water pixel.

The retrospective analysis of satellite imagery showed the origin, size, distribu-

tion, and evolution of the 2008 bloom event as well as smaller blooms in previous years (Hu et al., 2010). For the purpose of monitoring, MODIS data were obtained and analyzed in near real-time since early 2009 to monitor the bloom conditions in both YS and ECS (Figure 8.2). The earliest MODIS FAI image where algae slicks can be identified, obtained on 28 April 2009 from the Aqua satellite, is shown in Figure 8.5. The MODIS image shows some slicks about 200 km east of the Changjiang River mouth in the downstream of a NW – SE sediment plume from the Subei Bank, indicating that the algae slicks originated from nearshore waters of the Subei Bank. This is the same place where the 2008 macroalgae bloom originated. Spectral shapes of the algae pixels show elevated reflectance in the NIR (Figure 8.5d), suggesting that this is some kind of floating vegetation. Considering the proximity to the coast and the same origin as for the 2008 bloom, it is very likely that the algae is the same type, i.e., *U. prolifera* from expanded seaweed aquaculture. Note that this analysis is based on MOIDS data alone. Information derived from circulation models and environmental conditions (e.g., wind) provides additional evidence that these algae slicks can be *U. prolifera* (Hu et al., 2010).

8.4 Training

MODIS reflectance data collected on 19 May 2009 and 14 June 2000, and their corresponding RGB and FAI images for the ECS can be downloaded from the IOCCG website (`http://www.ioccg.org/handbook/He/`) for the demonstration on how to identify algae slicks and other features. Because of the synoptic coverage (often >10 degrees in both N–S and E–W directions) and medium resolution (250-m per pixel), the MODIS images are very large. Thus, commercial software packages (e.g., ENVI, ArcInfo, Erdas Imagine, or any other software that has basic image processing capabilities) are required to focus on a particular region. Here we use the software ENVI to demonstrate how to identify the algae slicks using the following visualization and analysis.

First, the RGB image is loaded into ENVI by using the "File -> Open Image File" function. Three display windows are shown (similar to Figures 8.6 a–c): scroll, image, and zoom. The scroll window shows the entire region at reduced resolution to serve as a browse image; the image window shows a portion of the image at full resolution (250-m); and the zoom image enlarges a smaller portion by 4 times. During the initial display in ENVI, the colours are stretched using histogram balancing over the entire image. The image window can be colour enhanced by a "Gaussian" or linear enhancement, using the menu of "Image -> Enhance".

Next, the FAI image is loaded into ENVI in the same way. The "Link Display" function is used to link the two images so that they can be cross examined. This way, any suspicious features identified on the FAI image can be easily determined if they are from clouds or land.

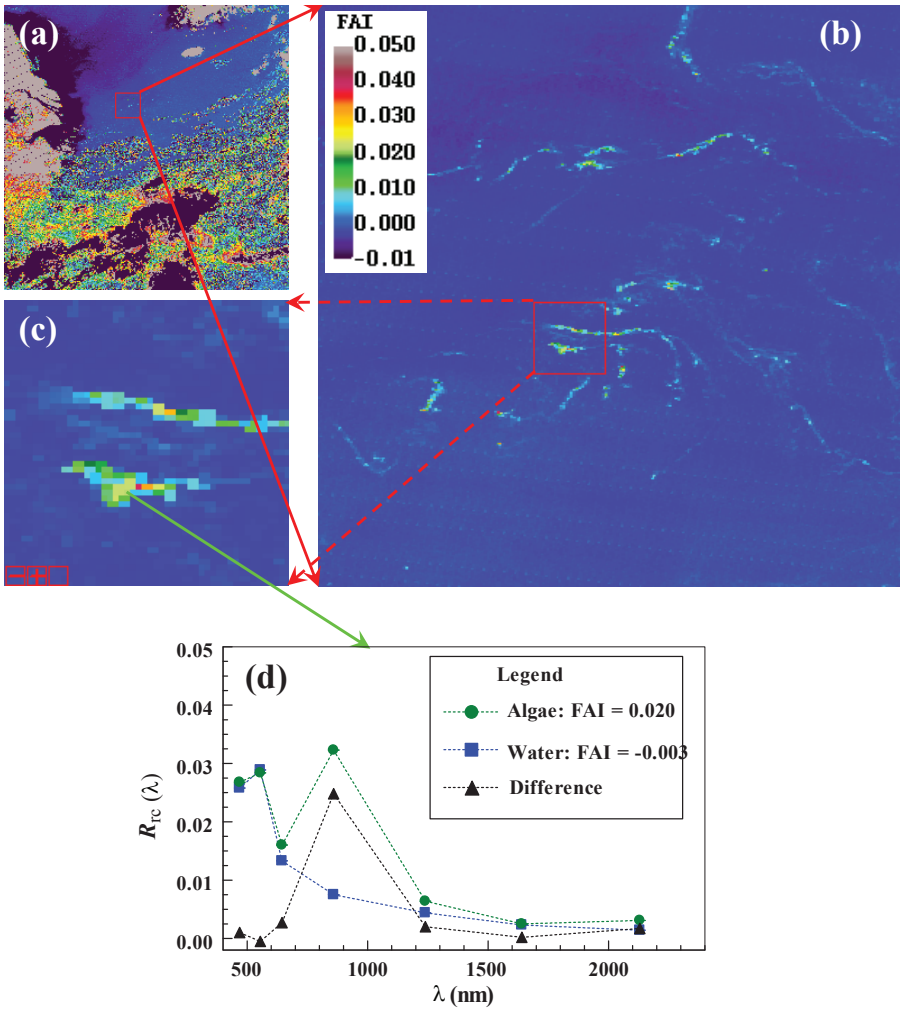

Figure 8.6 (a) MODIS-Terra 250-m FAI image on 19 May 2009 covering the ECS. (b) A sub-scene of about 100 x 100 km east of the Changjiang River mouth is shown at 250-m resolution. (c) An enlarged portion of (b) showing the algae slick. (d) The reflectance spectra of the identified algae pixel and nearby water pixel.

Finally, the image window in the scroll image is moved to examine the entire image step by step. It is easy to find that clouds and land show high FAI values. In cloud-free waters, there are also some slicks associated with high FAI values, as shown in Figure 8.6b. The same steps are applied to display the MODIS FAI image from 14 June 2000 (Figure 8.7).

8.5 Questions

Q1: Are the high-FAI slicks in Figure 8.6b the green macroalgae *Ulva prolifera*?

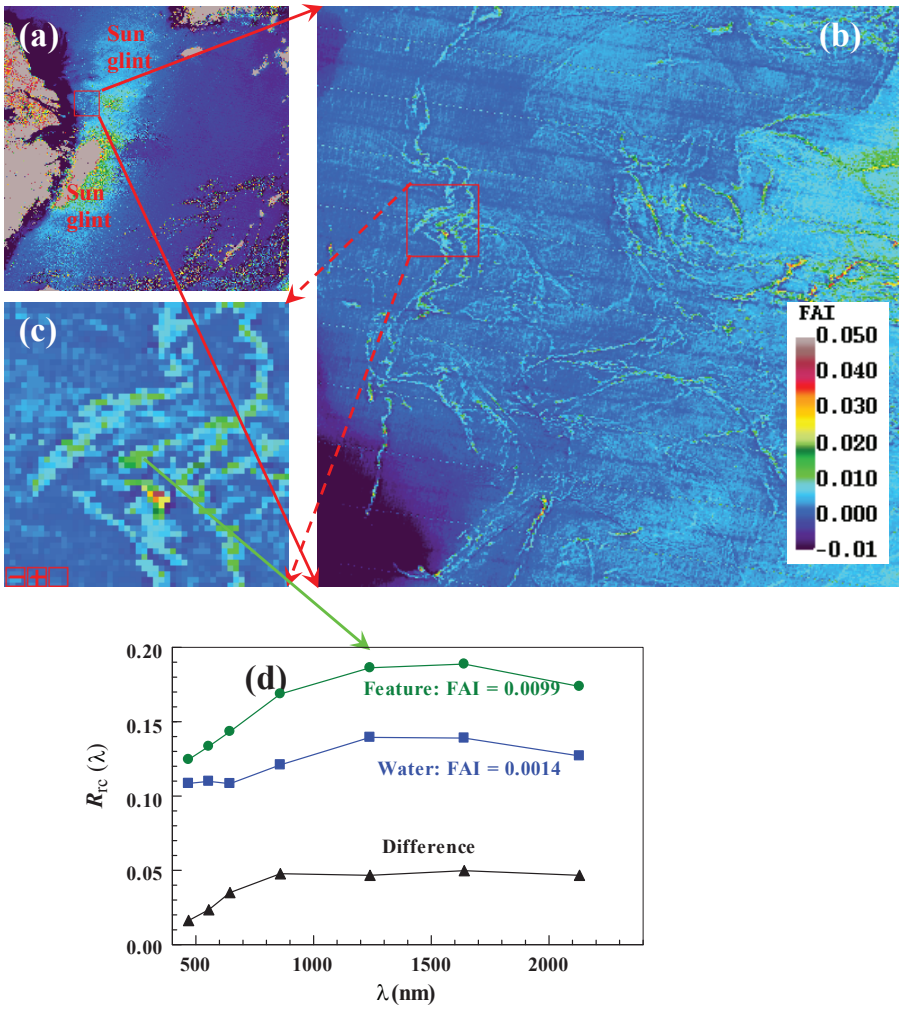

Figure 8.7 (a) MODIS-Terra 250-m FAI image on 14 June 2000 covering the ECS. (b) A sub-scene of about 100 x 100 km east of the Changjiang River mouth is shown at 250-m resolution. (c) An enlarged portion of (b) showing some suspicious slicks. (d) The reflectance spectra of the suspicious feature and a nearby water pixel. Their difference spectrum is also shown.

Q2: Are the high-FAI slicks in Figure 8.7b the green macroalgae *Ulva prolifera*?

8.6 Answers

A1: Very likely. Once clouds and sun glint can be ruled out as the potential cause of the slicks, it is almost certain that they are some sort of surface vegetation. However, to add more confidence, reflectance spectra of the identified slicks and the nearby water can be examined. Similar to the case for Figure 8.5, $R_{rc,\lambda}$ spectra extracted from pixels of the suspicious slicks show elevated reflectance in the NIR, where an

example is presented in Figure 8.6d. The data are extracted from the HDF data file for the locations (in image pixel line coordinates) of the slicks and nearby waters. The data extraction can be achieved through ENVI or simple computer programs. Although the high NIR reflectance is only an indication of surface vegetation and not necessarily the green macroalgae *Ulva prolifera*, the same arguments applied to Figure 8.5 can be used here to infer the algae type. In particular, the location is almost the same as three weeks ago (Figure 8.5) but the size is much larger, suggesting algae growth in this offshore region.

A2: Although the slicks appear to be floating algae, it is difficult to determine from the FAI image alone whether the suspicious features are freshwater slicks or whetehr they are due to water convergence, because the region is contaminated by significant sun glint (the extensive NE – SW high FAI band in Figure 8.7a). $R_{rc,\lambda}$ spectra extracted from pixels of the suspicious features show elevated reflectance in all wavelengths (Figure 8.7d), and their difference from the nearby water spectra do not show distinctive peaks at 859 nm, but rather show flat spectra from 859 to 2130 nm. Therefore, it is unlikely that these high-FAI slicks are floating algae. Indeed, cloud-free and glint-free images from adjacent days do not show similar slicks in the same region, confirming this speculation. However, the origin of the slicks, whether from freshwater or from water convergence, is still unclear.

8.7 Discussion and Summary

Visualization of suspicious slicks in MODIS 250-m imagery and Landsat 30-m imagery is relatively easy. Indeed, an interactive colour stretch applied in ENVI to the single 859-nm band, as referenced against the corresponding RGB image (to detect clouds), can also reveal the same algae slicks. However, this is labour intensive due to the interactive colour stretch. First, it is difficult to establish a consistent time-series because the single band still contains variable aerosol contributions. Likewise, a simple Normalized Difference Vegetation Index (NDVI) based on the $R_{rc,\lambda}$ data although partially removes the influence of aerosols and varying solar/viewing geometry, the residual uncertainties due to these spatially and temporarily varying properties can lead to highly variable NDVI values for the same targets. In contrast, the baseline subtraction method used in FAI serves as a simple but effective atmospheric correction, where FAI values from the same algae and water pixels remain relatively stable under varying conditions (Hu, 2009). The linear design also makes unmixing of mixed algae-water pixels straightforward. Thus, FAI is preferred to detect and quantify macroalgae blooms.

In this exercise, one must be cautious of the interpretation of suspicious slicks identified visually, especially in sun glint regions. Analysis of the spectral shape of the suspicious features and visual examination of images collected from adjacent days can add more confidence. The most difficult scenario is cloud masking. Clouds

are visually determined through examining RGB images. The reason for this is that although several cloud masking algorithms have been proposed and used to process MODIS data, in the YS and ECS where aerosols can sometimes lead to $R_{rc,NIR}$ and $R_{rc,SWIR}$ significantly higher than the pre-defined threshold reflectance for clouds, the cloud masks may reduce data coverage. Relaxing such threshold values, on the other hand, may lead to cloud pixels undetected. Developing a reliable cloud-detection algorithm specifically for this region should be the next step in this effort.

Synthetic Aperture Radar (SAR) can penetrate clouds. Limited SAR data suggest that green tide macroalgae blooms appear as bright slicks in C-band images but dark slicks in L-band images. SAR data therefore serve as an additional data source for green tide monitoring, although they have less spatial/temporal coverage and are not free. Likewise, data from other medium-resolution instruments (e.g., MERSI is equipped with similar 250-m bands as MODIS) and high-resolution instruments (e.g., HJ-1 is equipped with similar 30-m bands as Landsat TM and ETM+) can also provide complementary information to enhance our capability in green tide monitoring.

This work is focused on the green tide detection method. Understanding of the green tide characteristics (occurrence frequency, initiation, evolution, physiology, ecology, etc.), on the other hand, requires coordinated inter-disciplinary efforts in studying phytoplankton ecology, ocean circulation, and environmental forcing for algae growth (nutrient availability, temperature, etc.). These are beyond the scope of the current demonstration, but can be found in the refereed literature (e.g., Taylor et al., 2001; Merceron et al., 2007; Yuan et al., 2008). Our monitoring efforts, however, do include routine generation and analysis of ocean SST, wind, and chlorophyll-*a* concentrations. These properties provide ancillary information to understand the environmental conditions of the observed macroalgae blooms in the YS and ECS.

In summary, data from a suite of satellite instruments, from the medium-resolution MODIS and MERSI to the high-resolution Landsat and HJ as well as the cloud-free SAR, are effective in detecting blooms of the green macroalgae *Ulva prolifera* (green tides) in the YS and ECS under various conditions. Combined with other ancillary information, these data form the basis to establish a semi-operational monitoring system, currently being developed and operated jointly at the Ocean Remote Sensing Institute of the Ocean University of China (http://www.station.orsi.ouc.edu.cn:8080/algae/) and the Optical Oceanography Lab of the University of South Florida. This case study presents an example of how satellite imagery can be used to help understand and manage our coastal environments. Similar systems may be established for other coastal regions where green tides also occur.

8.7.1 Acknowledgements

This work was supported by the U.S. NASA (NNX09AE17G) and NOAA (NA06NES4400004), by a special project of the Qingdao government (NO.09-2-5-4-HY), and by the EU

FP6 DRAGONESS Project (No. SSA5.CT.2006- 030902) and the ESA-MOST Dragon Programme Ocean Project (ID2566). We thank the US NASA/GSFC and USGS for providing MODIS and Landsat data.

8.8 References

Blomster J, Back S, Fewer DP, Kiirikki M, Lehvo A, Maggs CA, Stanhope MJ (2002) Novel morphology in *Enteromorpha* (Ulvophyceae) forming green tides. Am J Bot 89:1756-1763

Fletcher, RL (1996) The occurrence of "green tides": a review In: Schramm W, Nienhuis PH (eds) Marine benthic Vegetation: recent changes and the effects of eutrophication. Springer, Berlin, Germany, p 7-43

Hayden HS, Blomster J, Maggs CA, Silva PC, Stanhope MJ, Waaland JR (2003) Linnaeus was right all along: *Ulva* and *Enteromorpha* are not distinct genera. European J Phycol 38:277-294

Hu C, He M-X (2008) Origin and offshore extent of floating algae in Olympic sailing area. EOS AGU Trans 89(33): 302-303

Hu C (2009) A novel ocean color index to detect floating algae in the global oceans. Remote Sens Environ 113: 2118-2129

Hu C, Li D, Chen C, Ge J, Muller-Karger FE, Liu J, Yu F, He M-X (2010) On the recurrent *Ulva prolifera* blooms in the Yellow Sea and East China Sea. J Geophys Res 115: C04002, doi:10.1029/2009JC005511

Jiang X, Liu J, Zou B, Wang Q, Zeng T, Guo M, Zhu H, Zou Y, Tang J (2009) The satellite remote sensing system used in emergency response monitoring for *Entermorpha prolifera* disaster and its application. Acta Oceanol Sin 31: 52-64

Li D, He S, Yang Q, Lin J, Yu F, He M-X, Hu C (2008) Origin and distribution characteristics of *Enteromorpha prolifera* in sea waters off Qingdao, China. Environ Protection 402(8B): 45-46 (in Chinese)

Liang Z, Lin X, Ma M, Zhang J, Yan X, Liu T (2008) A preliminary study of the *Enteromorpha prolifera* drift gathering causing the green tide phenomenon. Periodical of Ocean University of China 38(4): 601-604 (in Chinese, with English abstract)

Liu D, Keesing JK, Xing Q, Shi P (2009) World's largest macroalgal bloom caused by expansion of seaweed aquaculture in China. Mar Sci Bulletin doi:101016/jmarpolbul200901013

Lü X, Qiao F (2008) Distribution of sunken macroalgae against the background of tidal circulation in the coastal waters of Qingdao, China, in summer 2008. Geophys Res Lett 35: L23614, doi:101029/2008GL036084

Merceron M, Antoine V, Auby I, Morand P (2007) *In situ* growth potential of the subtidal part of green tide forming *Ulva* spp. stocks. Sci Tot Environ 384: 293-305

Nelson TA, Nelson AV, Tjoelker M (2003) Seasonal and spatial patterns of "Green tides" (Ulvoid algal blooms) and related water quality parameters in the coastal waters of Washington state, USA. Botanica Marina 46: 263-275

Qiao F, Ma D, Zhu M, Li MR, Zang J, Yu H (2008) Characteristics and scientific response of the 2008 *Enteromorpha prolifera* bloom in the Yellow Sea. Adv Mar Sci 26(3): 409-410 (in Chinese)

Sun S, Wang F, Li C, Qin S, Zhou M, Ding L et al (2008) Emerging challenges: Massive green algae blooms in the Yellow Sea. Nature Precedings, hdl:10101/npre200822661

Taylor R, Fletcher RL, Raven JA (2001) Preliminary studies on the growth of selected green-tide algae in laboratory culture: effects of irradiance, temperature, salinity and nutrients on growth rate. Botanica Marina 44: 327-336

Wang J, Yan B, Lin A, Hu J, Shen S (2007) Ecological factor research on the growth and induction of spores release in *Enteromorpha Prolifera* (Chlorophyta). Mar Sci Bull 26 (2): 60-65

Yuan D, Zhu J, Li C, Hu D (2008) Cross-shelf circulation in the Yellow and East China Seas indicated by MODIS satellite observations. J Marine Sys 70:134-149

Zhou, MJ, Zhu MY (2006) Progress of the Project "Ecology and Oceanography of Harmful Algal Blooms in China". Adv Earth Sci 21: 673-679

Case Study 9

Detecting Phytoplankton Community Structure from Ocean Colour

R.J.W. Brewin[*1], **N.J. Hardman-Mountford**[2], **T. Hirata**[3]

9.1 Background

Phytoplankton play a fundamental role in the biogeochemical cycling of the planet, with different phytoplankton communities having specific biogeochemical roles (Le Quéré et al. 2005; Nair et al. 2008). Phytoplankton support marine ecosystems as the primary carbon source for zooplankton, fish and ultimately higher predators. Furthermore, zooplankton and fish can have selective feeding preferences for phytoplankton of different sizes and types (Hansen et al. 1994; Scharf et al. 2000; Jennings et al. 2002). By improving our understanding of the spatial structure of the different phytoplankton communities, advances in biogeochemical and food-web models can be made, which may enhance our comprehension of the Earth system needed to predict future change.

Methods that can identify and quantify different elements of the phytoplankton community can provide useful information to help understand biogeochemical and ecological processes. Observing the *in situ* size structure and taxonomic grouping of phytoplankton at a global scale is, however, a challenging task. Satellite observation is currently the only practical method of observing the global ocean synoptically. With increasing concern as to how climate variation is affecting marine ecosystems, there is a large expectation of satellite remote sensing to provide global observations of the taxonomic or functional groups of phytoplankton, moving beyond conventional pigment biomass (i.e. chlorophyll).

Recently, a variety of bio-optical and ecological methods have been established that use satellite data to identify and differentiate between phytoplankton functional types (PFTs) or phytoplankton size classes (PSCs) in the surface ocean. These can be summarised into four main types: spectral-response methods which are based on

[1]School of Marine Science and Engineering, University of Plymouth, UK. **Email address:* robert.brewin@plymouth.ac.uk
[2]National Centre for Earth Observation, Plymouth Marine Laboratory, UK
[3]Graduate School of Environmental Earth Science, Hokkaido University, Japan

differences in the shape of the light reflectance/absorption spectrum for different PFTs/PSCs (Sathyendranath et al. 2004; Alvain et al. 2005; Ciotti and Bricaud 2006; Alvain et al. 2008; Brewin et al. 2010a), abundance-based methods which use information on the magnitude of chlorophyll biomass or light absorption to distinguish between phytoplankton communities (Devred et al. 2006; Uitz et al. 2006; Hirata et al. 2008a; Brewin et al. 2010b), methods that retrieve the particle size distribution from satellite-derived backscattering signal and then relate the particle size to the phytoplankton community (Hirata et al. 2008b; Kostadinov et al. 2009), and ecological-based approaches which use information on environmental factors, such as temperature and wind stress to supplement the bio-optical data for investigating specific taxa (Raitsos et al. 2008). Recent intercomparison studies suggest that abundance-based approaches appear robust at detecting dominant phytoplankton size classes (Brewin et al. 2008).

9.1.1 Phytoplankton size class model

Here we present a method for determining the fractional contribution of a phytoplankton size class (pico- <2μm, nano- 2-20μm and micro-phytoplankton >20μm) to the overall chlorophyll concentration (Brewin et al. 2010b). The model is an extension of the Sathyendranath et al. (2001) approach, based on the assumption that small cells dominate at low chlorophyll concentrations and large cells at high concentrations. The model can be expressed through two simple exponential equations. In this example the subscripts 1, 2 and 3 refer to pico-, nano- and microphytoplankton, and the total chlorophyll-*a* concentration is referred to as C (mg m^{-3}). Firstly, the chlorophyll concentration of the combined pico-nanophytoplankton population ($C_{1,2}$) can be expressed as:

$$C_{1,2} = {C_{1,2}}^{m}[1 - \exp(-S_{1,2}C)], \tag{9.1}$$

where, ${C_{1,2}}^{m}$ is the asymptotic maximum value for $C_{1,2}$ and $S_{1,2}$ determines the increase in $C_{1,2}$ with increasing total chlorophyll (C). Secondly, the chlorophyll concentration of the picophytoplankton population (C_1) can be expressed as:

$$C_1 = {C_1}^{m}[1 - \exp(-S_1C)], \tag{9.2}$$

where ${C_1}^{m}$ is the asymptotic maximum value for C_1 and S_1 determines the increase in C_1 with increasing total chlorophyll-*a* (C). The chlorophyll-*a* concentration of nanophytoplankton (C_2) and microphytoplankton (C_3) can then be calculated according to:

$$C_2 = C_{1,2} - C_1, \tag{9.3}$$

$$C_3 = C - C_{1,2}. \tag{9.4}$$

The percentage of each phytoplankton size class to the total chlorophyll concentration (C) can then be calculated by dividing the size-specific chlorophyll concentrations (C_1, C_2 and C_3) by the total chlorophyll concentration (C) and multiplying by 100, such that

$$P_1 = (C_1/C) \times 100, \tag{9.5}$$

$$P_2 = (C_2/C) \times 100, \tag{9.6}$$

$$P_3 = (C_3/C) \times 100, \tag{9.7}$$

where P_1, P_2 and P_3 represent the percentages of pico-, nano- and microphytoplankton to the total chlorophyll concentration (C). Parameter values for ${C_{1,2}}^m$, ${C_1}^m$, $S_{1,2}$ and S_1 were taken from Table 1 in Brewin et al. (2010b), and set to 1.06, 0.11, 0.85 and 6.80, respectively. When using these parameters, the model performed well when applied to satellite chlorophyll data and compared with *in situ* measurements (see section 4.3 in Brewin et al. 2010b).

Figure 9.1 shows the results from applying the model of Brewin et al. (2010b) to SeaWiFS satellite data for January and July 2006. The model was applied to daily total chlorophyll (C) images from each month and then averaged to produce the two monthly composite images. The results show clearly that very small phytoplankton cells (picophytoplankton, $<2\mu$m) dominate in the low-production, subtropical gyres, medium-sized cells (nanophytoplankton, 2-20 μm) predominate in the equatorial upwelling area and in higher latitude regions depending on the boreal or austral summer. Relatively large cells (microphytoplankton, $>20\mu$m) dominate in coastal areas and during highly productive events, such as high-latitude spring/summer blooms. Furthermore, the size fractionation shows that nanophytoplankton tend to maintain a background population of between 20-50% of the standing stock in most regions, whereas pico- and microphytoplankton have larger spatial variability.

9.1.2 Equatorial Pacific

The equatorial Pacific is a unique region of our oceans. It can act as a large source of CO_2 to the atmosphere through the upwelling of CO_2-rich waters along the equator and advection of CO_2-rich waters from the South-American coast (Etcheto et al. 1999; Feely et al. 1999), and also a sink though primary production and export (Takahashi et al. 2002). It is one of only three open-ocean areas that, despite having high nitrate and phosphate concentrations, display moderately-low phytoplankton biomass (Martin 1991; Behrenfeld et al. 1996) and are referred to as exhibiting High Nutrient, Low Chlorophyll characteristics (HNLC, Thomas 1979). This enigma has been linked to either the lack of iron that limits the growth of the phytoplankton (Martin and Fitzwater 1988; Behrenfeld et al. 1996; Coale et al. 1996) or to a large amount

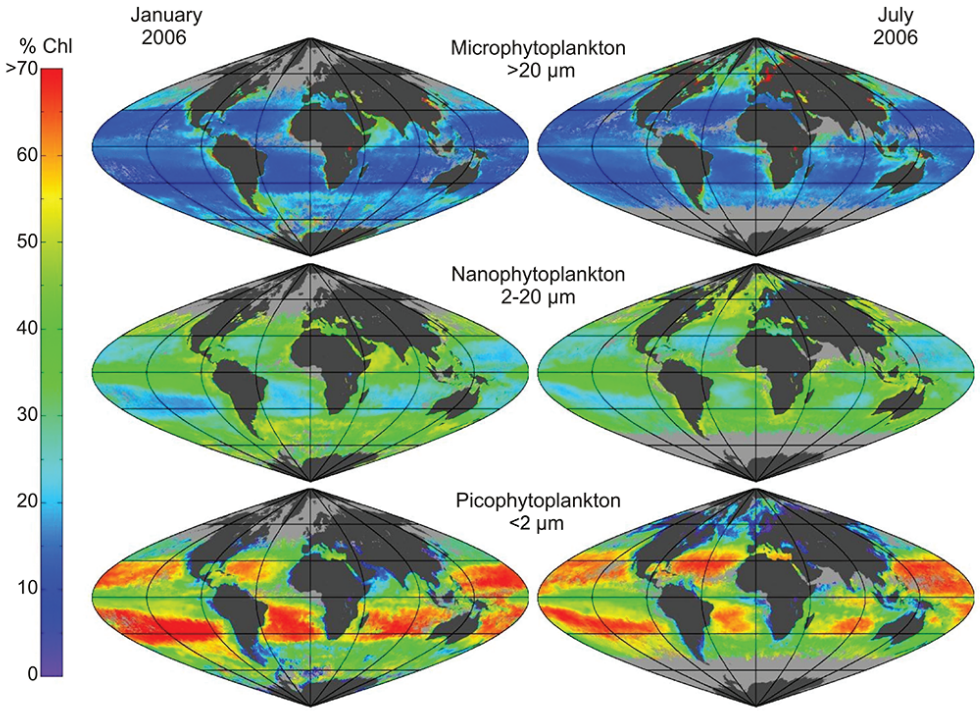

Figure 9.1 The percentage of total chlorophyll-*a* attributed to each of three phytoplankton size classes calculated according to the model of Brewin et al. (2010b), for the months of January and July 2006. The model was applied to daily Level 3 SeaWiFS composite images from each month and then averaged to produce monthly composites. Light grey pixels represent unidentified pixels due to cloud coverage or high sun zenith angles and dark grey pixels represent land.

of grazing from higher trophic levels that limits phytoplankton growth (Walsh 1976; Cullen 1991). Despite exhibiting moderately-low phytoplankton biomass, changes in the phytoplankton composition and sporadic large-scale accumulations of phytoplankton biomass have been found to occur (Chavez et al. 1990; Ryan et al. 2002), making the equatorial Pacific an ideal site to monitor variations in phytoplankton composition from satellite.

The model of Brewin et al. (2010b) was developed using an extensive dataset from the Atlantic Ocean, and validated using data with wider geographical coverage. However, the model of Brewin et al. (2010b) has not been validated in the equatorial Pacific. In light of this, 32 High Performance Liquid Chromatography (HPLC) pigment measurements (depth <10m) were downloaded from the NASA SeaBASS dataset (Werdell and Bailey 2002). Using diagnostic pigment analysis (Vidussi et al. 2001; Uitz et al. 2006; Brewin et al. 2010b) the *in situ* size-specific chlorophyll concentrations (C_1, C_2 and C_3) and size-specific percentage contributions to the total chlorophyll concentration (P_1, P_2 and P_3) were calculated for each sample. Then the

model of Brewin et al. (2010b) was applied to the *in situ* chlorophyll concentration to estimate C_1, C_2, C_3, P_1, P_2 and P_3 (Equations 9.1 – 9.7). Figure 9.2 shows the location of the 32 pigment measurements and a comparison between the diagnostic pigment-derived values and the values derived using the model. The two agreed well with an absolute root mean square error (RMSE) of 0.006 to 0.010 mg m^{-3} for the size-specific chlorophyll concentrations, and between 4.4 to 9.4 % for the percentage contributions to the total chlorophyll concentration, supporting the application of the Brewin et al. (2010b) model to the equatorial Pacific.

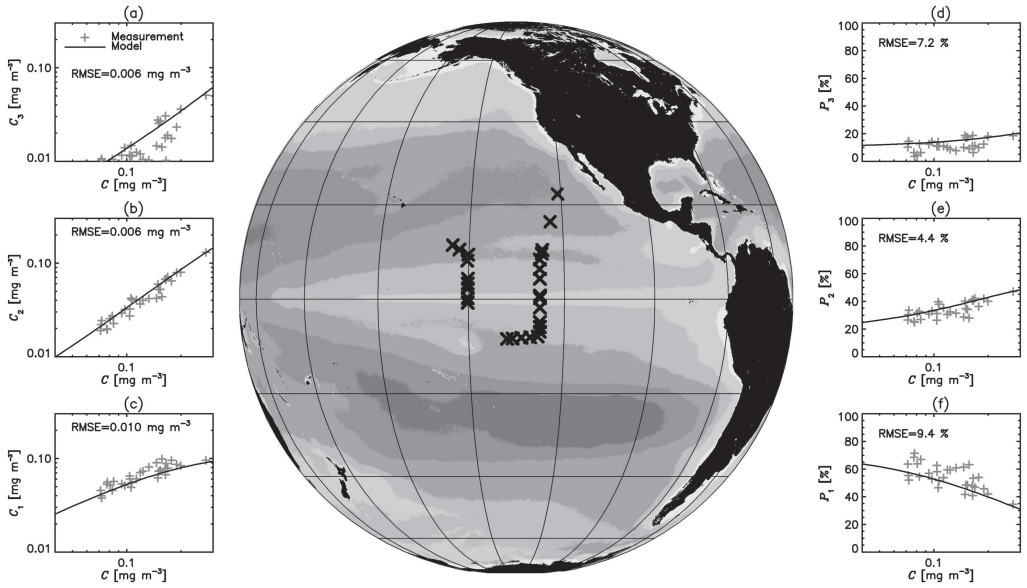

Figure 9.2 Location of the 32 HPLC pigment measurements used to validate the model of Brewin et al. (2010b) for use in the equatorial Pacific. The biome-based system of Hardman-Mountford et al. (2008) is superimposed on the globe with dark grey to light grey areas representing a transition from biomes with very low chlorophyll-*a* to biomes with very high chlorophyll-*a* . Results of the validation are shown to the left (C_1, C_2 and C_3) and right (P_1, P_2 and P_3) of the globe.

In this case study we apply the model of Brewin et al. (2010b) to daily, Level 3, SeaWiFS chlorophyll composites to produce two 8-day composites of the percentage contribution of the three size classes to total chlorophyll (P_1, P_2 and P_3), for 28 July – 4 August 1998 and 2003. We also produce two images of SST derived from the Advanced Very High Resolution Radiometer (AVHRR) sensor, for the same time periods. Differences in SST and the community composition of the three size classes, for the same seasonal week in the two contrasting years, are mapped in the equatorial Pacific.

9.2 Data and Methods

Sixteen daily Level 3 mapped SeaWiFS chlorophyll composites were downloaded from the NASA ocean colour website (http://oceancolor.gsfc.nasa.gov/), encompassing two eight-day periods.

- Week 1 (28 July – 4 August 1998)
- Week 2 (28 July – 4 August 2003)

All SeaWiFS data were extracted from the zipped format. Two SST AVHRR global composites for the same 8-day periods (week 1 and 2) were downloaded from the NASA Jet Propulsion Laboratory Physical Oceanography Distributed Active Archive Centre (ftp://podaac.jpl.nasa.gov/). Night time AVHRR Pathfinder (Version 5) 8-day means of sea surface temperature (SST) at 4 x 4 km^2 resolution were used. Night time SST products were used so that the solar radiation bias (the diurnal fluctuation in SST) that can occur from surface heating during daytime could be avoided. We used global, equal-angle, best SST. Information on the data used in this study is outlined in Table 9.1.

The software used in this study was IDL Version 6.3, Microsoft Windows (Win32 x86 m32). All IDL code developed for this study is available at http://www.ioccg.org/handbook/Brewin/. The procedure below has been developed into an IDL program (Handbook_RS_PSC_code.pro) to allow the reader to reproduce this example (see section 1.4 Training below).

The first step involves loading the sixteen daily Level 3 mapped SeaWiFS chl-*a* composites into the IDL program. All sixteen daily SeaWiFS composites are loaded into IDL using code developed by the Ocean Color Discipline Processing Group (readl3smi.pro). This code is designed to simplify the reading of SeaWiFS standard L3 mapped images, and converts the digital numbers (DN) of the image to chlorophyll-*a* values (mg m^{-3}). Once these images are loaded, the Brewin et al. (2010b) algorithm (Equations 9.1 – 9.7) is applied to each daily image on a pixel-by-pixel basis to derive P_1, P_2 and P_3 (the percentages of pico-, nano- and microphytoplankton to the total chlorophyll-*a* concentration (C)).

The daily composites from week 1 are then averaged to create 8-day composites of P_1, P_2 and P_3, and the same averaging is applied to the eight daily composites from week 2. Note that we applied the Brewin et al. (2010b) algorithm to daily images then averaged to produce an 8-day composite, as opposed to applying the algorithm directly to 8-day SeaWiFS chlorophyll-*a* composites, as the nonlinearity of equations 1 and 2 could introduce errors when applying the model directly to 8-day SeaWiFS chlorophyll-*a* composites.

The two SST images are then loaded into IDL using IDL code developed by the National Oceanographic Data Centre (pathfinder_v5_hdf_read.pro). Once these images are loaded, the data is converted to SST values (°C) from digital numbers (DN) according to:

$$\mathrm{SST} = 0.075 \times \mathrm{DN} - 3.0, \tag{9.8}$$

where the value 0.075 represents the slope and -3.0 the y-intercept. This results in six, 8-day, 9 x 9 km^2 resolution composites (arrays of [4320, 2160]) of P_1, P_2 , P_3 for both week 1 and 2, and two 8-day 4 x 4 km^2 resolution composites (arrays of [8192, 4096]) of SST for both week 1 and 2. The differences between the two contrasting weeks are then calculated according to:

$$P_{1,\mathrm{D}} = P_1(\mathrm{week1}) - P_1(\mathrm{week2}), \tag{9.9}$$

$$P_{2,\mathrm{D}} = P_2(\mathrm{week1}) - P_2(\mathrm{week2}), \tag{9.10}$$

$$P_{3,\mathrm{D}} = P_3(\mathrm{week1}) - P_3(\mathrm{week2}), \tag{9.11}$$

$$\mathrm{SST_D} = \mathrm{SST}(\mathrm{week1}) - \mathrm{SST}(\mathrm{week2}), \tag{9.12}$$

where, $P_{1,\mathrm{D}}$, $P_{2,\mathrm{D}}$, $P_{3,\mathrm{D}}$ and $\mathrm{SST_D}$ refer to the difference between the three size classes and SST of the two contrasting weeks. This results in 12 images to be used for analysis: P_1(week1), P_2(week1), P_3(week1), SST(week1), P_1(week2), P_2(week2), P_3(week2), SST(week2), $P_{1,\mathrm{D}}$, $P_{2,\mathrm{D}}$, $P_{3,\mathrm{D}}$ and SST_D. All 12 images are then rescaled to 36 x 36 km^2 resolution, to reduce computational requirements when plotting the images.

A plotting procedure is then set up to plot each of these 12 images and re-project them using an orthographic projection. The corresponding latitude and longitude values were calculated for each pixel. Values of each pixel in the image are binned into 256 ranges, and each range is assigned a colour depending on the colour scheme chosen. These 256 bins are then plotted onto an image of 1080 by 540 pixels, with each pixel representing 36 x 36 km^2 resolution. All pixels with no values (either due to cloud coverage or high sun zenith angles) are binned and assigned a light grey colour before being plotted. Using the SeaWiFS entire mission chlorophyll-*a* composite, a land mask has been developed (see "Land_mask", http://www.ioccg.org/handbook/Brewin/Data/) and the land is assigned a dark grey colour before being plotted onto the image.

Each image is then re-projected to an orthographic projection using the IDL functions "map_set.pro" and "map_proj_image.pro". Here we took the latitude of the point on the Earth's surface to be mapped to the centre of the projection plane to be 0°, and the longitude of the point on the Earth's surface to be mapped to the centre of the map projection to be -130°, to focus our attention to the equatorial Pacific. All 12 images are then projected onto the same image montage for analysis, and the respective colour bars for each image are also plotted (Figure 9.3).

Table 9.1 Satellite data used in the study (also available at http://www.ioccg.org/handbook/Brewin/Data/), including a land mask.

Date	Data	Filename	Location	Use
28/07/98	chl-a	S1998209.L3m_DAY _CHL_chlor_a_9km.bz2	http://oceancolor.gsfc.nasa.gov/cgi/l3	8-day PSC
29/07/98	chl-a	S1998210.L3m_DAY _CHL_chlor_a_9km.bz2	http://oceancolor.gsfc.nasa.gov/cgi/l3	8-day PSC
30/07/98	chl-a	S1998211.L3m_DAY _CHL_chlor_a_9km.bz2	http://oceancolor.gsfc.nasa.gov/cgi/l3	8-day PSC
31/07/98	chl-a	S1998212.L3m_DAY _CHL_chlor_a_9km.bz2	http://oceancolor.gsfc.nasa.gov/cgi/l3	8-day PSC
01/08/98	chl-a	S1998213.L3m_DAY _CHL_chlor_a_9km.bz2	http://oceancolor.gsfc.nasa.gov/cgi/l3	8-day PSC
02/08/98	chl-a	S1998214.L3m_DAY _CHL_chlor_a_9km.bz2	http://oceancolor.gsfc.nasa.gov/cgi/l3	8-day PSC
03/08/98	chl-a	S1998215.L3m_DAY _CHL_chlor_a_9km.bz2	http://oceancolor.gsfc.nasa.gov/cgi/l3	8-day PSC
04/08/98	chl-a	S1998216.L3m_DAY _CHL_chlor_a_9km.bz2	http://oceancolor.gsfc.nasa.gov/cgi/l3	8-day PSC
28/07/03	chl-a	S2003209.L3m_DAY _CHL_chlor_a_9km.bz2	http://oceancolor.gsfc.nasa.gov/cgi/l3	8-day PSC
29/07/03	chl-a	S2003210.L3m_DAY _CHL_chlor_a_9km.bz2	http://oceancolor.gsfc.nasa.gov/cgi/l3	8-day PSC
30/07/03	chl-a	S2003211.L3m_DAY _CHL_chlor_a_9km.bz2	http://oceancolor.gsfc.nasa.gov/cgi/l3	8-day PSC
31/07/03	chl-a	S2003212.L3m_DAY _CHL_chlor_a_9km.bz2	http://oceancolor.gsfc.nasa.gov/cgi/l3	8-day PSC
01/08/03	chl-a	S2003213.L3m_DAY _CHL_chlor_a_9km.bz2	http://oceancolor.gsfc.nasa.gov/cgi/l3	8-day PSC
02/08/03	chl-a	S2003214.L3m_DAY _CHL_chlor_a_9km.bz2	http://oceancolor.gsfc.nasa.gov/cgi/l3	8-day PSC
03/08/03	chl-a	S2003215.L3m_DAY _CHL_chlor_a_9km.bz2	http://oceancolor.gsfc.nasa.gov/cgi/l3	8-day PSC
04/08/03	chl-a	S2003216.L3m_DAY _CHL_chlor_a_9km.bz2	http://oceancolor.gsfc.nasa.gov/cgi/l3	8-day PSC
28/07/98 - 04/08/98	SST	1998209-1998216. s0481pfv50-bsst-16b	ftp://podaac.jpl.nasa.gov/pub/	8-day SST
28/07/03 - 04/08/03	SST	2003209-2003216. s0484pfv50-bsst	ftp://podaac.jpl.nasa.gov/pub/	8-day SST

9.3 Demonstration Section

Figure 9.3 shows a plot of the 12 images developed in the previous section where (a), (d), (g) and (j) are from week 1, (b), (e), (h) and (k) are from week 2, and (c), (f), (i), and (l) show the differences between the two weeks. The percentage of chlorophyll-*a* attributed to microphytoplankton is shown in the top three images (a-c), that attributed to nanophytoplankton in the next three (d-f), then picophytoplankton (g-i). The bottom three images represent SST (°C, j-l).

When analysing the microphytoplankton images (Figure 9.3a-c), one notices a higher proportion of microphytoplankton in the equatorial region during week 1 compared with week 2. This is highlighted in Figure 9.3c which shows the differences between the two microphytoplankton images and indicates 20% higher microphytoplankton % chlorophyll-*a* in the equatorial Pacific during week 1, with differences as high as 50% in the centre of this bloom, when compared with week 2.

When analysing the nanophytoplankton images (Figure 9.3d-f), one also notes slightly higher nanophytoplankton % chlorophyll-*a* in the equatorial region and slightly lower % chlorophyll-*a* just south-east of the equator during week 1 when compared with week 2 (Figure 9.3f). In contrast to the microphytoplankton, there is a significantly lower picophytoplankton % chlorophyll-*a* in the equatorial region during week 1 when compared with week 2 (Figure 9.3i). Furthermore, in contrast to nanophytoplankton, higher picophytoplankton % chlorophyll-*a* can be observed just south-east of the equator during week 1, compared with week 2 (Figure 9.3i).

Turning our attention to the SST images (Figure 9.3j-l), significant differences are noted between the two weeks. During week 1, lower SST values are seen in the central equatorial Pacific and slightly higher SST values in the south-east equatorial Pacific when compared with week 2.

9.4 Training

To help interpret the case study, we will now go through each of the steps to generate Figure 9.3. An IDL program (Handbook_RS_PSC_code.pro) was developed to allow the reader to reproduce this example.

1. Step 1: Download all the files needed for the case study (Table 1) from http://www.ioccg.org/handbook/Brewin/Data/ and save them to an appropriate folder on your desktop. Extract all the SeaWiFS files with the extension ".bz2" from their zipped format.

2. Step 2: Download all the IDL code needed for the case study from http://www.ioccg.org/handbook/Brewin/IDL%20Code/ and save it to your IDL path directory.

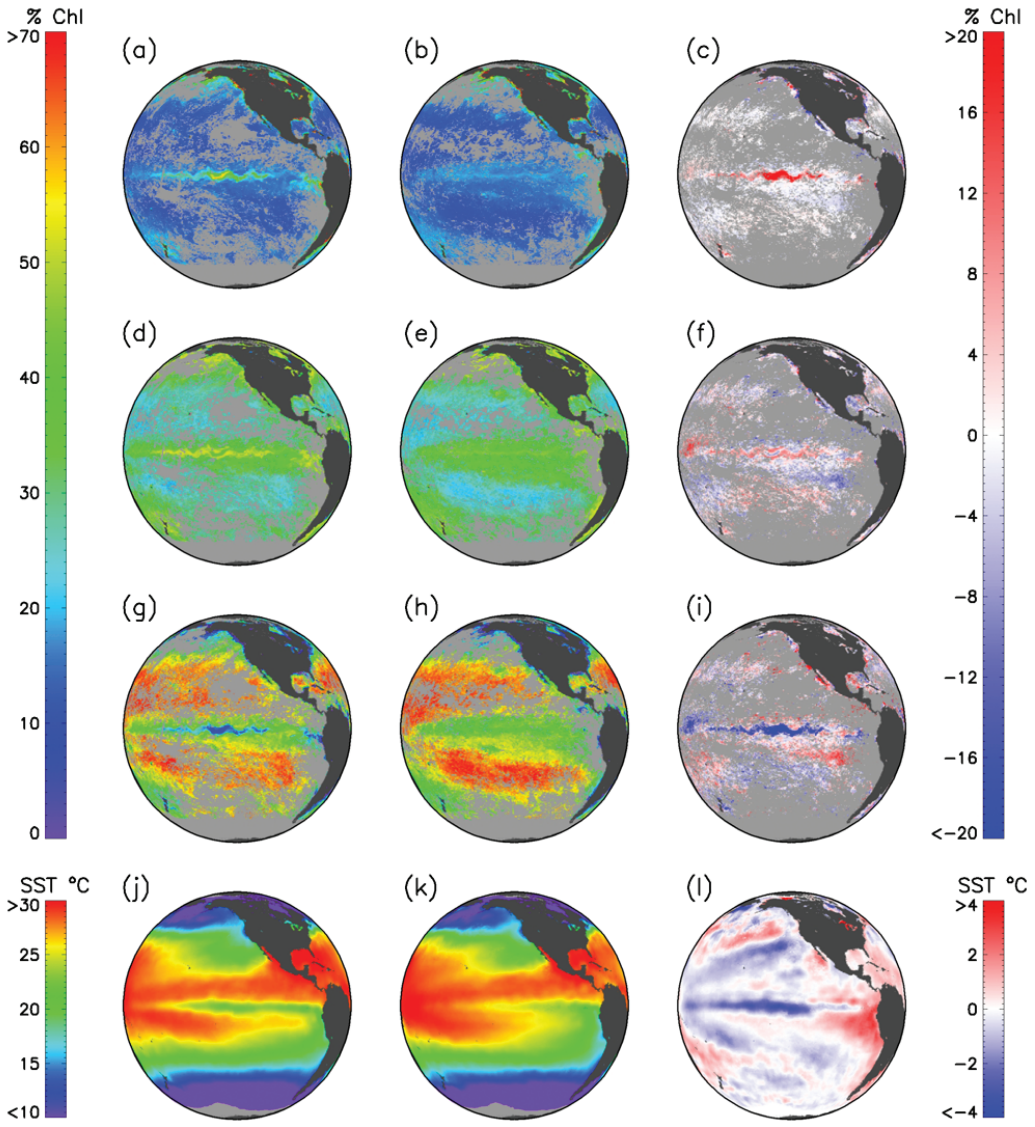

Figure 9.3 Plot of the 12 images developed in the case study. Figures (a), (d), (g) and (j) are from week 1, (b), (e), (h) and (k) from week 2, and (c), (f), (i), and (l) show the differences between the two weeks. Microphytoplankton % chlorophyll-*a* is shown in the top three images (a-c), followed by nanophytoplankton (d-f), then picophytoplankton (g-i), and at the bottom are the three SST images (j-l) in °C.

4. Step 4: The code will then run through the methodology described in section 9.2 (Data and Methods) and save Figure 9.3 to the directory where the files were downloaded in step 1.

5. NOTE: This program was run on Windows, using an Intel(R) Core(TM) 2 CPU 6320 @ 1.86GHz with 1.97GB of RAM. Using this computer, the code takes about 8 minutes to run. The code may take longer/shorter to run on other machines, may need to be manipulated for a UNIX/LINUX environment, and may need to be manipulated for other version of IDL (currently developed for IDL Version 6.3).

9.5 Questions

Q1: What phenomena may be causing the high microplankton % chlorophyll-*a* (Figure 9.3a) and the low SST values (Figure 9.3j) in the central equatorial Pacific during week 1?

Q2: Considering that the two 8-day composites are taken at the same seasonal time period, why are there such large differences in both SST and the phytoplankton community composition in Figure 9.3c, f, i and l?

Q3: How do the higher SST values south-east of the equatorial Pacific in week 1 (Figure 9.3j and l) appear to be influencing the phytoplankton community composition?

9.6 Answers

A1: The phenomena causing the high microplankton % chlorophyll-a (Figure 9.3a) and the low SST values (Figure 9.3j) in week 1, in the central equatorial Pacific, is the 1997-1999 El Niño/La Niña event. The periodic occurrence of El Niño and La Niña episodes has a strong effect on the physical forcing in the equatorial Pacific. Under non-El Niño conditions, easterly trade winds create a channel of cold surface water along the equator, referred to as the Eastern Equatorial Undercurrent (EUC). The EUC flows eastward across the equator at a depth of 20 to 200 m (Toggweiler and Carson 1995). During an El Niño event, a weakening or reversal of the trade winds occurs, which weakens the EUC and hence subdues the upwelling of cold nutrient rich waters and deepens the thermocline. Surface waters become warmer and nutrient poor. During a La Niña event, there is a strengthening of the trade winds, which strengthens the EUC, enhancing the upwelling of cold nutrient rich waters and raising the thermocline.

The 1997-1999 El Niño/La Niña event was the strongest of the 20th century (Kerr 1998; McPhaden 1999). During July/August 1998 (week 1) a large La Niña event occurred which strengthened the trade winds resulting in upwelling of cold nutrient rich waters close to the surface (McPhaden 1999). This is clearly seen in Figure 9.3l by the lower SST values during week 1 when compared with week 2 in the central equatorial Pacific (note that week 2 was during a non- El Niño/La Niña year).

This injection of cold nutrient rich waters during July/August 1998 ignited a huge surface phytoplankton bloom, with a 40-fold increase in chlorophyll-*a* (Chavez et al. 1999). This phytoplankton bloom is the largest phytoplankton bloom observed in the equatorial Pacific to date. This bloom, driven by the EUC, migrated from east to west at a speed of 105 km day^{-1} and its shape was distorted by Tropical Instability Waves (TIWs) (Chavez et al. 1999; Ryan et al. 2002) due to the meridional transport linked to the propagation of TIWs (notice the wave like shape of the bloom in Figure 9.3c).

A2: Despite the two 8-day composites being at the same seasonal time period, large differences in both SST and the phytoplankton community composition in Figure 9.3c, f, i and l are related to the fact that week 1 was during a large La Niña event (July/August 1998) and week 2 during non- El Niño/La Niña conditions. The inter-decadal occurrence of the El Niño/La Niña phenomena appears to be related to these differences.

Studies in the equatorial Pacific have suggested that diatoms do not contribute more than 20% of phytoplankton biomass (Blanchot et al. 2001; Kobayashi and Takahashi 2002; Dandonneau et al. 2004). Assuming diatoms comprise the majority of the microphytoplankton in the Equatorial Pacific, this value compliments our estimates of microphytoplankton % chlorophyll-*a* in non- El Niño/La Niña conditions (week 2, Figure 9.3b). However, blooms of diatoms have been reported in this area (Bender and McPhaden 1990; Chavez et al. 1990; Archer et al. 1997), particularly under La Niña events (Chavez et al. 1999; Strutton and Chavez 2000; Ryan et al. 2002; Alvain et al. 2008). Under such conditions, and using the algorithm of Brewin et al. (2010b), microphytoplankton appear to contribute as much as 70% of the phytoplankton biomass (Figure 9.3a).

Iron limitation is especially important for diatoms (Boyd, 2002) and when nutrients and iron are abundant in the photic layer, diatoms grow rapidly and dominate the phytoplankton population. Using *in situ* measurements, Chavez et al. (1999) linked the elevated levels of macronutrients and enhanced supply of iron associated with the La Niña event, to an increase in the concentration of diatoms (Table 1, Chavez et al. 1999), supporting the results shown in Figure 9.3a-c.

Differences in nanophytoplankton between the two weeks are less pronounced with slight increases in nanophytoplankton % chlorophyll-*a* at the periphery of the microphytoplankton bloom in week 1 (Figure 9.3f). In contrast to microphytoplankton, picophytoplankton are seen to have much lower % chlorophyll-*a* across the equatorial Pacific in week 1 when compared with week 2 (Figure 9.3i).

A3: The higher SST values seen in the south-east equatorial Pacific during week 1 (Figure 9.3j and l) appear to correspond to changes in the composition of nano- and picophytoplankton. While much of this area is masked by cloud coverage in Figure 9.3c, f and i, there is a slightly higher % chlorophyll-*a* of picophytoplankton in week

1 when compared with week 2 (Figure 9.3i) in the south-east equatorial Pacific. The inverse is seen for nanophytoplankton (Figure 9.3f).

Since picophytoplankton are smaller in size, they have a higher surface-to-volume ratio than nanophytoplankton, and hence can absorb nutrients with high efficiency under nutrient limited conditions (Raven 1998). Therefore, in stratified, nutrient depleted areas, such as the southern Pacific subtropical gyre, picophytoplankton are expected to dominate (Chisholm 1992; Dandonneau et al. 2004; Ras et al. 2008).

When comparing Figure 9.3g with Figure 9.3h, the southern subtropical gyre (indexed by the high levels of picophytoplankton >60 % chlorophyll-*a* south of the equator) appears further north and east in Figure 9.3g when compared with Figure 9.3h, possibly causing these discrepancies. This may be linked to changes in physical forcing during a La Niña event.

9.7 Summary

In this example we have highlighted the strong link between the community composition of the phytoplankton in the equatorial Pacific and the inter-decadal physical forcing (in this case the El Niño/La Niña phenomena). Changes in the community structure of phytoplankton appear to reflect changes in temperature in the equatorial Pacific. Larger phytoplankton cell sizes are associated with dynamic systems where fresh nutrients are available, and smaller size classes are associated with stratified, nutrient depleted regions. This tight coupling between the biology and physics in the equatorial Pacific supports the idea that all the components of a system, physical, biological and chemical, are intertwined, and that each component of the system is intrinsically linked with another (Lovelock 1992).

Remote sensing makes it possible to collect data in dangerous or inaccessible areas. It can also compliment costly and slow data collection *in situ*, ensuring that areas or particles are not disturbed, and it offers repeat viewing and can be used to monitor wide areas synoptically, not possible by conventional ground sampling methods. However, the true capabilities of remote sensing can only come to fruition when it is used in conjunction with *in situ* based measurements, for calibration and validation purposes. With more optical and biological *in situ* measurements, quantitative development and validation of the satellite PFT algorithms can continue. Furthermore, the synergistic benefits of using these observational techniques in conjunction allow for well-constrained, accurate biological and geophysical parameters that can then be assimilated into mathematical models to improve their parameterisation and our understanding needed to predict future change.

9.8 Acknowledgements

The NASA SeaWiFS project team and the NASA Jet Propulsion Laboratory Physical Oceanography Distributed Active Archive Centre is acknowledged for satellite data and all contributors to the SeaBASS data set for *in situ* pigment data. This work is funded by the National Environmental Research Council, UK, the National Centre for Earth Observation and NERC Oceans 2025 programme (Themes 6 and 10).

9.9 References and further reading

Alvain S, Moulin C, Dandonneau Y, Breon FM (2005) Remote sensing of phytoplankton groups in case 1 waters from global SeaWiFS imagery. Deep-Sea Res I 52:1989-2004

Alvain S, Moulin C, Dandonneau Y, Loisel H (2008) Seasonal distribution and succession of dominant phytoplankton groups in the global ocean: A satellite view. Global Biogeochem Cycles 22:GB3001, doi:3010.1029/2007GB003154

Archer D, Aiken J, Balch W, Barber D, Dunne J, Flament P, Gardner W, Garside C, Goyet C, Johnson E, Kirchman D, McPhaden M, Newton J, Peltzer E, Welling L, White J, Yoder J (1997) A meeting place of great ocean currents: shipboard observations of a convergent front at 2 degrees N in the Pacific. Deep-Sea Res II 44:1827-1849

Behrenfeld MJ, Bale AJ, Kolber DD, Aiken J, Falkowski PG (1996) Confirmation of iron limitation of phytoplankton photosynthesis in the equatorial Pacific Ocean. Nature 383:508-511

Bender ML, McPhaden MJ (1990) Anomalous nutruent distribution in the equatorial Pacific in April 1988: Evidence for rapid biological uptake. Deep-Sea Res I 37:1075-1084

Blanchot J, Andre JM, Navarette C, Neveux J, Radenac MH (2001) Picophytoplankton in the equatorial Pacific: vertical distributions in the warm pool and in the high nutrient low chlorophyll conditions. Deep-Sea Res I 48:297-314

Boyd PW (2002) Environmental factors controlling phytoplankton processes in the Southern Ocean. J Phycol 38:844-861

Brewin RJW, Lavender SJ, Hardman-Mountford NJ, Hirata T, Raitsos DE, Barciela R (2008) An intercomparison of bio-optical techniques for detecting phytoplankton functional types from space Ocean Optics XIX. SPIE proceedings, PDF No. oo080577 (CDROM), Castelvecchio Pascoli, Italy, 6-10 Oct. 2008

Brewin RJW, Lavender SJ, Hardman-Mountford NJ, Hirata T (2010a) A spectral response approach for detecting dominant phytoplankton size class from satellite remote sensing. Acta Oceanol Sin 29:14-32

Brewin RJW, Sathyendranath S, Hirata T, Lavender SJ, Barciela R, Hardman-Mountford NJ (2010b) A three-component model of phytoplankton size class for the Atlantic Ocean. Ecol Model 221:1472-1483

Chavez FP, Buck KR, Barber RT (1990) Phytoplankton taxa in relation to primary production in the equatorial Pacific. Deep-Sea Res I 37:1733-1752

Chavez FP, Strutton PG, Friederich GE, Feely RA, Feldman GC, Foley DG, McPhaden MJ (1999) Biological and Chemical Response of the Equatorial Pacific Ocean to the 1997-98 El Niño. Science 286: 2126 - 2131

Chisholm SW (1992) Phytoplankton Size. In: Primary Productivity and Biogeochemical Cycles in the Sea edited by Falkowski PG, Woodhead AD pp 213-237, Springer, New York

Ciotti AM, Bricaud A (2006) Retrievals of a size parameter for phytoplankton and spectral light absorption by coloured detrital matter from water-leaving radiances at SeaWiFS channels in a continental shelf off Brazil. Limnol Oceanogr Methods 4:237-253

Coale KH, Fitzwater SE, Gordon RM, Johnson KS, Barber RT (1996) Control of community growth and export production by upwelled iron in the equatorial Pacific Ocean. Nature 379:621-624

Cullen JJ (1991) Hypotheses to explain high-nutrient conditions in the open sea. Limnol Oceanogr 36:1578-1599

Dandonneau Y, Deschamps PY, Nicolas JM, Loisel H, Blanchot J, Montel Y, Thieuleux F, Becu G (2004) Seasonal and interannual variability of ocean color and composition of phytoplankton communities in the North Atlantic, equatorial Pacific and South Pacific. Deep-Sea Res II 51:303-318

Devred E, Sathyendranath S, Stuart V, Maas H, Ulloa O, Platt T (2006) A two-component model of phytoplankton absorption in the open ocean: Theory and applications. J Geophys Res 111:C03011, dio:03010.01029/02005JC002880

Etcheto J, Boutin J, Dandonneau Y, Bakker DCE, Feely RA, Ling RD, Nightingale PD, Wanninkhof R (1999) Air-sea CO_2 flux variability in the equatorial Pacific Ocean near 110°W. Tellus 51B:734-747

Feely RA, Wanninkhof R, Takahashi T, Tans P (1999) Influence of El Nino on the Equatorial Pacific contribution to atmospheric CO2 accounts. Nature 398:597-601

Hansen B, Bjørnsen PK, Hansen PJ (1994) The size ratio between planktonic predators and their prey. Limnol Oceanogr 39:395-403

Hardman-Mountford NJ, Hirata T, Richardson KA, Aiken J (2008) An objective methodology for the classification of ecological pattern into biomes and provinces for the pelagic ocean. Remote Sens Environ 112:3341-3352

Hirata T, Aiken J, Hardman-Mountford NJ, Smyth TJ, Barlow RG (2008a) An absorption model to derive phytoplankton size classes from satellite ocean colour. Remote Sens Environ 112:3153-3159

Hirata T, Hardman-Mountford NJ, Aiken J, Smyth T, Barlow R, Martines-Vicente V, Fishwick J, Bernard S (2008b) Optical approach to derive phytoplankton size classes using ocean color remote sensing. Ocean Optics XIX, Castelvecchio Pascoli, Italy, 6-10 Oct. 2008

Jennings S, Warr KJ, Mackinson S (2002) Use of size-based production and stable isotope analyses to predict trophic transfer efficiencies and predator-prey body mass ratios in food webs. Mar Ecol Prog Ser 240:11-20

Kerr RA (1998) Models win big in forecasting El Niño. Science 280:522-523

Kobayashi F, Takahashi K (2002) Distribution of diatoms along the equatorial transect in the western and central Pacific during the 1999 La Nina conditions. Deep-Sea Res II 49:2801-2821

Kostadinov TS, Siegel DA, Maritorena S (2009) Retrieval of the particle size distribution from satellite ocean colour observations. J Geophys Res 114:C09015, dio:09010.01029/02009JC005303

Le Quéré C, Harrison SP, Prentice CI, Buitenhuis ET, Aumont O, Bopp L, Claustre H, Cotrim Da Cunha L, Geider R, Giraud X, Klaas C, Kohfeld KE, Legendre L, Manizza M, Platt T, Rivkin R, Sathyendranath S, Uitz J, Watson AJ, Wolf-Gladrow D (2005) Ecosystem dynamics based on plankton functional types for global ocean biogeochemistry models. Glob Change Biol 11:2016-2040

Lovelock JE (1992) A numerical model for biodiversity. Philos Trans R Soc B Bio Sci 338:383-391, doi: 310.1098/rstb.1992.0156

Martin JH, Fitzwater SE (1988) Iron deficiency limits phytoplankton growth in the north-east Pacific subarctic. Nature 331:341-343

Martin JH (1991) Iron, Liebig's Law, and the Greenhouse. Oceanography 4:52-55

McPhaden MJ (1999) Genesis and evolution of the 1997-98 El Niño. Science 283:950-954

Nair A, Sathyendranath S, Platt T, Morales J, Stuart V, Forget M-H, Devred E, Bouman H (2008) Remote sensing of phytoplankton functional types. Remote Sens Environ 112:3366-3375

Raitsos DE, Lavender SJ, Maravelias CD, Haralambous J, Richardson AJ, Reid PC (2008) Identifying four phytoplankton functional types from space: An ecological approach. Limnol Oceanogr 53(2):605-613

Ras J, Claustre H, Uitz J (2008) Spatial variability of phytoplankton pigment distributions in the Subtropical South Pacific Ocean: a comparsion between *in situ* and predicted data. Biogeosciences 5:353-369

Raven JA (1998) Small is beautiful: The picophytoplankton. Funct Ecol 12:503-513

Ryan JP, Polito PS, Strutton PG, Chavez FP (2002) Unusual large-scale phytoplankton blooms in the equatorial Pacific. Prog Oceanogr 55:263-285

Sathyendranath S, Stuart V, Cota G, Maas H, Platt T (2001) Remote sensing of phytoplankton pigments: a comparison of empirical and theoretical approaches. Int J Remote Sensing 22:249-273

Sathyendranath S, Watts L, Devred E, Platt T, Caverhill C, Maass H (2004) Discrimination of diatoms from other phytoplankton using ocean-colour data. Mar Ecol Prog Ser 272:59-68

Scharf FS, Juanes F, Rountree RA (2000) Predator size - prey size relationships of marine fish predators: interspecific variation and effects of ontogeny and body size on trophic-niche breadth. Mar Ecol Prog Ser 208:229-248

Strutton PG, Chavez FP (2000) Primary productivity in the equatorial Pacific during the 1997-1998 El Niño. J Geophys Res 105:26089-26101

Takahashi T, Sutherland SC, Sweeney C, Poisson A, Metzl N, Tilbrook B, Bates N, Wanninkhof R, Feely RA, Sabine C, Olafsson J, Nojiri Y (2002) Global sea-air CO_2 flux based on climatological surface ocean pCO_2 and seasonal biological and temperature effects. Deep-Sea Res II 49:1601-1622

Thomas WH (1979) Anomalous nutrient-chlorophyll interrelationships in the offshore eastern tropical Pacific Ocean. J Mar Res 37:327-335

Toggweiler JR, Carson S (1995) What are upwelling systems contributing to the ocean's carbon and nutrient budgets? In: Summerhayes CP, Emeis KC, Angel MV, Smith RL, Zeitzschel B (eds) Upwelling in the ocean. Modern processes and ancient records. John Wiley & Sons, Chichester, UK, p 337-360

Uitz J, Claustre H, Morel A, Hooker SB (2006) Vertical distribution of phytoplankton communities in open ocean: An assessment based on surface chlorophyll. J Geophys Res 111:CO8005, doi:8010.1029/2005JC003207

Vidussi F, Claustre H, Manca BB, Luchetta A, Marty JC (2001) Phytoplankton pigment distribution in relation to upper thermocline circulation in the eastern Mediterranean Sea during winter. J Geophys Res 106(C9):19,939-919,956

Walsh JJ (1976) Herbivory as a factor in patterns of nutrient utilization in sea. Limnol Oceanogr 21:1-13

Werdell PJ, Bailey SW (2002) The SeaWiFS Bio-optical Archive and Storage System (SeaBASS): Current architecture and implementation. NASA Tech. Memo. 2002-211617. In: Fargion GS, McClain C (eds) NASA Goddard Space Flight Center. Greenbelt, Maryland, 45 pp